

DISSERTATION

ANALYSIS AND MODELING OF CELLS, CELL BEHAVIOR, AND HELICAL  
BIOLOGICAL MOLECULES

Submitted by

Steven Benoit

Department of Mathematics

In partial fulfillment of the requirements

For the Degree of Doctor of Philosophy

Colorado State University

Fort Collins, Colorado

Spring, 2011

Doctoral Committee:

Advisor: Vakhtang Putkaradze

Patrick D. Shipman

Donald J. Estep

Mario C. Marconi

Stuart A. Tobet

Copyright by Steven Benoit 2011  
All Rights Reserved

## ABSTRACT

### ANALYSIS AND MODELING OF CELLS, CELL BEHAVIOR, AND HELICAL BIOLOGICAL MOLECULES

Mathematical models of biological systems have evolved over time and through the introduction and growth of computer simulation and analysis. Models have increased in sophistication and power through the combination of multi-scale approaches, molecular and granular dynamics simulations, and advances in parallelization and processing speed. However, current cell models cannot accurately predict behaviors at the whole-cell scale, nor can molecular models predict accurately the complex shape assumed by large biological molecules including proteins, although significant progress is being made toward this goal. The present work introduces new models in three domains within biological systems modeling. We first discuss a phenomenological model of observed cell motions in developing tissue that characterizes cells according to a best-fit generalized diffusion model and combines this data with Voronoi diagrams to effectively visualize patterns of cell behavior in tissue. Next, we present a series of component models for cells and cell structure that support simulations involving tens to hundreds of cells in a way that captures behaviors ignored by existing models, including pseudopod formation, membrane mechanics, cytoskeletal polymerization / depolymerization, and chemical signal transduction. The resulting models exhibit many of the behaviors of real-world cells including polarization and chemotaxis. Finally, we present a method for analysis of biological molecules that form helical conformations that includes long-range electrostatic interactions as well

as short-range interactions to prevent self-intersections. We consider the stability of molecules with repeating monomers that include off-axis charge concentrations and derive energy landscapes to identify stable conformations, then analyze helical stability using geometric methods.

## ACKNOWLEDGMENTS

I am grateful to V. Putkaradze for longstanding support and encouragement, and to the Department of Mathematics for supporting my rather lengthy doctoral program. I thank S. Tobet and the members of his lab, most notably M. Stratton, B. Searcy, and K. Frahm who provided patient help as I learned some measure of cell biology. I also acknowledge the able assistance of D. D. Holm with the work on molecular simulation and geometric methods, and of P. Ziherl and A. Hocevar with whom I had fruitful discussions on modeling and analysis of cell motions. Finally, I am grateful to T. Chen, M. de Miranda, G. Majdic, D. Strle, and my cofellows Z. Cashero, M Easterly, C. Hartshorn, M. Duwe, A. Chen, R. Hoppal, and C. Bishop for including me in their interdisciplinary program and giving me the opportunity to experience such a multi-faceted project.

This work has been supported by a National Science Foundation grant number GDE-0841259; Colorado State University, Thomas Chen, Principal Investigator, Michael A. de Miranda and Stuart Tobet Co-Principal Investigators.

Any opinions, findings, conclusions or recommendations expressed in this material are those of the author and do not necessarily reflect the views of the National Science Foundation.

## TABLE OF CONTENTS

Abstract . . . . .	ii
Acknowledgments . . . . .	iv
<b>1 INTRODUCTION: CELLS, BIOLOGICAL MOLECULES . . . .</b>	<b>1</b>
1.1 Outline of the Dissertation . . . . .	2
<b>2 IN-VITRO ANALYSIS OF CELL BEHAVIOR . . . . .</b>	<b>7</b>
2.1 Introduction . . . . .	7
2.2 Analysis of cell trajectories . . . . .	8
2.2.1 Equalization of pixel intensities . . . . .	10
2.2.2 Merging focal planes . . . . .	11
2.2.3 Gaussian smoothing . . . . .	12
2.2.4 Global motion compensation . . . . .	14
2.2.5 Identification of cells as local maxima . . . . .	17
2.2.6 Trajectory extraction . . . . .	18
2.2.7 Local motion compensation . . . . .	20
2.2.8 Cell trajectory analysis . . . . .	21
2.3 Automated analysis tool . . . . .	22
2.3.1 The data pipe . . . . .	22
2.3.2 The filter set . . . . .	23
<b>3 MESOSCALE MODELS OF CELLS AND CELL BEHAVIOR . .</b>	<b>28</b>

3.1	Introduction . . . . .	28
3.1.1	Component Model Construction and Notation . . . . .	30
3.2	Plasma membrane . . . . .	31
3.2.1	Cells and organelles as domains . . . . .	33
3.2.2	Maintaining validity of the triangulated mesh . . . . .	34
3.2.3	Energy Functional . . . . .	35
3.2.4	Force Field . . . . .	37
3.2.5	Two-dimensional approximation . . . . .	41
3.2.6	Force in the two-dimensional approximation . . . . .	42
3.2.7	Simulation results . . . . .	43
3.3	Cytoskeleton and signal transduction . . . . .	44
3.3.1	Current Models of Cell Shape Modulation . . . . .	46
3.3.2	Modeling actin as a collection of linked spheres . . . . .	47
3.3.3	Signal transduction . . . . .	49
3.3.4	Signal particle detection and activation . . . . .	50
3.3.5	Actin dynamics and treadmilling . . . . .	50
3.4	Conclusions . . . . .	53
<b>4</b>	<b>MODELS OF HELICAL BIOLOGICAL MOLECULES . . . . .</b>	<b>65</b>
4.1	Introduction . . . . .	66
4.2	Derivation in $SE(3)$ coordinates . . . . .	69
4.3	Linear rod with straight unstressed conformation . . . . .	78
4.4	Energy of a helical conformation . . . . .	81
4.5	Multiple helical conformations . . . . .	86
4.6	Linear stability analysis . . . . .	87
4.7	Computation of potential energy . . . . .	95
4.8	Numerical stability of a linear polymer . . . . .	98

4.8.1	Setup of the problem . . . . .	99
4.8.2	Results of linear stability computations . . . . .	102
4.9	Conclusion . . . . .	104
<b>A PROOF OF LEMMA 3.2.1 . . . . .</b>		<b>109</b>
<b>B ALGORITHM FOR MESH ADJUSTMENT . . . . .</b>		<b>111</b>
B.0.1	Edge length adjustment . . . . .	111
B.0.2	Elimination of caps . . . . .	112
B.0.3	Elimination of microfaces . . . . .	113
B.0.4	Elimination of needles . . . . .	113
B.0.5	Maximal movement for subsequent modeling iteration . . . . .	114
<b>C GEOMETRIC PROPERTIES OF <math>SE(3)</math> GROUP . . . . .</b>		<b>115</b>
<b>D TWIST DYNAMICS OF A STRAIGHT POLYMER . . . . .</b>		<b>119</b>

# CHAPTER 1

## INTRODUCTION: CELLS, BIOLOGICAL MOLECULES

The study and analysis of the composition, movement, and self-organization of cells into functional tissues spans the boundaries of biology, rigid body and continuum mechanics, fluid dynamics, chemistry, thermodynamics, and mathematics. In the present work, we explore three related aspects of this extremely broad field of study, each of which providing a window to understanding some aspect of the behavior of this and other complex biological systems.

In a way, this is the quintessential multi-scale problem. Behaviors at the molecular scale drive the construction of specialized proteins and polymers that dictate both the mechanical properties as well as the chemical responses of cells and facilitate cell communication. At a scale several orders of magnitude larger, cellular structures including cell membrane, cytoskeleton, and organelles drive bulk behavior including migration and adhesion, but simulation at this scale is well out of the reach of molecular methods. At even larger scales, the formation of tissue-scale structures from thousands of cells create a topography through which migrating cells travel to their destinations following chemical and mechanical cues, with the end result being a macro-scale organism that functions properly only because each cell migrates from its place of birth to its ultimate location correctly. An understanding of this process covers ten orders of magnitude, from Angstroms to meters, and represents one of the most challenging modeling problems known [1, 2].

## 1.1 Outline of the Dissertation

### Observation and analysis

The essential first step in construction of models of a complex system is observation and analysis of the system behavior at a scale appropriate to the modeling effort. In Chapter 2, we present an automated system for analysis of cell movements as observed using fluorescence video microscopy. This analysis generates a useful classification of behaviors for groups of cells in living tissue, and also provides a basis for comparison with simulated collections of cells under similar conditions.

This analysis is based on an observation protocol developed at Colorado State University that allows *in vitro* visualization of cell movements in embryonic tissues for up to three days [3]. The product of this imaging protocol is a series of multi-plane images, where the focus is swept through three planes, at a separation of 10 microns, in an attempt to capture images of cells through a roughly 40 micron thickness of tissue.

The automated tool processes the raw images produced from the microscope into a series of cell trajectories, then analyzes the diffusive properties of those trajectories, and correlates motion parameters with physical position in the sample, providing both numerical and visual representations of the results. Examples from the paraventricular region of hypothalamus are used to demonstrate the technique.

### Multi-scale modeling

There are a number of existing models of cells, cell components, and multi-cellular systems at various scales, ranging from molecular dynamics simulations of cell membranes and motor proteins through continuum mechanical models of large-scale tissue structures and models of cell dynamics and motion based on differential equations or

stochastic simulation. If we consider the set of models that begin with first-principle representations of the molecules, liquids and bond that constitute a cell as *bottom up* models, the most elaborate and robust of these are, at best, capable of simulating a small subset of a cell (say, the plasma membrane), for a very short time scale (on the order of a few milliseconds). These models can generate predictions of physical properties such as elastic or bulk moduli, viscosity, or tensile strength, which can be tested against observation, resulting in increased understanding of those component systems, but this class of model cannot hope to simulate whole-cell systems, much less systems of interacting cells or tissue.

The other approach, which we call *top down*, consists of models based on phenomenology of large aggregates of cells or tissue, and relies either continuum mechanical approaches that discard the notion of individual cells, or stochastic methods, which model cells as discrete points. While these approaches have achieved some success in modeling and predicting real-world behavior of cell aggregates, they do not provide insight into the cell-level processes that generate their predicted behaviors.

We see a need for a modeling "middle ground", or *mesoscale* models of cell aggregates. These models would capture the behaviors of cells that lead to migration and tissue formation, while stopping short of attempting to model at the molecular level. In Chapter 3, we present a class of mesoscale models of cells and their interactions, and describe a method by which these models can be integrated into a simulation environment that can support new models of individual cell components as they are developed.

## **Biological molecules**

At its lowest level, models of biological systems must consider individual molecules and their behavior and characteristics. For simple molecules or ions, this is a straightforward exercise in molecular dynamics. For more complex biomolecules, however, the mechanical properties of long-chain systems require a more efficient mechanism of study due to the large number of constituent parts. Many of these molecules, including the primary structural proteins of the cellular cytoskeleton (actin, tubulin, keratin, vimentin, etc.), form polymers with uniform structure along their length, opening these molecules to forms of analysis that take advantage of their intrinsic helical symmetries.

In Chapter 4, we present a method for quickly analyzing and classifying the stable conformations of helical molecules based on a geometric analysis that leverages the inherent symmetries in the molecules to identify helical stable shapes as well as explore the levels of stability of those shapes. This method can be applied to molecules that have arbitrarily complex monomers with arbitrary charge distributions, where charges need not be on the helical axis of the molecule. Long-range electrostatic forces are included in the analysis, and it is the interplay of these forces with elastic forces that result in stable helical conformations.

## **Implementations**

Finally, we provide, in a series of appendixes, a complete implementation of the three systems described in this work: the automated analysis tool to extract and analyze cell trajectories from sequences of multi-plane microscopic images; the system of meso-scale models of cell components and the simulation environment in which they can be integrated; and software to generate the energy landscapes and identify stable

helical conformations of biological molecules consisting of repeating monomer chains with generalized off-axis charge distributions. Each of these implementations are presented in the Java language, and are also available for download from the author's web site [4].

**Remark** Because of the diverse nature of the material covered in this dissertation, we choose to include a separate References section at the end of each chapter. It is hoped that this makes resources easier for the reader to locate.

## REFERENCES

- [1] Masaru Tomita. Whole-cell simulation: a grand challenge of the 21st century. *Trends in Biotechnology*, 19(6):205–210, June 2001.
- [2] David Harel. A grand challenge for computing: Towards full reactive modeling of a multi-cellular animal. *Lecture Notes in Computer Science*, 2937:39–60, 2003.
- [3] Stuart A. Tobet, Heather J. Walker, Marianne L. Seney, and Kwok W. Yu. Viewing cell movements in the developing neuroendocrine brain. *Integrative and Comparative Biology*, 43(6):794–801, 2003.
- [4] Steven Benoit. Personal web site. <http://lamar.colostate.edu/~sbenoit/>.

## CHAPTER 2

### IN-VITRO ANALYSIS OF CELL BEHAVIOR

#### 2.1 Introduction

An essential prerequisite to any modeling effort is a phenomenological study of the system under consideration. Observations can guide model development and provide a set of benchmarks against which model performance can be measured. The value of the model is then gaged by its ability to reproduce meaningful behaviors observed in the real-world system.

Video fluorescence microscopy is an essential tool for the study of cells and cell migration, and especially in the study of *in vitro* tissue slices. Of particular interest is the ability to prepare slices for imaging, then introduce reagents during the imaging cycle to allow detection of alterations in cell behavior that can be attributed to the reagents [1]. The output of these microscopy cycles consists of a series of images representing discrete time points (typically several minutes apart), and a set of distinct focal planes within the sample for each time point.

The analysis of the data that comes from video microscopy traditionally involves manual adjustment of image intensities, manual alignment of each successive image to compensate for motion of the sample on the stage during imaging, manual identification of points of interest (cells) in each frame, then assembly of those point locations into paths that can be subsequently evaluated to characterize cell behavior.

## Outline of the chapter

We first describe an analysis procedure that can be applied to a series of images generated by video fluorescence microscopy. Section 2.2 describes the steps of an analysis of cell trajectories that begins with the raw output images produced by a microscope under the control of MetaMorph<sup>®</sup> Microscopy Automation and Image Analysis Software<sup>1</sup>, and proceeds through the calculation of diffusion parameters for cell trajectories and the generation of a set of visualizations of the resulting cell motion characterizations. Examples of the results of the analysis when applied to the motion of cells near the paraventricular nucleus of the embryonic hypothalamus in mice are provided for illustration. Section 2.3 then describes a generalized framework for video analysis, consisting of a specification for *filters* and a data *pipe* from which the filters receive data and to which they deliver filtered data.

The Java source code of the author’s implementation of the automated analysis tool is available in the Appendix and on the author’s web site [2].

## 2.2 Analysis of cell trajectories

Throughout this section, we will denote an individual image frame with the letter  $\mathbf{F}$  (an abbreviation for *frame*). We use subscripts to index these image frames – an *image frame set*  $\{\mathbf{F}_{z,t}\}$ ,  $1 \leq z \leq m$ ,  $1 \leq t \leq n$ , is a set of image frames  $\mathbf{F}_{z,t}$ , where the index  $t$  represents the time, and  $z$  represents the focal plane, with respect to an arbitrary reference focal plane. A typical image frame set that we consider might contain thirty to forty time points, and three  $z$  values, separated from each other by some fixed distance (typical values of this separation would be 10 microns, or the order of the size of a cell).

---

<sup>1</sup>MetaMorph is a registered trademark of Molecular Devices, Inc.

During the analysis of a set of images, we will often generate new image frames from existing frames, and so we use parenthesized superscripts to indicate the generation of the frame. For example,  $\mathbf{F}_{z,t}^{(0)}$  might represent the raw image generated by a camera attached to the microscope, while  $\mathbf{F}_{z,t}^{(1)}$  represents the results of applying some filter to that raw image,  $\mathbf{F}_{z,t}^{(2)}$  represents the output of the second stage of image processing, and so forth.

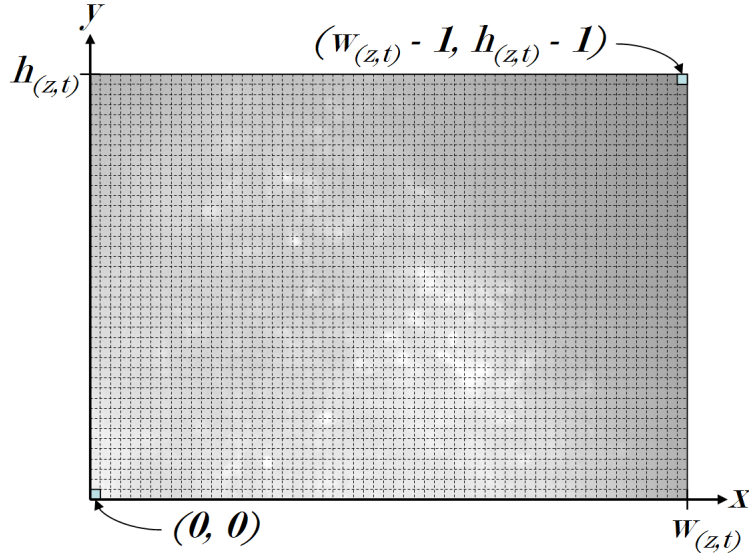


Figure 2.1: Cartesian coordinate system applied to image frames.

Within an image frame, we specify a Cartesian coordinate system, as shown in Figure 2.1, with the origin in the lower left corner of the image,  $x$  axis increasing to the right, and  $y$  axis increasing upward, scaled so one unit on each axis represents one pixel in the image. We denote the width and height of image frame  $\mathbf{F}_{z,t}^{(i)}$  by  $w_{z,t}^{(i)}$  and  $h_{z,t}^{(i)}$ , respectively. For example, an  $800 \times 600$  pixel image frame has  $w_{z,t}^{(i)} = 800$ , and  $h_{z,t}^{(i)} = 600$ . We refer to a pixel by the coordinates at its lower left corner – the pixel at the bottom left corner of the image frame would be referred to by coordinates  $(0, 0)$ , while the pixel in the upper right corner of an image frame is assigned coordinates  $(w_{z,t}^{(i)} - 1, h_{z,t}^{(i)} - 1)$ . We assume throughout that pixels have a 1:1 aspect ratio.

**Remark** This coordinate system is chosen to match the mathematician’s preferred frame, not the computer scientist’s preferred frame. Computer imaging systems typically place the  $(0, 0)$  coordinate in the upper left corner and allow  $y$  to increase downward. Making this choice, however, subjects the interpretation angle measures and functions like sine and cosine to confusion, and so we adopt the more traditional system.

### 2.2.1 Equalization of pixel intensities

The original raw image frames  $\{\mathbf{F}_{z,t}^{(0)}\}$  are collected with a digital camera which generates intensity values on a scale from 0 (no incident light) to some upper limit (typically either 255 or 65,535, corresponding to 8- or 16-bit unsigned binary values, respectively) which represents the maximum measurable light intensity, and presumably any intensities beyond this limit. In practice, however, the actual range of intensities measured is a very small subset of this range, concentrated near the lower limit. The result is that if the images are presented visually on a computer monitor, they appear as featureless black. Moreover, there is no guarantee that images taken at different time points or different Z planes have the same baseline intensity scale (the ambient light level may have changed, for example).

To do meaningful analysis, therefore, the intensity  $\lambda$  of the pixels in each image are first scaled so they fill the range  $0 \leq \lambda \leq 255$ , and image frames are further intensity-scaled such that all image frames have the same mean intensity. Letting  $\lambda_{x,y,z,t}^{(0)}$  be the intensity of the pixel at coordinates  $(x, y)$  in image frame  $\mathbf{F}_{z,t}^{(0)}$ , and letting  $w_{z,t}^{(0)}$  and  $h_{z,t}^{(0)}$  be the width and height of  $\mathbf{F}_{z,t}^{(0)}$  (in pixels), respectively, we first compute the average image intensity of each image as

$$\bar{\lambda}_{z,t}^{(0)} = \frac{1}{w_{z,t}^{(0)} h_{z,t}^{(0)}} \sum_{x=1}^{w_{z,t}^{(0)}} \sum_{y=1}^{h_{z,t}^{(0)}} \lambda_{x,y,z,t}^{(0)},$$

and the average intensity  $\bar{\Lambda}^{(0)}$  over all image frames as

$$\bar{\Lambda}^{(0)} = \frac{1}{nm} \sum_{t=1}^n \sum_{z=1}^m \bar{\lambda}_{z,t}^{(0)}.$$

The maximum and minimum overall intensity is given by

$$\lambda_{max}^{(0)} = \max\{\lambda_{x,y,z,t}^{(0)} : 1 \leq t \leq n, 1 \leq z \leq m, 0 \leq x \leq w_{z,t}, 0 \leq y \leq h_{z,t}\},$$

$$\lambda_{min}^{(0)} = \min\{\lambda_{x,y,z,t}^{(0)} : 1 \leq t \leq n, 1 \leq z \leq m, 0 \leq x \leq w_{z,t}, 0 \leq y \leq h_{z,t}\}.$$

We define a scale factor  $\alpha_{z,t}$  for each image frame as

$$\alpha_{z,t} = \frac{255\bar{\Lambda}^{(0)}}{\bar{\lambda}_{z,t}^{(0)}(\lambda_{max}^{(0)} - \lambda_{min}^{(0)})},$$

then generate by intensity-leveled images  $\mathbf{F}_{z,t}^{(1)}$  as image frames with  $w_{z,t}^{(1)} = w_{z,t}^{(0)}$ ,  $h_{z,t}^{(1)} = h_{z,t}^{(0)}$ , and

$$\lambda_{x,y,z,t}^{(1)} = \max\left((\lambda_{x,y,z,t}^{(0)} - \lambda_{min}^{(0)})\alpha_{z,t}, 255\right).$$

An example of a raw and intensity-leveled image frame are shown in Figure 2.2.

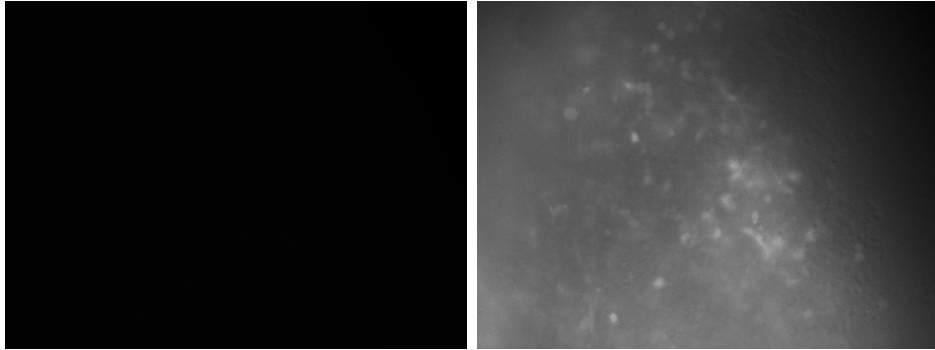


Figure 2.2: A raw image frame from microscope, and the resulting intensity-leveled image.

## 2.2.2 Merging focal planes

The reason that multiple focal planes are gathered during image acquisition is to increase the probability that a given cell in the sample is within reasonable focus

in at least one of the planes. The focal planes are roughly one cell body diameter apart, meaning that any cell within a section of tissue whose depth is equal to three cell diameters should be within half of its body diameter of the actual focal plane in one of the images. In-focus cells will appear as intensity maxima given the nature of fluorescence microscopy, while out-of-focus cells appear as a vague brightening of a broad region of the image.

Since the extents of an image frame in the  $x$  or  $y$  direction far exceeds the three cell diameters of resolution in the  $z$  direction, it makes little sense to attempt to include  $z$  coordinates in analyses of cell positions. However, capturing this extra  $z$  information may extend the time over which a cell is visible if it is moving transverse to the focal plane. We therefore merge the focal plane images into a single image that captures the intensity maxima revealed in each of the individual images. The merged image frames  $\mathbf{F}_t^{(2)}$  (where we may now omit the  $z$  subscript), are created with  $w_t^{(2)} = w_{z,t}^{(1)}$ ,  $h_t^{(2)} = h_{z,t}^{(1)}$ , and

$$\lambda_{x,y,t}^{(2)} = \max_{1 \leq z \leq m} \left\{ \lambda_{x,y,z,t}^{(1)} \right\} .$$

Figure 2.3 shows a portion of the result of merging three intensity-leveled image frames representing three different focal planes at a single time point. Realistically, there is a short time interval between the exposures, as the microscope would take some time to adjust its focal plane, but this time is very short (a few seconds) compared to the interval between time points (five or ten minutes, typically), so we consider these images to be simultaneous. In this case, the focal planes were very close and the input images show little variation.

### 2.2.3 Gaussian smoothing

Before we extract intensity maxima, we next apply a Gaussian smoothing to the images. The reason for this is that without smoothing, the location of an actual intensity

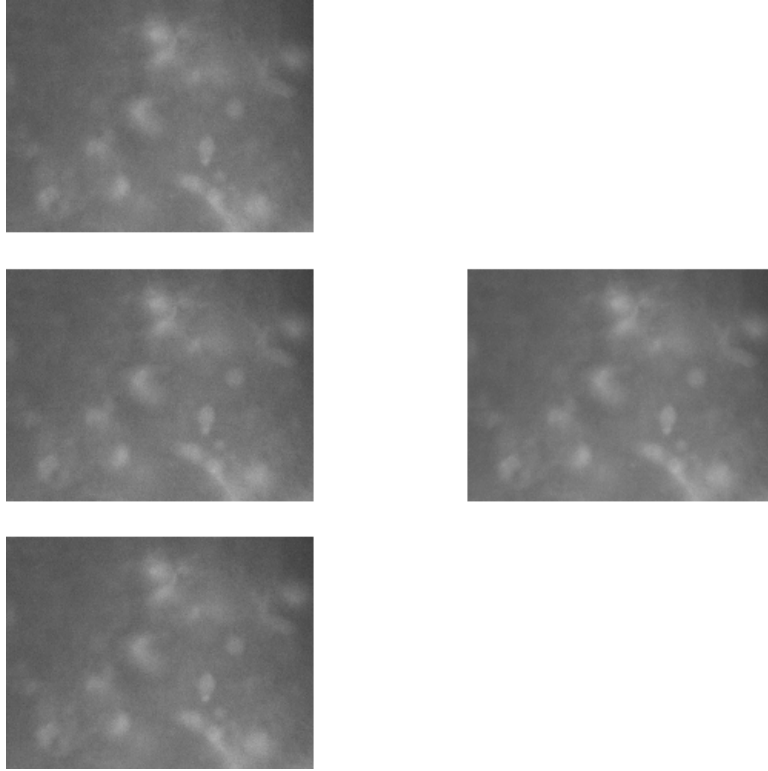


Figure 2.3: A magnified portion of three focal planes for a particular time point, and the resulting merged image.

maximum may be misinterpreted if noise gives a point near the actual maximum a higher intensity, making that point appear to be the location of the maxima. To avoid this, we generate a Gaussian kernel based on the function

$$G(x, y) = \frac{1}{2\pi} e^{-x^2 - y^2},$$

where we take  $x$  and  $y$  as integers in the range  $-2 \leq x \leq 2$ ,  $-2 \leq y \leq 2$ . The result is a five by five kernel with the values,

$$G = \frac{1}{2\pi} \begin{bmatrix} e^{-8} & e^{-5} & e^{-4} & e^{-5} & e^{-8} \\ e^{-5} & e^{-2} & e^{-1} & e^{-2} & e^{-5} \\ e^{-4} & e^{-1} & 1 & e^{-1} & e^{-4} \\ e^{-5} & e^{-2} & e^{-1} & e^{-2} & e^{-5} \\ e^{-8} & e^{-5} & e^{-4} & e^{-5} & e^{-8} \end{bmatrix}.$$

Normalizing this kernel,

$$G' = \frac{1}{2\pi \left(1 + \frac{4}{e} + \frac{4}{e^2} + \frac{4}{e^4} + \frac{8}{e^5} + \frac{4}{e^8}\right)} \begin{bmatrix} e^{-8} & e^{-5} & e^{-4} & e^{-5} & e^{-8} \\ e^{-5} & e^{-2} & e^{-1} & e^{-2} & e^{-5} \\ e^{-4} & e^{-1} & 1 & e^{-1} & e^{-4} \\ e^{-5} & e^{-2} & e^{-1} & e^{-2} & e^{-5} \\ e^{-8} & e^{-5} & e^{-4} & e^{-5} & e^{-8} \end{bmatrix}.$$

we can then convolve it with the region surrounding each pixel in image frame  $\mathbf{F}_t^{(2)}$  to obtain  $\mathbf{F}_t^{(3)}$ , taking any pixel value with coordinates outside the limits of  $\mathbf{F}_t^{(2)}$  to have an intensity of zero. The result is a new set of image frames with  $w_t^{(3)} = w_t^{(2)}$ ,  $h_t^{(3)} = h_t^{(2)}$ , and

$$\lambda_{x,y,t}^{(3)} = \sum_{i=1}^5 \sum_{j=1}^5 G'_{i,j} \lambda_{x+i-2,y+j-2,t}^{(2)}.$$

Figure 2.4 shows a portion of an image frame before and after Gaussian smoothing was applied.

## 2.2.4 Global motion compensation

It is an unfortunate fact that during the course of observation, a tissue sample will move on the microscope stage, resulting in a shift of the sample in images. This movement may be global (vibration or shock moves the slide on the stage), or local

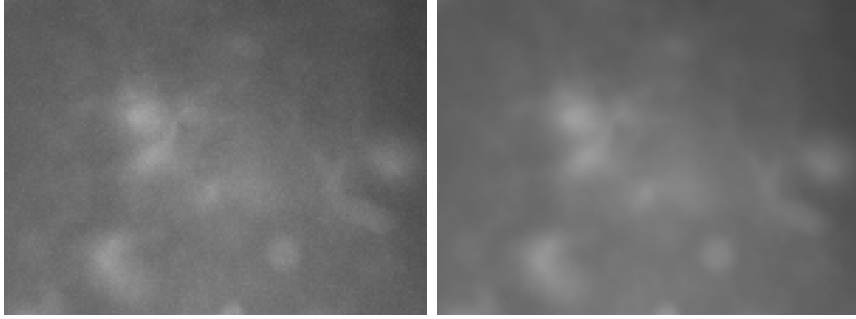


Figure 2.4: The effect of Gaussian smoothing on an image frame.

(the tissue changes shape, shrinking or expanding during image acquisition). If this motion is not compensated, any cell positions and trajectories will be inaccurate, reducing the validity of results, or making what appear to be high-confidence predictions that are blatantly wrong. For example, tissue shrinkage might result in very clean looking trajectories with a clear directional bias, but which bear no relationship to actual cell movement within its surrounding tissue.

Two factors are at work here - global movements of the sample on the stage, and local changes in the relative size and shape of the tissue. These two effects need different strategies to address them, and at this stage, we focus on compensating for global motion of the sample on the stage. To prevent shrinkage and shape change effects from confounding this process, we restrict our attention to the center of the image, acting to stabilize that portion of the image against motion. We compute the offset vector  $(\Delta x, \Delta y)$  for each image frame such that it correlates most strongly with the image frame from the preceding time point, where the correlation is taken over the middle fourth of the image in each axis. In particular, to compute the correlation between the image frame  $\mathbf{F}_{t-1}^{(3)}$  and  $\mathbf{F}_t^{(3)}$  for a particular vector offset  $(\Delta x_i, \Delta y_i)$ , we set  $x_- = \max(\Delta x_i, 0)$ ,  $x_+ = \min(w_t^{(3)}, w_t^{(3)} + \Delta x_i)$ ,  $y_- = \max(\Delta y_i, 0)$ , and  $y_+ =$

$\min(h_t^{(3)}, h_t^{(3)} + \Delta y_i)$ , then the mean squared error (MSE) between the two images is

$$\text{MSE} = \frac{1}{(x_+ - x_-)(y_+ - y_-)} \sum_{x=x_-}^{x_+} \sum_{y=y_-}^{y_+} \left( \lambda_{x,y,t-1}^{(3)} - \lambda_{x-\Delta x_i, y-\Delta y_i, t}^{(3)} \right)^2.$$

We select the  $(\Delta x_i, \Delta y_i)$  for which the MSE is minimized. In actual implementations, we may restrict this search to vectors  $(\Delta x_i, \Delta y_i)$  whose length does not exceed some limit, in the interest of efficiency. Once the vector is selected for each  $t$ ,  $2 \leq t \leq n$ , we chain these vectors together into a trajectory, and compute the minimum bounding rectangle  $R$  that contains the entire trajectory.

$$R = \left\{ (x, y) : \min_{2 \leq j \leq n} \sum_{i=2}^j \Delta x_i < x < \max_{2 \leq j \leq n} \sum_{i=2}^j \Delta x_i, \right. \\ \left. \min_{2 \leq j \leq n} \sum_{i=2}^j \Delta y_i < y < \max_{2 \leq j \leq n} \sum_{i=2}^j \Delta y_i \right\}.$$

We denote the boundaries of this rectangle as  $R_l = \min\{x : x \in R\}$ ,  $R_r = \max\{x : x \in R\}$ ,  $R_b = \min\{y : y \in R\}$ , and  $R_t = \max\{y : y \in R\}$ , where the subscripts  $l$ ,  $r$ ,  $b$ , and  $t$  represent left, right, bottom, and top, respectively. We then construct image frames  $\{\mathbf{F}_t^{(4)}\}$  with  $w_t^{(4)} = w_t^{(3)} + R_r - R_l$ , and  $h_t^{(4)} = h_t^{(3)} + R_t - R_b$ . The first frame is not shifted, but has a border of zero-intensity pixels,

$$\lambda_{x,y,1}^{(4)} = \begin{cases} \lambda_{x+R_l, y+R_b, 1}^{(3)} & \text{if } 0 \leq x + R_l \leq w_t^{(3)} \text{ and } 0 \leq y + R_b \leq h_t^{(3)} \\ 0 & \text{otherwise} \end{cases}.$$

Subsequent frames are shifted by the cumulative resultant of all preceding vectors  $(\Delta x_i, \Delta y_i)$ . If we let

$$(Dx_i, Dy_i) = \left( \sum_{j=1}^i \Delta x_j, \sum_{j=1}^i \Delta y_j \right),$$

then for  $2 \leq t \leq n$ ,

$$\lambda_{x,y,t}^{(4)} = \begin{cases} \lambda_{x+R_l+Dx_i, y+R_b+Dy_i, t}^{(3)} & \text{if } 0 \leq x + R_l + Dx_i \leq w_t^{(3)} \\ & \text{and } 0 \leq y + R_b + Dy_i \leq h_t^{(3)} \\ 0 & \text{otherwise} \end{cases}.$$

Figure 2.5 shows three image frames from a globally motion compensated sequence. The black borders where the image was shifted to compensate for global motion are apparent.

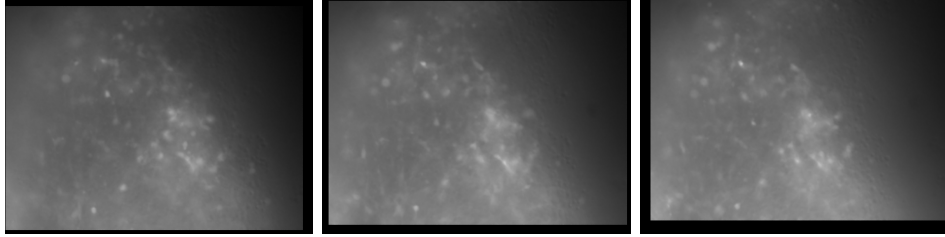


Figure 2.5: Image frames after global motion-compensation has been applied.

### 2.2.5 Identification of cells as local maxima

With the images stabilized against global motions, we next identify cells in the image frames  $\{\mathbf{F}_t^{(4)}\}$ . We first define a threshold intensity  $\lambda_{min}$  and consider only pixels with an intensity  $\lambda_{x,y,t} \geq \lambda_{min}$  (experiment suggests a value of  $\lambda_{min} = 80$  is reasonable). We then define a maximum radius  $r_{max}$  that we expect a cell to have in our image, and for each pixel  $\lambda_{x,y,t}$  in a given image frame  $\mathbf{F}_t^{(4)}$ , we classify the pixel as a local maximum if

1. the pixel has the highest intensity of any pixel within  $r_{max}$ ,
2. the pixel has no neighbor that is black, and
3. there is at least one pixel  $\lambda_{x',y',t}$  within  $r_{max}$  with  $|\lambda_{x',y',t} - \lambda_{x,y,t}| \geq \frac{\lambda_{min}}{4}$ .

Having done this, it is possible that two or more pixels within  $r_{max}$  of one another had the same intensity and were both classified as maxima. If this is the case, we combine any such maxima into a single maximum, giving that maximum coordinates that are the average of the coordinates of all maxima identified within the  $r_{max}$

neighborhood. The end result will be that no maximum is within  $r_{max}$  of any other maximum.

We will denote the set of  $J$  maxima in image frame  $\mathbf{F}_t^{(4)}$  by  $\{(Px_{t,j}, Py_{t,j})\}$ ,  $1 \leq j \leq J$ . Figure 2.6 shows an image frame with the set of identified intensity maxima highlighted.

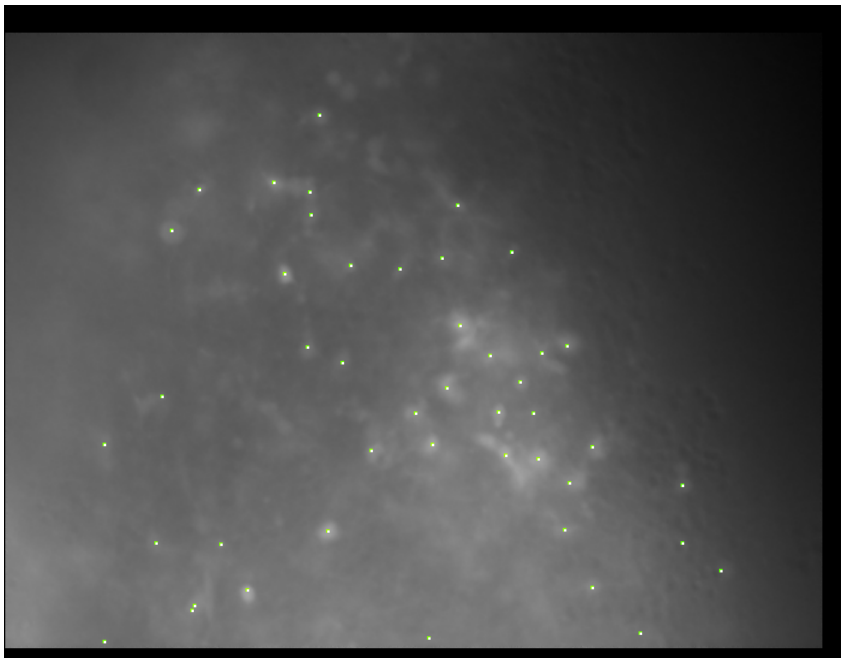


Figure 2.6: The set of local intensity maxima identified in an image frame.

### 2.2.6 Trajectory extraction

Now that we have a set of identified maxima, we can assemble them into cell trajectories. To do this, we compare the sets of maxima from a given image frame with those in the subsequent image frame, looking for the maximum from the first frame that is nearest a maximum from the second frame, if any maxima in the first frame are within  $r_{max}$  of any maxima in the second frame. If such a pairing is found, those two maxima are considered as part of a trajectory, and are removed from consideration.

This process is repeated until there are no maxima in the first frame within  $r_{max}$  of any in the second frame.

For a given pair of image frames  $\mathbf{F}_t^{(4)}$  and  $\mathbf{F}_{t+1}^{(4)}$ , denote the set of  $K_t$  identified pairings defined above by

$$S_{t,t+1} = \{s_{t,1}, \dots, s_{t,K_t}\},$$

where

$$s_{t,k} = [(Px_{t,a_k}, Py_{t,a_k}), (Px_{t+1,b_k}, Py_{t+1,b_k})].$$

Any maxima that do not fall into one of these pairings are discarded.

Trajectories are assembled by chaining these pairings together. If the second maximum of any pairing is the first maximum of a pairing in the subsequent frame, the two pairings are combined into a sequence of three points, and so forth, until all pairings that share a common maximum have been collected into the longest possible sequences of maxima.

The result will be a set of trajectories  $T_i$ , each of which consisting of a sequence of maxima that span some range of time points,

$$T_i = \{(Px_{t_i,a_i}, Py_{t_i,a_i}), (Px_{t_i+1,b_i}, Py_{t_i+1,b_i}), \dots, (Px_{t_i+l_i,z_i}, Py_{t_i+l_i,z_i})\},$$

where  $l_i$  is the length of trajectory  $T_i$ , and  $t_i$  is the time point where the trajectory began.

At the end of this process, we cull any trajectories that are too small to analyze. The cull criteria can include a minimum length of trajectory needed to obtain valid statistical information on its behavior, or a lower limit on the amount of total motion we require in order to make a trajectory worth analyzing. We found 10 steps to be a reasonable lower limit for trajectory length, and culled any trajectories that never moved more than  $r_{max}/3$  from their starting point.

## 2.2.7 Local motion compensation

Given the set of trajectories, this identifies the local areas within the sequence of image frames that need to be analyzed for local motion (shrinkage or shape changes in the tissue). We wish to analyze cell motion *relative to its surrounding tissue*, and so we need to compensate for this tissue movement without losing the cell motion in the process.

We do this by considering the pairwise steps of a trajectory between frames (the  $s_{t,k}$  from which trajectories are assembled above). For each such pairing, we perform exactly the same motion compensation analysis that was done to compensate for global motion, but in this case we use a smaller region (a rectangle centered at the maximum position in each frame, with edge length one twelfth of the total image size in each axis), and we ignore all points within  $r_{max}$  of the maxima. That is, we disregard the cell motion when correlating the tissue regions. The vector that gives the lowest MSE represents the motion of the tissue surrounding the cell, independent of the cell motion.

For a given trajectory  $T_i$  consisting of  $l_i$  steps, this will generate  $l_i - 1$  tissue motion vectors  $(\delta x_{t_j}, \delta y_{t_j})$ ,  $t_i + 1 \leq j \leq t_i + l_i$ . The corrected cell trajectory,  $\widehat{T}_i$ , is composed of the points

$$\widehat{T}_i = \left\{ (Px_{t_i, a_i}, Py_{t_i, a_i}), (Px_{t_i+1, b_i} - \delta x_{t_i+1}, Py_{t_i+1, b_i} - \delta y_{t_i+1}), \dots, \left( Px_{t_i+l_i, z_i} - \sum_{k=i+1}^{l_i} \delta x_{t_i+k}, Py_{t_i+l_i, z_i} - \sum_{k=i+1}^{l_i} \delta y_{t_i+k} \right) \right\}.$$

This notation is cumbersome at best, so at this point we relabel the points in the corrected trajectories, retaining the starting point and starting time index for correlation with position and time during the analysis. In what follows, we denote a corrected trajectory as

$$\mathcal{T}_i = \{(x_{i,j}, y_{i,j})\}, 1 \leq j \leq l_i \quad \text{where} \quad (x_{i,1}, y_{i,1}) = (0, 0).$$

We denote the initial point of  $\mathcal{T}_i$  as  $(x_i^*, y_i^*)$ , and the starting time point of the trajectory as  $t_i^*$ .

### 2.2.8 Cell trajectory analysis

For each corrected trajectory  $\mathcal{T}_i = \{(x_{i,j}, y_{i,j})\}$ , we compute the following values

$$\langle x \rangle_j = \frac{1}{j} \sum_{k=1}^j (x_{i,k} - x_i^*) \quad \text{and} \quad \langle y \rangle_j = \frac{1}{j} \sum_{k=1}^j (y_{i,k} - y_i^*),$$

$$d_j = \sqrt{(x_{i,j} - x_i^*)^2 + (y_{i,j} - y_i^*)^2} \quad \text{and} \quad \langle d_j \rangle = \frac{1}{j} \sum_{k=1}^j d_j,$$

and

$$\langle (d_j - \langle d_j \rangle)^2 \rangle = \frac{1}{j} \sum_{k=1}^j (d_j - \langle d_j \rangle)^2.$$

We then perform a least-squares regression to find the best-fit curve of the form

$$y = 4Kj^\alpha$$

to the data series  $\{\langle (d_j - \langle d_j \rangle)^2 \rangle\}$ ,  $1 \leq j \leq l_i$ . This function represents a diffusion model of the cell's motion, where  $K$  is the diffusion constant (representing how easily the cell can move in the surrounding tissue), and  $\alpha$  characterizes the diffusion of the cell, where  $\alpha < 1$  represents *subdiffusive* motion,  $\alpha = 1$  represents normal *diffusive* motion, and  $\alpha > 1$  indicates *superdiffusive* behavior.

By correlating the diffusion constant  $K$ , diffusion exponent  $\alpha$ , along with trajectory length, average speed, average direction, and total distance covered with cell position in tissue, and with the presence or absence of treatment reagents, we can extract a substantial amount of information from a series of microscopic image frames.

## 2.3 Automated analysis tool

The author's implementation of the automated analysis described in the previous section is a Java-based system that uses a general concept of a series of *filters* which take their input data from a *pipe* and which add output data to that pipe for downstream filters to use. A screen image from the automated analysis tool is shown in Figure 2.7.

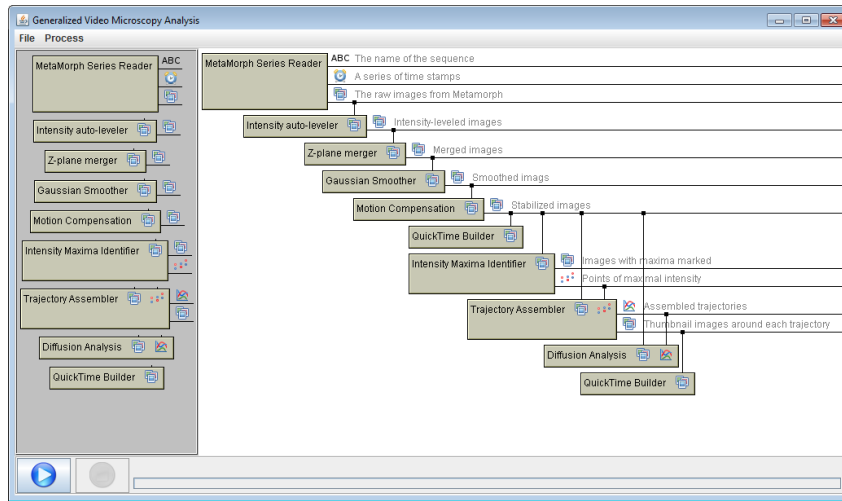


Figure 2.7: A typical screen view of the automated analysis tool. The list of available filters are shown on the left, and the assembled filter tree is on the right. Start and stop buttons at the bottom control the process, and a progress bar indicates status.

### 2.3.1 The data pipe

By a *pipe*, we mean a collection of named data objects of specified type. A data object can be anything from a simple text string to a complex data structure such as a series of images or a set of coordinate points. When a data object is added to a pipe, it becomes available to any filters that draw from that pipe. By naming each data object, the pipe can contain multiple objects of a given type. Filters retrieve

objects from the pipe by name, then verify that the object is of the expected data type.

The pipe object has the ability to store itself to a file system, and to load itself from a previously stored state. After each filter in the analysis is executed, the pipe is stored to the hard drive. In this way, if an automated process is interrupted, it can reload its prior state and resume with the last filter that did not complete, rather than executing all filters again. An executor object handles loading of stored pipes and executing each filter in turn based on a comparison of the data objects that filter requires and the data objects currently available in the pipe.

### 2.3.2 The filter set

The analysis application described here includes a set of nine filters, used for various stages of processing. Before the first filter is executed, the user is prompted for a working directory in which to load and store files, and any existing pipe information in that directory is loaded to allow interrupted analyses to continue. It should be noted that the filter set listed here is by no means exhaustive, and the application supports the development and integration of new filters as needed to extend the analysis.

**MetaMorph file reader filter** This filter is typically the first filter in the filter chain. It searches for MetaMorph image sets (indicated by the presence of files with ".nd" file extensions), and presents a list of the image sets it finds for the user to choose from. It then reads the TIF files generated by the MetaMorph program that form the selected image set. Each TIF file may contain several images, representing the various Z planes captured at a single time point, or may contain several time points in a single file. The outputs of this filter are the name of the selected image set; an array of images, with each column representing a time point, and each row

representing a focal plane; and a series of time stamps representing the actual times each time point was captured.

**Intensity leveling filter** This filter implements the intensity leveling algorithm described in the prior section. It takes as its input the raw images that the MetaMorph file reader filter generates and produces as its output an array of the intensity-leveled images, with the same dimensions as the input array

**Z-plane merger filter** This filter merges several focal planes into a single image, by selecting the highest intensity value across all focal planes for each pixel, and constructing the resulting image. The input to this filter is an image array of arbitrary size. The output is an image array with a single row and as many columns as the input array.

**Gaussian smoother filter** This filter smooths the images in an image array so subsequent detection of maxima will identify the locations of objects in the frame accurately. It convolves a Gaussian kernel with the input images to produce smoothed images. The input of the filter is an image array of arbitrary size, and the output is a new image array of the same dimensions with the smoothed images.

**Global motion compensation filter** Global motion compensation attempts to stabilize the center portion of an image array by correlating each frame with the prior frame, and maximizing that correlation over some transformation of the second frame. In the present implementation, only translation transformations are considered, so the filter can compensate for linear displacements of the sample on the stage during image acquisition. Rotational transformations will be added in the future to correct for rotations of the sample on the stage as well. The input to this filter is an image array of arbitrary dimension, and the output is a new image array of the same dimension

but whose images are transformed in such a way as to stabilize the central portion of the images throughout the sequence. The size of the images in the output image array are larger by an appropriate amount so that transforming the input images does not truncate any of the original image data.

**Local maxima identification filter** This filter identifies local maxima in an image array, producing a point-set array as its output. A point set array is an array of the same dimensions as the input image array, but where each array element is a set of points in the image frame representing the coordinates of the maxima. This filter also examines the ambient region surrounding each point, correlating it with the same region in the subsequent frame using the same techniques that the global motion compensation filter used. The result is an ambient tissue velocity for the region surrounding each cell that can be used to determine cell motion relative to surrounding tissue, rather than relative to the sample as a whole.

**Trajectory assembler filter** Trajectory assembly examines the point set array and ambient tissue velocities and attempts to determine which maxima in adjacent frames represent the same object. Having done this, it assembles trajectories across as many frames as possible. The output of this process is a list of trajectories with actual coordinates and compensated coordinates that factor out the ambient tissue motion. This filter also produces a series of images showing the region surrounding a trajectory with the cell's position in the region for each frame. These thumbnail images can then be assembled by the QuickTime filter (described below) to generate movies of individual cells traveling in tissue.

**Diffusion analysis filter** The diffusion analysis takes assembled trajectories and computes the mean squared displacement of each cell from its starting point over time.

It then fits this data to a diffusion model of the form  $y = 4Kt^\alpha$  using a least-squares algorithm, generating a diffusion constant  $K$  and exponent  $\alpha$  that characterized cell motion as subdiffusive, diffusive, or superdiffusive. The output of this filter is a set of Excel spreadsheets with the detailed calculations and results, a series of graphs of mean squared distances for each trajectory and the associated best-fit diffusion curve, and a series of visualizations that divide the tissue into a Voronoi diagram around each cell location, then color the regions in this diagram based on parameter values, including mean cell speed, distance traveled, diffusion constant, and diffusion exponent.

**QuickTime movie creation filter** The final filter in the set is a QuickTime movie generator. This filter takes an arbitrary image array as its input and produces a QuickTime movie from each row in that image array. This filter can be attached at one or more points in the filter tree to create helpful visualizations of any stage in the analysis process.

## REFERENCES

- [1] Stuart A. Tobet, Heather J. Walker, Marianne L. Seney, and Kwok W. Yu. Viewing cell movements in the developing neuroendocrine brain. *Integrative and Comparative Biology*, 43(6):794–801, 2003.
- [2] S. Benoit. Personal web site. <http://lamar.colostate.edu/~sbenoit/>.

# CHAPTER 3

## MESOSCALE MODELS OF CELLS AND CELL BEHAVIOR

### 3.1 Introduction

Most cells encountered in living organisms have complex internal structures, enclosed within a membrane. Such *eukaryotic* cells exhibit widely diverse morphology and behavior in living organisms. The ability of cells to move and form larger structures is essential to many biological processes, including reproduction, [1, 2], embryonic cell migration [3–5], immune response [6–9], wound healing [10, 11], axon formation [12–14], and others. Cells can migrate significant distances from their place of origin to their ultimate location in tissue, guided by chemical and mechanical signals [15, 16]. Understanding interactions of large aggregates of cells during tissue growth and organization is challenging due to the complex nature of the system and the difficulty of imaging migrating cells *in vivo*.

Mathematical models of cell aggregation date back to the works of Patlak (1953) [17] and Keller and Segel (1971) [18]. These works considered cells as isolated, moving, *active* particles that exhibit reaction to the environment by, for example, excreting chemical into the surrounding media other particles can react to. The models then address the continuum description for the motion of these particles, relating cell

densities to chemical concentration distributions rather than tracking individual cell positions or trajectories. However, such an idealized view of cells as infinitesimally small objects in space leads to the possibilities of infinitely high concentrations of cells [19–23]. Various ways of regularizing that singularity have been suggested, such as [24, 25], most of those relating to the very intuitive idea that for finite size particles, the density cannot reach values beyond some critical *dense packing*, so that the density evolution equation must be modified to include this property. In addition, the dynamics of intercellular interaction changes under closed packing, which must be addressed as well. More recent work, including [26] and [27] model individual cells with local interactions and reproduce global behavior in reasonable agreement with observation.

The continuum models are powerful tools for the study of motion and aggregations of particles, including motile cells. However, under realistic conditions of organism development, motile cells not only form closely packed aggregates, but also considerably change their shape during the process. The change of shape of individual units in large aggregates under close packing is a phenomenon that, to our knowledge, has not been studied consistently. Of course, deformation of a cell could be addressed using a molecular approach to modeling the cell, but because of extreme complexity of even the most simple cells, such approach cannot describe collective dynamics of many cells. The goal of this chapter is to find a suitable “middle ground” of the course-graining of cellular structure, in order to accurately represent aggregation dynamics. A reasonable number of model elements for a simulation on a modern computer is on the order of  $10^8$ , if we assume short-range interactions between the elements as well as an efficient neighbor-finding methodology. The desire to study behavior in aggregates on the order of, say 10,000 cells, then, calls for models with around 10,000 model elements per cell that capture with sufficient fidelity cell behaviors critical to

migration and guidance. The present work attempts to address this need by developing models for the principal components of cells and describing a framework in which these models can interact to simulate the desired aggregate systems.

## **Outline of the chapter**

We assume the primary factors influencing cell aggregate behavior are cell membrane mechanics, cytoskeleton, adhesion, and signal transduction, and will model each component separately. We begin with some global constraints on component models that will facilitate their integration, then within each functional area, we present a component model with the objective of keeping total model element count over the aggregate within our target range of  $10^8$ . We then describe a framework in which these models can be integrated to produce tissue-scale simulations, while allowing for new models of individual components to be added as they are developed. Finally, we provide results of simulations performed using our suite of component models and compare with observations from developing embryonic tissue. Our simulations were all performed in two dimensions, but we describe three-dimensional models in the text, which we plan to implement in future work.

### **3.1.1 Component Model Construction and Notation**

Component models will be based on collections of interacting model elements. To facilitate efficient computation, only short-range forces will be considered. This removes electrostatic effects from consideration, a restriction that bears further study in the future. Moreover, we will consider all model elements to be points or spheres, and all body interactions in the model to be either contact, Hooke spring, Lennard-Jones, or soft sphere interactions. At first glance, this seems a very restrictive constraint, but as will be shown, a wide variety of structures can be represented with surprising

fidelity under such limitations, and this restriction allows model elements from diverse component models to interact with a consistent and efficient mechanism. Within this system, model element are characterized by a center position and radius. We will use  $\mathbf{p}_i$  to denote the position of the  $i^{\text{th}}$  model element,  $r_i$  to denote its radius, and  $(x_i, y_i, z_i)$  to denote its coordinates with respect to a standard right-handed orthonormal coordinate frame.

Given our stated target capability of modeling  $10^4$  cells, with roughly  $10^4$  model elements per cell, we divide this number among the individual systems as shown in Table 3.1 to inform model development in the sequel. An objective in component model design is that increasing element counts should model behavior more accurately, with the asymptotic limit of large element counts being a very good representation of the component structure.

Table 3.1: Approximate per-cell target element counts for component models.

Component model	Target element count
Cell Membrane	2,000
Cytoskeleton	6,000
Signal Transduction	1,000
Extra-Cellular Environment	1,000

### 3.2 Plasma membrane

The plasma membrane separates the interior (cytoplasmic) domain and exterior (extracellular) domain. It consists of a bilayer of phospholipids in which proteins are embedded at irregular intervals [28], and at concentrations on the order of one protein to fifty lipids [29]. Individual lipids are in an ordered liquid or gel-like state in

which a lipid is free to move relative to its neighbors (which it does quite readily) or move to the other layer within the bilayer (which proceeds much more slowly) [30]. Cell membranes act as elastic media, and there are many factors in the composition of the membrane, proteins that span the membrane, and interaction of the membrane with the cytoskeleton that can lead to shape and curvature changes [31].

The cell membrane is not a static surface, but dynamically forms a variety of structures [30,32,33]. These structures are not well understood, but proposed organizational units include shells (rings of cholesterol and sphingolipid surrounding proteins in the membrane, much like a hydration shell around ions in aqueous solution [34]), clusters (groups of a few proteins with their associated shells [29]), caveolae (invaginations of the membrane coated with caveolin [34]), nanodomains and rafts (regions with larger extent than a cluster that maintain stability for longer time periods than the membrane in general [29]), and pores (transient openings in the membrane [33]). In addition, the membrane may be able to buckle and fold in response to local stimuli [33]. A variety of techniques have been used to model lipid membranes, a survey of which can be found in [35–38], but none of which the author is aware provide a model in the range of our stated target model element count.

Typical values of key mechanical properties of plasma membranes are shown in Table 3.2.

Table 3.2: Empirical mechanical properties of plasma membranes.

Property	Typical Value	Citation
Elastic modulus ( $K_c$ )	$7 \times 10^{-20}$ J	[39]
Tension ( $T$ )	$3 \times 10^{-5}$ N/m	[40]
Area per lipid	$5.89 \times 10^{-19}$ m <sup>2</sup>	[41]
Bilayer thickness	$4.45 \times 10^{-9}$ m	[41]

### 3.2.1 Cells and organelles as domains

We can view a cell, organelle or vesicle as an open simply connected domain  $\mathcal{C}$  in  $\mathbb{R}^N$  whose boundary  $\Omega_{\mathcal{C}}$  is a smooth manifold of dimension  $N - 1$ . Domains of distinct cells may not overlap, nor may domains of distinct organelles or vesicles within a given cell. We expect such domains to have fixed, or at least slowly varying, interior volume, but it has been shown that membrane surface area can change quickly in response to changes in cell shape, so we do not constrain surface area [42].

For the purpose of designing a model for discrete simulation, we will represent the boundary  $\Omega_{\mathcal{C}}$  of  $\mathcal{C}$  by a triangulated mesh consisting of faces  $\mathcal{F} = \{F_i\}$ ,  $i \in \{1, \dots, N_F\}$ . We denote the set of vertex points in such a triangulation as  $\mathcal{P} = \{\mathbf{p}_j\}$ ,  $j \in \{1, \dots, N_P\}$ . To simplify what follows, we consider an edge as pair of oppositely directed edges between two vertex points. Attaching an orientation to an edge allows the boundary of a triangle to be specified as an ordered sequence of edges in such a way that its outward-facing side can be determined.

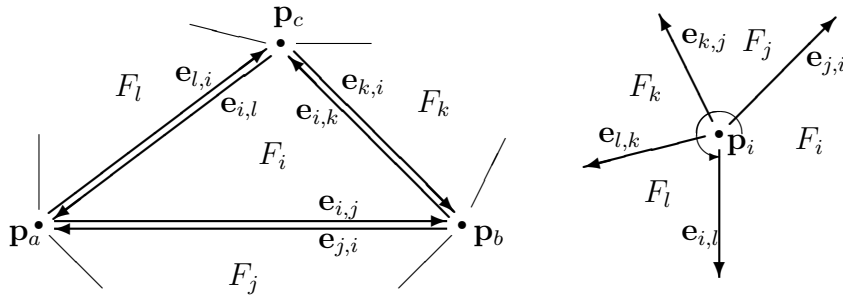


Figure 3.1: The set of faces, edges, and vertex points that make up a triangulated mesh representation of the boundary of a domain, as viewed from the exterior of the domain.

As shown in Figure 3.1, we label an edge  $\mathbf{e}_{i,j}$  based on the two faces it connects, with the ordering of the indexes such that the left-hand face is listed first when viewed from the exterior of the domain. Under this convention, if we have a face  $F_i$  consisting

of edges  $(\mathbf{e}_{i,j}, \mathbf{e}_{i,k}, \mathbf{e}_{i,j})$  then the outward pointing normal vector  $\hat{\mathbf{n}}_i$  of  $f_i$  is given by

$$\hat{\mathbf{n}}_i = \frac{\mathbf{e}_{i,j} \times \mathbf{e}_{j,k}}{|\mathbf{e}_{i,j} \times \mathbf{e}_{j,k}|}. \quad (3.1)$$

We denote the list of edges leaving a vertex point  $\mathbf{p}_i$ , in counter-clockwise order as seen from the exterior of the domain, by  $\mathcal{E}_i = (\mathbf{e}_{j,i}, \mathbf{e}_{k,j}, \dots, \mathbf{e}_{i,l})$ , and we will at times refer to this list of edges by a single index, as in  $\mathcal{E}_i = (\mathbf{e}_1, \mathbf{e}_2, \dots, \mathbf{e}_m)$ , when doing so makes the exposition more clear.

If we restrict the domains that represent cells to those whose surface is a genus 0 manifold, with Euler characteristic 2, then the number of vertex points is related to the number  $N_F$  of faces by

$$N_P = 2 + \frac{N_F}{2}.$$

Given a target model element (vertex point) count  $N_P$  for a cell or organelle membrane, then, we compute the number of faces in the triangulation as  $N_F = 2(N_P - 2)$ . In practice, we algorithmically construct a domain in some initial state using this fixed number of faces. The number of faces in the model may change as the system evolves, however, as explained below.

We will make use of the area  $A_i$  of face  $F_i$ , which is computed using any two of the edges that make up the boundary of the face, say  $\mathbf{e}_{i,j}$  and  $\mathbf{e}_{k,i}$ , as

$$A_i = \frac{1}{2} |\mathbf{e}_{i,j} \times \mathbf{e}_{k,i}|. \quad (3.2)$$

### 3.2.2 Maintaining validity of the triangulated mesh

During simulation of membrane dynamics, vertices move in response to forces, which causes changes in edge lengths and the shape and size of faces. The mesh representation of the membrane may require adjustment after each iteration in the evolution process to ensure that the mesh remains valid. Moreover, the structure of the mesh may provide an upper limit on the movement that vertices may undergo in each time

step to prevent degeneracies in the triangulation. Appendix B describes an algorithm that can be applied after each iteration to ensure the model remains valid, and which produces an upper limit on movement that can be used in the subsequent evolution step to prevent invalidating the mesh.

### 3.2.3 Energy Functional

#### Internal energy of a cell

Once we have defined the outer shape of the cell, let us turn our attention to the energy of the cell in a given configuration. The energy functional  $E$ , the gradient of which will drive evolution of the membrane, is given by

$$E = E^{(elem)} + E^{(pres)} + E^{(tens)} + E^{(curv)} + E^{(si)}, \quad (3.3)$$

whose terms represent, respectively, model element interaction energy, compression of the interior volume, surface tension, membrane curvature, and a term to prevent membrane self-intersection.

To model the interaction of the membrane with a set of model elements with positions  $\{\mathbf{p}_j\}$  and radii  $r_j$ , for  $j \in \{1, \dots, M\}$ , we use a Lennard-Jones potential

$$E^{(elem)} = K_{LJ} \sum_{i=1}^{N_p} \sum_{j=1}^M (\xi_{i,j}^{12} - 2\xi_{i,j}^6) \quad \text{where} \quad \xi_{i,j} = \frac{\varepsilon + r_j}{|\mathbf{p}_i - \mathbf{q}_j|}, \quad (3.4)$$

where the inner sum is taken over the set of model elements that are not part of the membrane, whose positions we denote by  $\{\mathbf{q}_j\}$ ,  $1 \leq j \leq M$ . Note that this energy only describes inter-cellular interaction under close contact, and *does not* describe the long-range interaction between the cells due to, for example, electrostatic interactions.

The pressure term is based on the compression of the cell volume  $V$  (relative to its equilibrium volume  $V_0$ ), and on the bulk modulus of cytoplasm, which we estimate as  $K_b = 10^5$  Pa. Using a modulus closer to that of water, say  $2 \times 10^9$  Pa, while more

realistic, generates very large forces in response to small movements in membrane elements. Our lower estimate preserves the essential incompressibility of the cell while bringing the magnitude of the pressure forces into alignment with other forces in the model.

$$E^{(pres)} = \frac{K_b}{2V_0} (V - V_0)^2. \quad (3.5)$$

We compute the cell volume of a given triangulation of the cell surface using the following lemma, whose proof we present in Appendix A,

**Lemma 3.2.1.** *Given a triangulation  $\mathcal{F}$  of  $\Omega_C$  where  $C$  is a compact 2-manifold embedded in  $\mathbb{R}^3$  whose vertices are  $\{\mathbf{q}_1, \mathbf{q}_2, \dots, \mathbf{q}_n\}$ , and where  $\mathbf{q}_i = (x, y, z)$  with respect to some orthonormal basis  $\{\mathbf{e}_1, \mathbf{e}_2, \mathbf{e}_3\}$ , if each triangle  $f_i = (\mathbf{p}_{i_1}, \mathbf{p}_{i_2}, \mathbf{p}_{i_3})$  has outward-pointing normal vector  $\hat{\mathbf{n}}_i$ , then the volume  $V$  of the interior of  $\mathcal{F}$  is given by*

$$V = \frac{1}{6} \sum_{f_i \in \mathcal{F}} |(\mathbf{p}_{i_2} - \mathbf{p}_{i_1}) \times (\mathbf{p}_{i_3} - \mathbf{p}_{i_1})| \mathbf{p}_{i_1} \cdot \hat{\mathbf{n}}_i. \quad (3.6)$$

We formulate surface tension energy based on surface area, where the force acts to minimize surface area. Therefore,

$$E^{(tens)} = \frac{T}{2} \sum_{i=1}^{N_f} A_i, \quad (3.7)$$

where  $A_i$  is given by (3.2).

To compute curvature energy, if we denote the angle between face normals  $\hat{\mathbf{n}}_i$  and  $\hat{\mathbf{n}}_j$  by  $\alpha_{i,j}$ , which we can compute directly using  $\alpha_{i,j} = \cos^{-1} \hat{\mathbf{n}}_i \cdot \hat{\mathbf{n}}_j$ , then the energy contribution of edge  $\mathbf{e}_{i,j}$  can be estimated by

$$E_{i,j}^{(curv)} = \frac{4K_c |\mathbf{e}_{i,j}|}{\varepsilon} \tan^2 \frac{\alpha_{i,j}}{2} = \frac{4K_c |\mathbf{e}_{i,j}|}{\varepsilon} \frac{1 - \hat{\mathbf{n}}_i \cdot \hat{\mathbf{n}}_j}{1 + \hat{\mathbf{n}}_i \cdot \hat{\mathbf{n}}_j},$$

where  $K_c$  is the elastic modulus of the membrane. Summing over all edges associated with each vertex point, and dividing by two since this counts each edge twice,

$$E^{(curv)} = \frac{2K_c}{\varepsilon} \sum_{i=1}^{N_p} \sum_{\mathbf{e}_{j,k} \in \mathcal{E}_i} |\mathbf{e}_{j,k}| \frac{1 - \hat{\mathbf{n}}_j \cdot \hat{\mathbf{n}}_k}{1 + \hat{\mathbf{n}}_j \cdot \hat{\mathbf{n}}_k}. \quad (3.8)$$

Self-intersection in the membrane is prevented by placing a soft sphere of radius  $\varepsilon/2$  at each vertex in the membrane model, but ignoring the interaction between spheres that lie on vertices connected by an edge. That is, an edge can shorten to accommodate membrane shape changes, but “distant” vertices will be prevented from getting close to one another. The energy term is given by,

$$E^{(si)} = K_{SS} \sum_{i=1}^{N_p} \sum_j \begin{cases} \left( \frac{\varepsilon}{|\mathbf{p}_j - \mathbf{p}_i|} \right)^{12} - 1 & |\mathbf{p}_j - \mathbf{p}_i| < \varepsilon \\ 0 & |\mathbf{p}_j - \mathbf{p}_i| \geq \varepsilon \end{cases}, \quad (3.9)$$

where  $K_{SS}$  is the soft-sphere interaction strength and the inner sum is taken over the set  $\mathcal{V}$  of vertices excluding vertex  $\mathbf{p}_i$  and any vertices that share an edge with  $\mathbf{p}_i$ .

**Remark** In practice, an efficient neighbor-finding algorithm will result in very few terms in the inner sums for both  $E_{elem}$  and  $E_{si}$ , since we can make  $\varepsilon$  a global upper limit for the radius of elements that interact via Lennard-Jones or soft sphere potentials, assuming we truncate our Lennard-Jones potentials at, say,  $r = 2.5\varepsilon$ .

### 3.2.4 Force Field

The force  $\mathbf{F}_i$  on vertex  $\mathbf{p}_i$  is given by  $\mathbf{F}_i = -\nabla_i E$  where  $\nabla_i = (\partial/\partial x_i, \partial/\partial y_i, \partial/\partial z_i)$ . The force due to interactions with other (non-membrane) model components  $\mathbf{q}_j$ ,  $1 \leq j \leq M$  with radii  $r_j$  is given by

$$\mathbf{F}_i^{(elem)} = -12K_{LJ} \sum_{j=1}^M (\xi_{i,j}^{12} - \xi_{i,j}^6) \frac{\mathbf{q}_j - \mathbf{p}_i}{|\mathbf{q}_j - \mathbf{p}_i|^2} \quad \text{where} \quad \xi_{i,j} = \frac{\varepsilon + r_j}{|\mathbf{q}_j - \mathbf{p}_i|}. \quad (3.10)$$

When we consider the force due to pressure experienced by a single vertex point, recall that in (3.6), we are free to choose any starting edge and reference vertex to

compute the contribution of a face to the volume. Therefore, we will assume that for all faces that a particular vertex point participates in, we use the vertex of interest as  $\mathbf{p}_i$  in (3.6). If we index the edges in  $\mathcal{E}_i$  as  $(\mathbf{e}_1, \mathbf{e}_2, \dots, \mathbf{e}_n)$ , and make the identification  $\mathbf{e}_{n+1} \equiv \mathbf{e}_1$ , and denote the points that edge  $\mathbf{e}_j$  connects by  $(\mathbf{p}_i, \mathbf{q}_j)$ , then

$$\mathbf{F}_i^{(pres)} = -\frac{K_b}{2V_0} \nabla_i (V - V_0)^2 = -\frac{K_b}{6V_0} (V - V_0) \sum_{j=1}^n (\mathbf{q}_j \times \mathbf{q}_{j+1}). \quad (3.11)$$

The tension force on a vertex point  $\mathbf{p}_i$  includes contributions from each face the vertex participates in. As with the pressure term, we are free to choose which edges we use to compute the area in (3.2), and so we choose those that meet at  $\mathbf{p}_i$ .

$$\mathbf{F}_i^{(tens)} = -\frac{T}{4} \sum_{j=1}^n \nabla_i |\mathbf{e}_j \times \mathbf{e}_{j+1}| = -\frac{T}{4} \sum_{j=1}^n \hat{\mathbf{n}}_j \times (\mathbf{q}_{j+1} - \mathbf{q}_j), \quad (3.12)$$

where  $\hat{\mathbf{n}}_j$  is the outward-pointing unit normal vector to the face with edges  $\mathbf{e}_j$  and  $\mathbf{e}_{j+1}$ .

When computing the curvature force on vertex  $\mathbf{p}_i$ , we must consider that the vertex position affects not only the edges directly connected to the vertex, but also the edges opposite the vertex in each face containing the vertex. The edge opposite the vertex in the face with edges  $\mathbf{e}_j$  and  $\mathbf{e}_{j+1}$  is given by  $\mathbf{e}_{j+1} - \mathbf{e}_j$ , and if we denote the normal vector of the face that shares this edge by  $\hat{\boldsymbol{\eta}}_j$ , then

$$\begin{aligned} \mathbf{F}_i^{(curv)} &= -\frac{4K_c}{\varepsilon} \sum_{j=1}^n \nabla_i \left( |\mathbf{e}_{j+1}| \frac{1 - \hat{\mathbf{n}}_j \cdot \hat{\mathbf{n}}_{j+1}}{1 + \hat{\mathbf{n}}_j \cdot \hat{\mathbf{n}}_{j+1}} + |\mathbf{e}_{j+1} - \mathbf{e}_j| \frac{1 - \hat{\mathbf{n}}_j \cdot \hat{\boldsymbol{\eta}}_j}{1 + \hat{\mathbf{n}}_j \cdot \hat{\boldsymbol{\eta}}_j} \right) \\ &= -\frac{4K_c}{\varepsilon} \sum_{j=1}^n \left( \frac{1 - \hat{\mathbf{n}}_j \cdot \hat{\mathbf{n}}_{j+1}}{1 + \hat{\mathbf{n}}_j \cdot \hat{\mathbf{n}}_{j+1}} \nabla_i |\mathbf{e}_{j+1}| + \frac{1 - \hat{\mathbf{n}}_j \cdot \hat{\boldsymbol{\eta}}_j}{1 + \hat{\mathbf{n}}_j \cdot \hat{\boldsymbol{\eta}}_j} \nabla_i |\mathbf{e}_{j+1} - \mathbf{e}_j| \right. \\ &\quad \left. - \frac{2|\mathbf{e}_{j+1}|}{(1 + \hat{\mathbf{n}}_j \cdot \hat{\mathbf{n}}_{j+1})^2} \nabla_i (\hat{\mathbf{n}}_j \cdot \hat{\mathbf{n}}_{j+1}) - \frac{2|\mathbf{e}_{j+1} - \mathbf{e}_j|}{(1 + \hat{\mathbf{n}}_j \cdot \hat{\boldsymbol{\eta}}_j)^2} \nabla_i (\hat{\mathbf{n}}_j \cdot \hat{\boldsymbol{\eta}}_j) \right). \end{aligned} \quad (3.13)$$

Using  $\nabla_i |\mathbf{e}_{j+1}| = -\mathbf{e}_{j+1}/|\mathbf{e}_{j+1}|$ ,  $\nabla_i |\mathbf{e}_{j+1} - \mathbf{e}_j| = 0$ , this simplifies to

$$\begin{aligned} \mathbf{F}_i^{(curv)} = \frac{4K_c}{\varepsilon} \sum_{j=1}^n & \left( \frac{1 - \hat{\mathbf{n}}_j \cdot \hat{\mathbf{n}}_{j+1}}{1 + \hat{\mathbf{n}}_j \cdot \hat{\mathbf{n}}_{j+1}} \frac{\mathbf{e}_{j+1}}{|\mathbf{e}_{j+1}|} + \frac{2|\mathbf{e}_{j+1}|}{(1 + \hat{\mathbf{n}}_j \cdot \hat{\mathbf{n}}_{j+1})^2} \nabla_i (\hat{\mathbf{n}}_j \cdot \hat{\mathbf{n}}_{j+1}) \right. \\ & \left. + \frac{2|\mathbf{e}_{j+1} - \mathbf{e}_j|}{(1 + \hat{\mathbf{n}}_j \cdot \hat{\boldsymbol{\eta}}_j)^2} \nabla_i (\hat{\mathbf{n}}_j \cdot \hat{\boldsymbol{\eta}}_j) \right). \end{aligned} \quad (3.14)$$

Now recall that

$$\begin{aligned} \hat{\mathbf{n}}_j \cdot \hat{\mathbf{n}}_{j+1} &= \frac{\mathbf{e}_j \times \mathbf{e}_{j+1}}{|\mathbf{e}_j \times \mathbf{e}_{j+1}|} \cdot \frac{\mathbf{e}_{j+1} \times \mathbf{e}_{j+2}}{|\mathbf{e}_{j+1} \times \mathbf{e}_{j+2}|} \\ &= \frac{(\mathbf{e}_j \cdot \mathbf{e}_{j+1})(\mathbf{e}_{j+1} \cdot \mathbf{e}_{j+2}) - (\mathbf{e}_j \cdot \mathbf{e}_{j+2})(\mathbf{e}_{j+1} \cdot \mathbf{e}_{j+1})}{|\mathbf{e}_j \times \mathbf{e}_{j+1}| |\mathbf{e}_{j+1} \times \mathbf{e}_{j+2}|}, \end{aligned}$$

and so

$$\begin{aligned} \nabla_i (\hat{\mathbf{n}}_j \cdot \hat{\mathbf{n}}_{j+1}) &= \nabla_i \frac{(\mathbf{e}_j \cdot \mathbf{e}_{j+1})(\mathbf{e}_{j+1} \cdot \mathbf{e}_{j+2}) - (\mathbf{e}_j \cdot \mathbf{e}_{j+2})(\mathbf{e}_{j+1} \cdot \mathbf{e}_{j+1})}{|\mathbf{e}_j \times \mathbf{e}_{j+1}| |\mathbf{e}_{j+1} \times \mathbf{e}_{j+2}|} \\ &= \frac{(\mathbf{e}_j \cdot \mathbf{e}_{j+1}) \nabla_i (\mathbf{e}_{j+1} \cdot \mathbf{e}_{j+2}) + (\mathbf{e}_{j+1} \cdot \mathbf{e}_{j+2}) \nabla_i (\mathbf{e}_j \cdot \mathbf{e}_{j+1})}{|\mathbf{e}_j \times \mathbf{e}_{j+1}| |\mathbf{e}_{j+1} \times \mathbf{e}_{j+2}|} \\ &\quad - \frac{(\mathbf{e}_j \cdot \mathbf{e}_{j+2}) \nabla_i (\mathbf{e}_{j+1} \cdot \mathbf{e}_{j+1}) + (\mathbf{e}_{j+1} \cdot \mathbf{e}_{j+1}) \nabla_i (\mathbf{e}_j \cdot \mathbf{e}_{j+2})}{|\mathbf{e}_j \times \mathbf{e}_{j+1}| |\mathbf{e}_{j+1} \times \mathbf{e}_{j+2}|} \\ &\quad - (\hat{\mathbf{n}}_j \cdot \hat{\mathbf{n}}_{j+1}) \left( \frac{\nabla_i |\mathbf{e}_j \times \mathbf{e}_{j+1}|}{|\mathbf{e}_j \times \mathbf{e}_{j+1}|} + \frac{\nabla_i |\mathbf{e}_{j+1} \times \mathbf{e}_{j+2}|}{|\mathbf{e}_{j+1} \times \mathbf{e}_{j+2}|} \right). \end{aligned}$$

To simplify this, we use the facts that

$$\nabla_i |\mathbf{e}_j \times \mathbf{e}_{j+1}| = \frac{\mathbf{e}_j \times \mathbf{e}_{j+1}}{|\mathbf{e}_j \times \mathbf{e}_{j+1}|} \times (\mathbf{e}_{j+1} - \mathbf{e}_j) = \hat{\mathbf{n}}_j \times (\mathbf{e}_{j+1} - \mathbf{e}_j),$$

and

$$\nabla_i (\mathbf{e}_j \cdot \mathbf{e}_{j+1}) = -(\mathbf{e}_j + \mathbf{e}_{j+1}).$$

The result is

$$\begin{aligned} \nabla_i (\hat{\mathbf{n}}_j \cdot \hat{\mathbf{n}}_{j+1}) &= (\hat{\mathbf{n}}_{j+1} - (\hat{\mathbf{n}}_j \cdot \hat{\mathbf{n}}_{j+1}) \hat{\mathbf{n}}_j) \times \frac{\mathbf{e}_{j+1} - \mathbf{e}_j}{|\mathbf{e}_j \times \mathbf{e}_{j+1}|} \\ &\quad + (\hat{\mathbf{n}}_j - (\hat{\mathbf{n}}_j \cdot \hat{\mathbf{n}}_{j+1}) \hat{\mathbf{n}}_{j+1}) \times \frac{\mathbf{e}_{j+2} - \mathbf{e}_{j+1}}{|\mathbf{e}_{j+1} \times \mathbf{e}_{j+2}|}. \end{aligned}$$

Then using

$$\nabla_i (\hat{\mathbf{n}}_j \cdot \hat{\boldsymbol{\eta}}_j) = \nabla_i \left[ \frac{\mathbf{e}_j \times \mathbf{e}_{j+1}}{|\mathbf{e}_j \times \mathbf{e}_{j+1}|} \cdot \hat{\boldsymbol{\eta}}_j \right] = (\hat{\boldsymbol{\eta}}_j - (\hat{\mathbf{n}}_j \cdot \hat{\boldsymbol{\eta}}_j) \hat{\mathbf{n}}_j) \times \frac{\mathbf{e}_{j+1} - \mathbf{e}_j}{|\mathbf{e}_j \times \mathbf{e}_{j+1}|},$$

we are left with

$$\begin{aligned}
\mathbf{F}_i^{(curv)} = \frac{4K_c}{\varepsilon} \sum_{j=1}^n & \left( \frac{1 - \hat{\mathbf{n}}_j \cdot \hat{\mathbf{n}}_{j+1}}{1 + \hat{\mathbf{n}}_j \cdot \hat{\mathbf{n}}_{j+1}} \frac{\mathbf{e}_{j+1}}{|\mathbf{e}_{j+1}|} \right. \\
& + \frac{2|\mathbf{e}_{j+1}|}{(1 + \hat{\mathbf{n}}_j \cdot \hat{\mathbf{n}}_{j+1})^2} \left[ (\hat{\mathbf{n}}_{j+1} - (\hat{\mathbf{n}}_j \cdot \hat{\mathbf{n}}_{j+1})\hat{\mathbf{n}}_j) \times \frac{\mathbf{e}_{j+1} - \mathbf{e}_j}{|\mathbf{e}_j \times \mathbf{e}_{j+1}|} \right. \\
& \quad \left. \left. + (\hat{\mathbf{n}}_j - (\hat{\mathbf{n}}_j \cdot \hat{\mathbf{n}}_{j+1})\hat{\mathbf{n}}_{j+1}) \times \frac{\mathbf{e}_{j+2} - \mathbf{e}_{j+1}}{|\mathbf{e}_{j+1} \times \mathbf{e}_{j+2}|} \right] \right. \\
& \left. + \frac{2|\mathbf{e}_{j+1} - \mathbf{e}_j|}{(1 + \hat{\mathbf{n}}_j \cdot \hat{\boldsymbol{\eta}}_j)^2} (\hat{\boldsymbol{\eta}}_j - (\hat{\mathbf{n}}_j \cdot \hat{\boldsymbol{\eta}}_j)\hat{\mathbf{n}}_j) \times \frac{\mathbf{e}_{j+1} - \mathbf{e}_j}{|\mathbf{e}_j \times \mathbf{e}_{j+1}|} \right). \tag{3.15}
\end{aligned}$$

Finally, the anti self-intersection force, which we adjust by  $1/\varepsilon^2$  so it vanishes smoothly when  $|\mathbf{p}_j - \mathbf{p}_i| = \varepsilon$ ,

$$\mathbf{F}_i^{(si)} = -12K_{SS} \sum_{\substack{j=1 \\ j \neq i}}^{N_p} \left\{ \begin{array}{l} \frac{\varepsilon^{12}(\mathbf{p}_j - \mathbf{p}_i)}{|\mathbf{p}_j - \mathbf{p}_i|^{14}} - \frac{1}{\varepsilon^2} \quad |\mathbf{p}_j - \mathbf{p}_i| < \varepsilon \\ \mathbf{p}_i, \mathbf{p}_j \text{ do not share an edge} \\ 0 \quad |\mathbf{p}_j - \mathbf{p}_i| \geq \varepsilon \text{ or} \\ \mathbf{p}_i, \mathbf{p}_j \text{ share an edge} \end{array} \right. . \tag{3.16}$$

To summarize, the total force  $\mathbf{F}_i$ , then, on a given vertex point  $\mathbf{p}_i$  is given by

$$\begin{aligned}
\mathbf{F}_i = & -12K_{LJ} \sum_{j=1}^M \left( \left( \frac{\varepsilon + r_j}{|\mathbf{q}_j - \mathbf{p}_i|} \right)^{12} - \left( \frac{\varepsilon + r_j}{|\mathbf{q}_j - \mathbf{p}_i|} \right)^6 \right) \frac{\mathbf{q}_j - \mathbf{p}_i}{|\mathbf{q}_j - \mathbf{p}_i|^2} \\
& - \frac{K_b}{6V_0} (V - V_0) \sum_{j=1}^n (\mathbf{q}_j \times \mathbf{q}_{j+1}) - \frac{T}{4} \sum_{j=1}^n \hat{\mathbf{n}}_j \times (\mathbf{q}_{j+1} - \mathbf{q}_j) \\
& + \frac{4K_c}{\varepsilon} \sum_{j=1}^n \left( \frac{1 - \hat{\mathbf{n}}_j \cdot \hat{\mathbf{n}}_{j+1}}{1 + \hat{\mathbf{n}}_j \cdot \hat{\mathbf{n}}_{j+1}} \frac{\mathbf{e}_{j+1}}{|\mathbf{e}_{j+1}|} \right. \\
& \quad + \frac{2|\mathbf{e}_{j+1}|}{(1 + \hat{\mathbf{n}}_j \cdot \hat{\mathbf{n}}_{j+1})^2} \left[ (\hat{\mathbf{n}}_{j+1} - (\hat{\mathbf{n}}_j \cdot \hat{\mathbf{n}}_{j+1})\hat{\mathbf{n}}_j) \times \frac{\mathbf{e}_{j+1} - \mathbf{e}_j}{|\mathbf{e}_j \times \mathbf{e}_{j+1}|} \right. \\
& \quad \quad \left. \left. + (\hat{\mathbf{n}}_j - (\hat{\mathbf{n}}_j \cdot \hat{\mathbf{n}}_{j+1})\hat{\mathbf{n}}_{j+1}) \times \frac{\mathbf{e}_{j+2} - \mathbf{e}_{j+1}}{|\mathbf{e}_{j+1} \times \mathbf{e}_{j+2}|} \right] \right. \\
& \quad \left. + \frac{2|\mathbf{e}_{j+1} - \mathbf{e}_j|}{(1 + \hat{\mathbf{n}}_j \cdot \hat{\mathbf{n}}_j)^2} (\hat{\boldsymbol{\eta}}_j - (\hat{\mathbf{n}}_j \cdot \hat{\boldsymbol{\eta}}_j)\hat{\mathbf{n}}_j) \times \frac{\mathbf{e}_{j+1} - \mathbf{e}_j}{|\mathbf{e}_j \times \mathbf{e}_{j+1}|} \right) \\
& - 12K_{SS} \sum_{\substack{j=1 \\ j \neq i}}^{N_p} \begin{cases} \frac{\varepsilon^{12}(\mathbf{p}_j - \mathbf{p}_i)}{|\mathbf{p}_j - \mathbf{p}_i|^{14}} - \frac{1}{\varepsilon^2} & |\mathbf{p}_j - \mathbf{p}_i| < \varepsilon, \\ & \mathbf{p}_i, \mathbf{p}_j \text{ do not share an edge} \\ 0 & |\mathbf{p}_j - \mathbf{p}_i| \geq \varepsilon \text{ or} \\ & \mathbf{p}_i, \mathbf{p}_j \text{ share an edge} \end{cases} . \tag{3.17}
\end{aligned}$$

### 3.2.5 Two-dimensional approximation

In many cases, we wish to perform simulations in two dimensions, for simplicity. The method we adopt for this is to consider the cell to be a cylinder of thickness  $\varepsilon$  with vertical walls, as shown in Figure 3.2.5. In this scenario, the perimeter is divided into rectangles, which can be further divided into triangles if desired, but such subdivision is unnecessary because each rectangle is planar. We suppose that the top and bottom surface are fixed, hence force computations are irrelevant, and we limit our attention to the narrow edge.

If we consider the cell to be lying on the  $x - y$  plane, and we number the vertical edges of the rectangles that form its boundary as  $\mathbf{p}_i$ ,  $i \in \{1, \dots, N_p\}$ , proceeding in a counterclockwise direction as viewed from a point with positive  $z$  coordinate, as

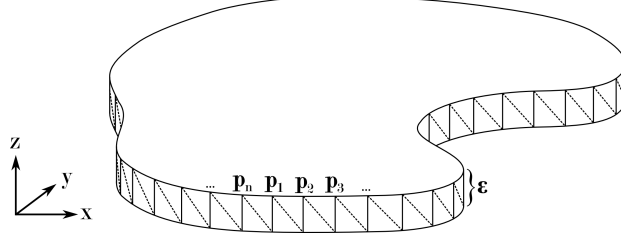


Figure 3.2: A method for generating a two-dimensional approximation of a cell for simplified simulations.

shown in Figure 3.2.5.

Under this two dimensional simplification, (3.4), (3.5), (3.7), and (3.9) remain valid, but we compute surface area  $A_i$  of a perimeter rectangle using  $A_i = \varepsilon |\mathbf{p}_{i+1} - \mathbf{p}_i|$ , and compute cell volume  $V$  using

$$V = \frac{\varepsilon}{2} \sum_{i=1}^{N_p} (x_i y_{i+1} - y_i x_{i+1}) ,$$

where the two-dimensional coordinates of  $\mathbf{p}_i$  are  $(x_i, y_i)$ .

The curvature energy simplifies slightly due to the constrained geometry,

$$E^{(curv)} = 4K_c \sum_{i=1}^{N_p} \frac{1 - \hat{\mathbf{n}}_i \cdot \hat{\mathbf{n}}_{i+1}}{1 + \hat{\mathbf{n}}_i \cdot \hat{\mathbf{n}}_{i+1}} . \quad (3.18)$$

In the above, we have made use of the identifications  $\hat{\mathbf{n}}_{N_p+1} \equiv \hat{\mathbf{n}}_1$  and  $\mathbf{p}_{N_p+1} \equiv \mathbf{p}_1$  to allow the sums to close the boundary.

### 3.2.6 Force in the two-dimensional approximation

Under the constrained geometry of the two-dimensional approximation discussed in 3.2.5, the force simplifies somewhat. Only the curvature term presents some complexity. If we use  $\mathbf{e}_i$  to denote edge  $\mathbf{p}_{i+1} - \mathbf{p}_i$ , and let  $\hat{\mathbf{e}}_i = \mathbf{e}_i / |\mathbf{e}_i|$ , then  $\hat{\mathbf{n}}_i \cdot \hat{\mathbf{n}}_{i+1} = \hat{\mathbf{e}}_i \cdot \hat{\mathbf{e}}_{i+1}$ , and so

$$F_i^{(curv)} = -4K_c \nabla_i \left[ \frac{1 - \hat{\mathbf{e}}_i \cdot \hat{\mathbf{e}}_{i+1}}{1 + \hat{\mathbf{e}}_i \cdot \hat{\mathbf{e}}_{i+1}} + \frac{1 - \hat{\mathbf{e}}_{i-1} \cdot \hat{\mathbf{e}}_i}{1 + \hat{\mathbf{e}}_{i-1} \cdot \hat{\mathbf{e}}_i} + \frac{1 - \hat{\mathbf{e}}_{i-2} \cdot \hat{\mathbf{e}}_{i-1}}{1 + \hat{\mathbf{e}}_{i-2} \cdot \hat{\mathbf{e}}_{i-1}} \right] ,$$

where as before, vertex position affects curvature at the vertex and also at adjacent vertices, yielding three terms. Computing gradients,

$$F_i^{(curv)} = 8K_c \left[ \frac{\nabla_i(\hat{\mathbf{e}}_i \cdot \hat{\mathbf{e}}_{i+1})}{(1 + \hat{\mathbf{e}}_i \cdot \hat{\mathbf{e}}_{i+1})^2} + \frac{\nabla_i(\hat{\mathbf{e}}_{i-1} \cdot \hat{\mathbf{e}}_i)}{(1 + \hat{\mathbf{e}}_{i-1} \cdot \hat{\mathbf{e}}_i)^2} + \frac{\nabla_i(\hat{\mathbf{e}}_{i-2} \cdot \hat{\mathbf{e}}_{i-1})}{(1 + \hat{\mathbf{e}}_{i-2} \cdot \hat{\mathbf{e}}_{i-1})^2} \right].$$

The gradients of the dot products are given by

$$\begin{aligned} \nabla_i(\hat{\mathbf{e}}_i \cdot \hat{\mathbf{e}}_{i+1}) &= \frac{(\hat{\mathbf{e}}_i \cdot \hat{\mathbf{e}}_{i+1})\hat{\mathbf{e}}_i - \hat{\mathbf{e}}_{i+1}}{|\mathbf{e}_i|}, \\ \nabla_i(\hat{\mathbf{e}}_{i-1} \cdot \hat{\mathbf{e}}_i) &= \frac{\mathbf{e}_i - \mathbf{e}_{i-1} - (\hat{\mathbf{e}}_{i-1} \cdot \hat{\mathbf{e}}_i)[|\mathbf{e}_i|\hat{\mathbf{e}}_{i-1} - |\mathbf{e}_{i-1}|\hat{\mathbf{e}}_i]}{|\mathbf{e}_{i-1}||\mathbf{e}_i|}, \text{ and} \\ \nabla_i(\hat{\mathbf{e}}_{i-2} \cdot \hat{\mathbf{e}}_{i-1}) &= \frac{\hat{\mathbf{e}}_{i-2} - (\hat{\mathbf{e}}_{i-2} \cdot \hat{\mathbf{e}}_{i-1})\hat{\mathbf{e}}_{i-1}}{|\mathbf{e}_{i-1}|}. \end{aligned}$$

Applying these, we obtain

$$\begin{aligned} F_i^{(curv)} &= 8K_c \left[ \frac{(\hat{\mathbf{e}}_i \cdot \hat{\mathbf{e}}_{i+1})\hat{\mathbf{e}}_i - \hat{\mathbf{e}}_{i+1}}{|\mathbf{e}_i|(1 + \hat{\mathbf{e}}_i \cdot \hat{\mathbf{e}}_{i+1})^2} + \frac{\mathbf{e}_i - \mathbf{e}_{i-1} + (\hat{\mathbf{e}}_{i-1} \cdot \hat{\mathbf{e}}_i)(|\mathbf{e}_{i-1}|\hat{\mathbf{e}}_i - |\mathbf{e}_i|\hat{\mathbf{e}}_{i-1})}{|\mathbf{e}_{i-1}||\mathbf{e}_i|(1 + \hat{\mathbf{e}}_{i-1} \cdot \hat{\mathbf{e}}_i)^2} \right. \\ &\quad \left. + \frac{\hat{\mathbf{e}}_{i-2} - (\hat{\mathbf{e}}_{i-2} \cdot \hat{\mathbf{e}}_{i-1})\hat{\mathbf{e}}_{i-1}}{|\mathbf{e}_{i-1}|(1 + \hat{\mathbf{e}}_{i-2} \cdot \hat{\mathbf{e}}_{i-1})^2} \right], \end{aligned} \tag{3.19}$$

and the complete two-dimensional analog to (3.17) is

$$\begin{aligned} \mathbf{F}_i &= -12K_{LJ} \sum_{j=1}^M \left( \left( \frac{\varepsilon + r_j}{|\mathbf{q}_j - \mathbf{p}_i|} \right)^{12} - \left( \frac{\varepsilon + r_j}{|\mathbf{q}_j - \mathbf{p}_i|} \right)^6 \right) \frac{\mathbf{q}_j - \mathbf{p}_i}{|\mathbf{q}_j - \mathbf{p}_i|^2} \\ &\quad - \frac{\varepsilon K_b}{2V_0} (V - V_0) \begin{bmatrix} y_{i+1} - y_{i-1} \\ x_{i-1} - x_{i+1} \end{bmatrix} - \frac{T\varepsilon}{2} (\mathbf{e}_{i-1} - \mathbf{e}_i) \\ &\quad + 8K_c \left[ \frac{(\hat{\mathbf{e}}_i \cdot \hat{\mathbf{e}}_{i+1})\hat{\mathbf{e}}_i - \hat{\mathbf{e}}_{i+1}}{|\mathbf{e}_i|(1 + \hat{\mathbf{e}}_i \cdot \hat{\mathbf{e}}_{i+1})^2} + \frac{\mathbf{e}_i - \mathbf{e}_{i-1} + (\hat{\mathbf{e}}_{i-1} \cdot \hat{\mathbf{e}}_i)(|\mathbf{e}_{i-1}|\hat{\mathbf{e}}_i - |\mathbf{e}_i|\hat{\mathbf{e}}_{i-1})}{|\mathbf{e}_{i-1}||\mathbf{e}_i|(1 + \hat{\mathbf{e}}_{i-1} \cdot \hat{\mathbf{e}}_i)^2} \right. \\ &\quad \left. + \frac{\hat{\mathbf{e}}_{i-2} - (\hat{\mathbf{e}}_{i-2} \cdot \hat{\mathbf{e}}_{i-1})\hat{\mathbf{e}}_{i-1}}{|\mathbf{e}_{i-1}|(1 + \hat{\mathbf{e}}_{i-2} \cdot \hat{\mathbf{e}}_{i-1})^2} \right] \\ &\quad - 12K_{SS} \sum_{\substack{j=1 \\ j \neq i}}^{N_p} \begin{cases} \frac{\varepsilon^{12}(\mathbf{p}_j - \mathbf{p}_i)}{|\mathbf{p}_j - \mathbf{p}_i|^{14}} & |\mathbf{p}_j - \mathbf{p}_i| < \varepsilon, \text{ and } \mathbf{p}_i, \mathbf{p}_j \text{ not adjacent} \\ 0 & |\mathbf{p}_j - \mathbf{p}_i| \geq \varepsilon \text{ or } \mathbf{p}_i, \mathbf{p}_j \text{ adjacent} \end{cases}. \end{aligned} \tag{3.20}$$

### 3.2.7 Simulation results

An example of simulated two-dimensional membrane behavior are shown in Figure 3.2.7. Here, a fixed boundary was placed around a circular membrane composed of

300 model elements, then a rigid circular probe under constant force was introduced and allowed to collide with the membrane. It can be seen that membrane volume is preserved, but surface area increases as the membrane deforms. Model elements are added as the perimeter expands to maintain a spacing between elements that falls within a target range.

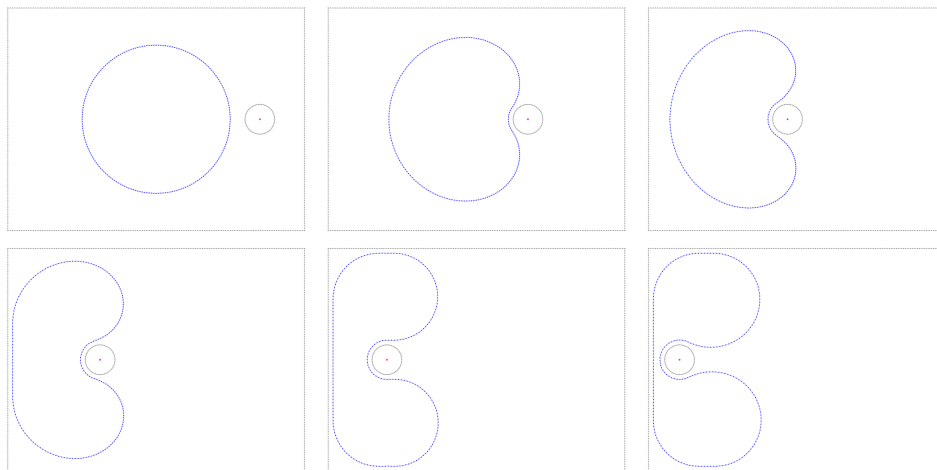


Figure 3.3: A simulation of a two-dimensional membrane reacting to a rigid probe under constant force.

### 3.3 Cytoskeleton and signal transduction

In the computation above, we have assumed that the internal energy of a cell under compression is due to the deformation of the membrane as well as the pressure of the cytoplasm. In reality, however, a cell possesses internal cytoskeleton giving it additional rigidity. The purpose of this section is to model a cytoskeleton using a computationally reasonable number of elements.

Cell shape is modulated by an internal cytoskeleton that is constructed and dismantled dynamically within the cytoplasm [43, 44]. The cytoskeleton is a network of

interlinked polymer filaments in the interior of a cell (if we disregard blebbing, where the membrane opens and cytoskeleton protrudes outside the cell). There are different types of polymers that make up the cytoskeleton, but the most abundant and most directly related to cell motion is actin. Actin filaments are very small (typically 6–8 nm in diameter [45]) and form a dense network that is concentrated near the cortex of the cell [46]. Actin filaments are linked to trans-membrane proteins in the plasma membrane, and cross-link among themselves to provide rigidity and shape to the cell. They polymerize and depolymerize continuously, with half-lives on the order of tens of minutes, and display asymmetric growth, preferring to add new monomers on one end during polymerization and lose them from the other during depolymerization [45], a phenomenon known as *treadmilling*. During motility, the leading edge of the cell is characterized by formation of new microfilaments [47]. A number of proteins affect actin microfilament polymerization or depolymerization [48–50], sever existing microfilaments [51–54], or bind microfilaments together [55–57]. Other trans-membrane proteins bind to the actin cytoskeleton to promote adhesion.

The other primary constituents of the cytoskeletal framework are microtubules and intermediate filaments. Microtubules are the stiffest cytoskeletal structures, helical arrangements of the protein tubulin on the order of 25 nm in diameter [45], which form a highly dynamic network, with a typical lifetime on the order of a few minutes for a microtubule [58, 59]. The primary role of microtubules appears to be the transport of vesicles and organelles within a cell, but they also act to regulate actin behavior and play a role in polarizing a cell and determining its direction of motion [60–62]. In interphase (non-dividing) cells, most microtubules are attached to a centrosome near the cell nucleus and project outward toward the periphery of the cell [44, 46, 63]. During cell movement, the centrosome tends to move toward the cell’s leading edge [64].

Intermediate filaments consist of polymers based on a variety of different proteins (keratins, desmin, GFAP, vimentin, and others) [65–67]. The proteins form coiled coils then tetramers which align into protofilaments, then aggregate into rope-like filaments on the order of 10nm in size [45]. The intermediate filament network is also a dynamic system, but changes in its structure are not correlated with cell movement as are those of actin microfilaments or microtubules [68,69]. Rather, its role appears to be inter-cell communication and transport of proteins [70–72].

Some data taken from [45] regarding the mechanical properties of the various forms of cytoskeletal structures are included in Table 3.3.

Table 3.3: Mechanical properties of cytoskeletal filaments

	Diameter (nm)	Persistence Length ( $\mu\text{m}$ )	Bending Stiffness ( $\text{Nm}^2$ )	Young's Modulus (Pa)
Actin microfilament	6–8	15	$7 \times 10^{-26}$	$1.3\text{--}2.5 \times 10^9$
Microtubule	25	6000	$2.6 \times 10^{-23}$	$1.9 \times 10^9$
Intermediate filament	10	$\sim 1$	$4 \times 10^{-27}$	$1 \times 10^9$

### 3.3.1 Current Models of Cell Shape Modulation

Early models of cytoskeletal dynamics and its role in shape modulation were simple molecular-level hypotheses of how particular observed behaviors occurred [73–76]. Subsequent modeling efforts were more general, including lattice [77], kinetic [78–80], and continuum models [81]. Recent efforts have extended and improved on these works [82–84], but still model only a subset of cytoskeletal behavior (for example, actin network dynamics, microtubule dynamics, intermediate filament dynamics, or the dynamics of links with transmembrane adhesion proteins). At present, there is no unified model of cell behavior that integrates these disparate models, but some

models generalize cell behavior as a whole without trying to account for contributions from these individual factors [85–88].

### 3.3.2 Modeling actin as a collection of linked spheres

We present a simple but effective model of cytoskeletal actin that exhibits robust chemotactic behavior. In the spirit of the component models described in the introduction, we model actin filaments in the cytoskeleton of a cell as a collection of spherical model elements connected by springs that interact with each other and with membrane model elements.

Consider a cell domain  $\mathcal{C}$ , with boundary membrane  $\Omega_{\mathcal{C}}$ , consisting of model elements as described in the prior section. We attach an actin filament to each membrane model element, with a number of linked spheres proportional to the length of the filament. This situation is shown for the two-dimensional case in Figure 3.3.2, but the three-dimensional case is analogous.

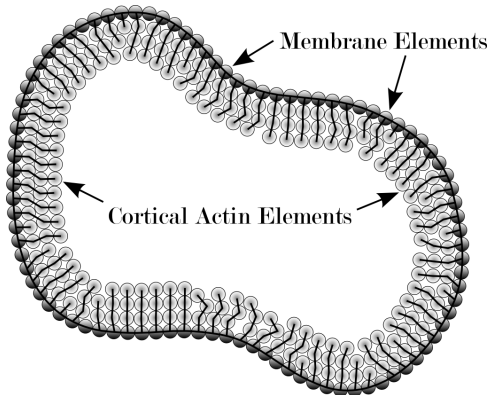


Figure 3.4: An initial arrangement of cortical actin model elements in a cell

We equip these spheres with a simple Lennard-Jones potential and a Hooke’s law spring connection, with spring constant  $K_s$ , to either the adjacent spheres in the filament, or the membrane element in the case of the first sphere in a filament, and

allow them to interact with each other and with membrane elements. The attraction generated by this potential between nearby elements models the crosslinking of actin filaments within the cytoskeleton. This results in a level of mechanical stiffness in areas where the cortical actin elements are not simple monolayers. The degree of rigidity, provided by the Lennard-Jones attraction, can be controlled by the potential well depth  $K_{LJ}$ . If we denote the spheres of the the actin filament attached to membrane element  $\mathbf{p}_i$  by  $\{\mathbf{q}_{i,1}, \dots, \mathbf{q}_{i,m_i}\}$  with radii  $\{r_{i,1}, \dots, r_{i,m_i}\}$ , and assign a fixed radius  $R$  to membrane elements, the energy functional for cortical actin is given by

$$\begin{aligned}
E = & K_{LJ} \sum_{i=1}^n \sum_{k \neq i}^n \left( \left( \frac{r_i + r_k}{|\mathbf{q}_k - \mathbf{q}_i|} \right)^{12} - 2 \left( \frac{r_i + r_k}{|\mathbf{q}_k - \mathbf{q}_i|} \right)^6 \right) \\
& + \frac{K_s}{2} \sum_{i=1}^n (|\mathbf{p}_i - \mathbf{q}_{i,1}| - (R + r_{i,1}))^2 \\
& + \frac{K_s}{2} \sum_{i=1}^n \sum_{j=1}^{m_i-1} (|\mathbf{q}_{i,j} - \mathbf{q}_{i,j+1}| - (r_{i,j} + r_{i,j+1}))^2,
\end{aligned} \tag{3.21}$$

where the inner summation in the Lennard-Jones term is taken over other all actin elements within the same cell as well as the membrane elements in that cell. The force  $\mathbf{F}_{i,1}$  on the leading actin element  $\mathbf{q}_{i,1}$  in the  $i$ -th filament is given by

$$\begin{aligned}
\mathbf{F}_{i,1} = & 12K_{LJ} \sum_{j \neq i} \frac{\mathbf{q}_i - \mathbf{q}_j}{|\mathbf{q}_j - \mathbf{q}_i|^2} \left[ \left( \frac{r_i + r_j}{|\mathbf{q}_j - \mathbf{q}_i|} \right)^6 - 1 \right] \left( \frac{r_i + r_j}{|\mathbf{q}_j - \mathbf{q}_i|} \right)^6 \\
& + K_s (\mathbf{p}_i - \mathbf{q}_{i,1}) (|\mathbf{p}_i - \mathbf{q}_{i,1}| - (R + r_{i,1})) \\
& + K_s (\mathbf{q}_{i,2} - \mathbf{q}_{i,1}) (|\mathbf{q}_{i,1} - \mathbf{q}_{i,2}| - (r_{i,1} + r_{i,2})),
\end{aligned} \tag{3.22}$$

where we disregard the last term if the filament contains only one element. The force on other actin elements  $\mathbf{q}_{i,j}$   $j > 1$  in the filament is given by

$$\begin{aligned}
\mathbf{F}_{i,j} = & 12K_{LJ} \sum_{j \neq i} \frac{\mathbf{q}_i - \mathbf{q}_j}{|\mathbf{q}_j - \mathbf{q}_i|^2} \left[ \left( \frac{r_i + r_j}{|\mathbf{q}_j - \mathbf{q}_i|} \right)^6 - 1 \right] \left( \frac{r_i + r_j}{|\mathbf{q}_j - \mathbf{q}_i|} \right)^6 \\
& + K_s (\mathbf{q}_{i,j-1} - \mathbf{q}_{i,1}) (|\mathbf{q}_{i,j} - \mathbf{q}_{i,j-1}| - (r_{i,j} + r_{i,j-1})) \\
& + K_s (\mathbf{q}_{i,j+1} - \mathbf{q}_{i,1}) (|\mathbf{q}_{i,j} - \mathbf{q}_{i,j+1}| - (r_{i,j} + r_{i,j+1})),
\end{aligned} \tag{3.23}$$

where here we disregard the last term if the element is the last in its filament. Where actin interacts via Lennard-Jones or spring forces with membrane elements we will, of course, make the appropriate additions of opposite forces to those membrane elements.

### 3.3.3 Signal transduction

There are two simple models of chemical signal we can adopt - a particle or a continuum model. In a particle model, a source of signal emits particles at a rate determined by its signaling strength, and those particles diffuse through the surrounding environment until they either decay naturally or encounter a receptor, which is then activated by the signal. In a continuum model, the source has a particular strength, and all receptors in the model are activated based on their distance from the source and on the decay curve of the signal over distance. The difficulty with a continuum model is that it does not take into account that our simulation space is neither isotropic nor homogeneous, and so direct distance computations inherently ignore critical phenomena. Such a system allows signals to diffuse through plasma membranes at the same rate as through ECM or cytoplasm, for example. To adjust the continuum model to factor in densities and diffusion constants for various regions makes the model difficult to implement. In a particle model, on the other hand, diffusion is controlled by local conditions, making the model very simple and facilitating distributed computation. However, this comes with the understanding that in order to accurately simulate continuous chemical diffusion, a large number of diffusing particles will be necessary.

Our model supports sources of chemical signal. A source has characteristics that govern how fast it releases signal particles, and how much total signal it is allowed to release (perhaps infinite). It may have a signaling curve that describes signal levels emitted over time through the effective life of the source. For example, we can

define a set of point sources with infinite lifetime and slow diffusion rate to create a constant gradient in a sample, or we could define a point source with fast release rate and very short lifetime to simulate the release of neurotransmitter from an axon. Once released, the signal diffuses through its surroundings under Brownian motion, or decays probabilistically with a given half-life.

### **3.3.4 Signal particle detection and activation**

Model elements can act as receptors, transmitters, or both. For example, membrane elements (which carry embedded transmembrane proteins) act as receptors of extracellular signals, and transmitters of inter-cellular signals, providing a transduction mechanism that allows the cell to react to its local environment. When a signal particle encounters (comes within a threshold distance of) a receptor that is sensitive to that signal, the signal particle is consumed, and the receptor becomes “activated”. Activation level is simply a signed number associated with the receptor, where receipt of a signal adds or subtracts some fixed value to the receptor’s activation level. The receptor’s response to activation levels is model-dependent. For example, a membrane model element may use its activation to allow ions to flow through a channel, in which case the receptor acts as a signal source to generate ions on the interior side of the membrane, with the number of ions the source can generate proportional to the activation level of the receptor. These ions are then received by nearby cortical actin elements, which causes changes in polymerization levels, as described below.

### **3.3.5 Actin dynamics and treadmilling**

Actin filaments respond to the activation levels of their parent membrane element by adjusting their polymerization. Within a cell, there exists a fixed pool of actin monomer, meaning that over time, the amount of polymerized actin should remain

constant. During cell evolution, membrane elements detect attractant or repellent signals, and take on positive or negative activation levels, respectively. Where a membrane element has a positive activation level, we simulate polymerization of actin by adding or increasing the size of actin model elements in the filament attached to that membrane element. Filaments depolymerize in response to negative activation levels, in which case we shrink or remove elements from the filament. After processing membrane element signals, we apply a global adjustment to all actin filaments such that the total volume of actin elements (polymerized actin) in the cell is conserved.

More formally, if a cell consists of actin elements  $\mathbf{q}_i$ ,  $1 \leq i \leq n$ , and element  $\mathbf{q}_i$  has activation level  $\alpha_i \in \mathbb{R}$ , then the mean activation  $\bar{\alpha}$  per element in the cell is given by

$$\bar{\alpha} = \frac{1}{n} \sum_{i=1}^n \alpha_i. \quad (3.24)$$

From this, we compute the volume change  $\delta V_i$  for the element as

$$\delta V_i = \frac{(\alpha_i - \bar{\alpha})}{\bar{\alpha}} V_i, \quad (3.25)$$

where  $V_i$  is the current volume of  $\mathbf{q}_i$  (above average activation causes growth, below-average causes shrinkage).

Actin filaments preferentially polymerize at their barbed end, and depolymerize at their pointed end, where the barbed end is attached to the membrane, resulting in *treadmilling* as monomers are added at one end and slowly migrate to the other end as the polymer absorbs and releases monomers. We model this by processing polymerization events at the end of the filament that is attached to the membrane, and depolymerization events at the opposite (free) end. The process is illustrated in Figure 3.3.5. We first designate a maximum size for actin model elements. To polymerize a filament, we either enlarge the leading (membrane-attached) actin element, or if that element is already at the maximum size, we create a new, small element and

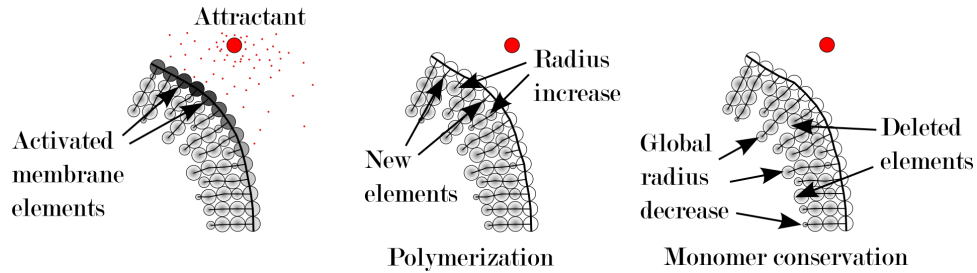


Figure 3.5: Signal transduction and actin dynamics

insert it between the membrane and the first element of the filament. When depolymerizing, we decrease the size of the trailing (free end) actin element, and when that size reaches zero, delete the element. In this way, filaments grow and shrink smoothly, exhibiting the expected treadmilling effects. In regions of positive membrane activation, polymerization of filaments at the membrane-attached end causes an outward force that projects the cell in the direction of the attractive signal source, generating a chemotactic response. In regions of negative activation, the actin depolymerization results in reduced rigidity, which allows the trailing edge of the cell to shift forward and follow the advancing leading edge while preserving cell volume.

### Simulation results

Results from this simple model of cytoskeletal dynamics reveal that it captures many of the behaviors of actin networks that are essential to cell motility. Figure 3.3.5 shows the results of a simulation of a cell with cortical actin cytoskeleton, in the presence of a diffusing chemical attractant. The cell consisted of 200 membrane model elements and 800 actin elements. Cell polarization and the formation of lamellipodia and resulting chemotaxis is clearly visible.

In Figure 3.3.5, we allow the source of attractant signal to move at a fixed rate, causing the cell to pursue the attractant.

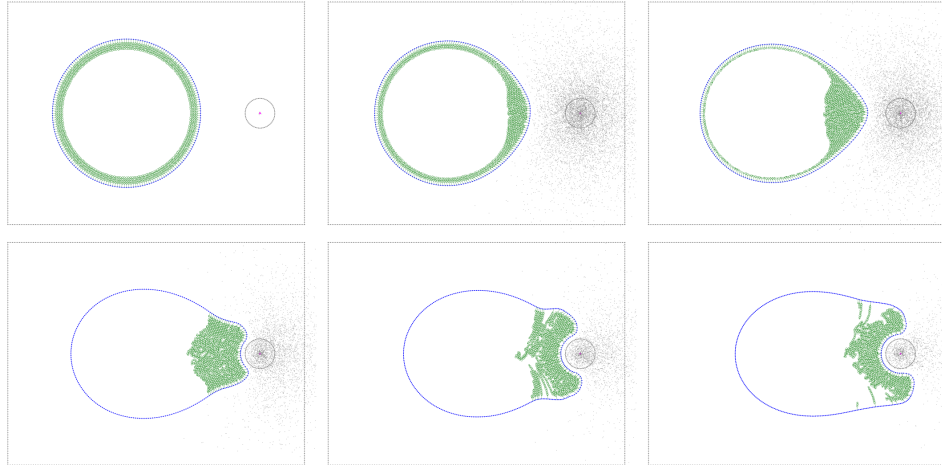


Figure 3.6: Simulation of cells with cortical actin cytoskeleton, and source of diffusing chemical attractant.

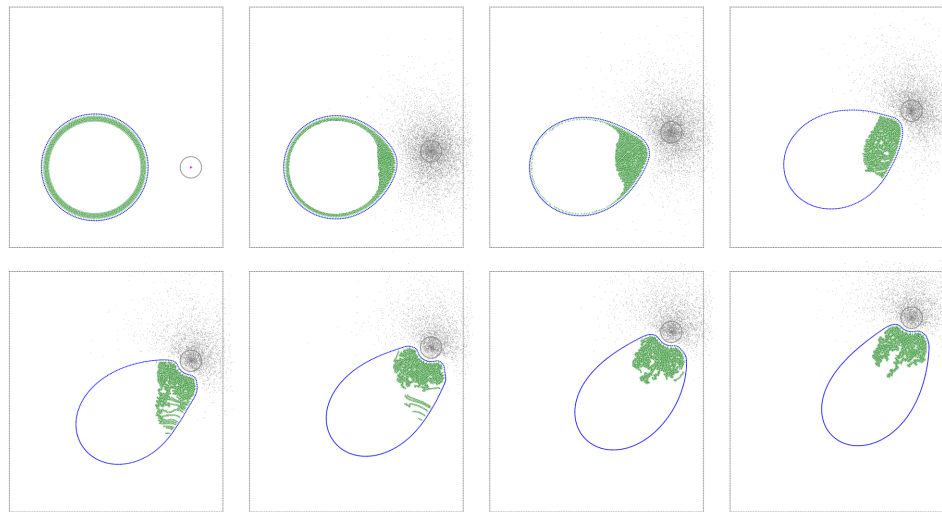


Figure 3.7: Simulation of a cell pursuing a diffusing chemical attractant under constant motion.

### 3.4 Conclusions

While the accurate modeling of cells and cell behavior remains one of the most challenging problems facing computational biology, new models continue to appear that

capture with increasing fidelity the diverse behavior of cells and cell aggregates. Our mesoscale models show that at scales of a few thousand model elements per cell, behavior that includes cell polarization, lamellipodia formation, and chemotaxis can be demonstrated. Further refinement in these models, guided by empirical observations and measurements, will only improve their accuracy.

Certainly, the models presented in the present work represent a simple foray into meso-scale discrete representations of cells and cell structures, but we hope that our generalized framework for constructing and integrating models of diverse cellular systems can serve as a foundation for further model development and refinement. The complete source code for the authors' implementation of this framework (with which all examples in this chapter were constructed) is included in the Appendix and is freely available on the author's web page [89].

## REFERENCES

- [1] Georgina Fabro, Roberto A. Rovasio, Silvia Civalero, Anat Frenkel, S. Roy Caplan, Michael Eisenbach, and Laura C. Giojalas. Chemotaxis of capacitated rabbit spermatozoa to follicular fluid revealed by a novel directionality-based assay. *Biol Reprod*, 67(5):1565–1571, 2002.
- [2] U. Benjamin Kaupp, Nachiket D. Kashikar, and Ingo Weyand. Mechanisms of sperm chemotaxis. *Annu Rev Physiol*, 70:93–117, March 2008.
- [3] T. N. Behar, A. E. Schaffner, C. A. Colton, R. Somogyi, Z. Olah, C. Lehel, and J. L. Barker. GABA-induced chemokinesis and NGF-induced chemotaxis of embryonic spinal cord neurons. *J Neurosci*, 14(1):29–38, January 1994.
- [4] T. N. Behar, M. M. Dugich-Djordjevic, Y-X. Li, W. Ma, R. Somogyi, X. Wen, E. Brown, C. Scott, R. D. G. McKay, and J. L. Barker. Neurotrophins stimulate chemotaxis of embryonic cortical neurons. *Eur J Neurosci*, 9(12):2561–2570, April 2006.
- [5] Ray Keller. Cell migration during gastrulation. *Curr Opin Cell Biol*, 17(5):533–541, October 2005.
- [6] Andrew D. Luster. Chemokines —chemotactic cytokines that mediate inflammation. *New Engl J Med*, 338(7):436–445, February 1998.
- [7] Joost J. Oppenheim and De Yang. Alarmins: chemotactic activators of immune responses. *Curr Opin Immunol*, 17(4):359–365, August 2005.

- [8] Andrew D. Luster, Ronen Alon, and Ulrich von Andrian. Immune cell migration in inflammation: present and future therapeutic targets. *Nat Immunol*, 6(12):1182–1190, December 2005.
- [9] Jonathan R. Mathias, Benjamin J. Perrin, Ting–Xi Liu, John Kanki, A. Thomas Look, and Anna Huttenlocher. Resolution of inflammation by retrograde chemotaxis of neutrophils in transgenic zebrafish. *J Leukocyte Biol*, 80:1281–1288, September 2006.
- [10] Richard A. F. Clark. *The molecular and cellular biology of wound repair*. Plenum Press, New York, 2nd edition, 1996.
- [11] Reinhard Gillitzer and Matthias Goebeler. Chemokines in cutaneous wound healing. *J Leukocyte Biol*, 69:513–521, April 2001.
- [12] Guo–li Ming, Scott T. Wong, John Henley, Xiao–bing Yuan, Hong–jun Song, Nicholas C. Spitzer, and Mu–ming Poo. Adaptation in the chemotactic guidance of nerve growth cones. *Nature*, 417(6887):411–418, May 2002.
- [13] William J. Rosoff, Jeffrey S. Urbach, Mark A. Esrick, Ryan G. McAllister, Linda J. Richards, and Geoffrey J. Goodhill. A new chemotaxis assay shows the extreme sensitivity of axons to molecular gradients. *Nat Neurosci*, 7(6):678–682, May 2004.
- [14] Duncan Mortimer, Thomas Fothergill, Zac Pujic, Linda J. Richards, and Geoffrey J. Goodhill. Growth cone chemotaxis. *Trends Neurosci*, 31(2):90–98, February 2007.
- [15] Michael Eisenbach. *Chemotaxis*. Imperial College Press, London, 2004.
- [16] Peter J. M. Van Haastert and Peter N. Devreotes. Chemotaxis: signalling the way forward. *Nat Rev Mol Cell Bio*, 5(8):626–634, August 2004.

- [17] Clifford S. Patlak. Random walk with persistence and external bias. *B Math Biophys*, 15(3):311–338, 1953.
- [18] Evelyn F. Keller and Lee A. Segel. Model for chemotaxis. *J Theor Biol*, 30(2):225–234, February 1971.
- [19] M. P. Brenner, P. Constantin, L. P. Kadanoff, A. Schenkel, and S. C. Venkataramani. Diffusion, attraction and collapse. *Nonlinearity*, 12:1071–1098, 1999.
- [20] D. D. Holm and V. Putkaradze. Aggregation of finite sized particles with variable mobility. *Phys. Rev. Lett*, 95:225105, 2005.
- [21] D. D. Holm and V. Putkaradze. Formation of clumps and patches in self-aggregation of finite size particles. *Physica D*, 220:183, 2005.
- [22] A. Bertozzi and T. Laurent. Finite-time blow-up of solutions of an aggregation equation in  $R^n$ . *Communications in Mathematical Physics*, 247:717–735, 2007.
- [23] A. Bertozzi and J. Brandman. Finite-time blow-up of  $L^\infty$ -weak solutions of an aggregation equation. *Communications in Mathematical Sciences*, 8(1):45–65, 2010.
- [24] A. Bertozzi C. Topaz and M. Lewis. A nonlocal continuum model for biological aggregation. *Bull. Math. Biology*, 68:1601–1623, 2006.
- [25] A. Blanchet, J. A. Carrillo, and P. Laurençot. Critical mass for a Patlak–Keller–Segel model with degenerate diffusion in higher dimensions. *Calculus of variations and partial differential equations*, 35(2):133–168, February 2008.
- [26] Eirikur Palsson and Hans G. Othmer. A model for individual and collective cell movement in *Dictyostelium discoideum*. *P Natl Acad Sci USA*, 97(19):10448–10453, September 2000.

- [27] Manolya Eyiurekli. A computational model of chemotaxis-based cell aggregation. Master's thesis, Drexel University, August 2006.
- [28] S. J. Singer and Garth L. Nicolson. Structure of cell membranes. *Science*, 175(4023):720–731, February 1972.
- [29] Ken Jacobson, Ole G. Mouritsen, and Richard G. W. Anderson. Lipid rafts: at a crossroad between cell biology and physics. *Nat Cell Biol*, 9(1):7–14, 2007.
- [30] John Katsaras and Thomas Gutberlet, editors. *Lipid Bilayers – Structure and Interactions*. Biological Physics Series. Springer Verlag, Berlin, 2001.
- [31] Harvey T. McMahon and Jennifer L. Gallop. Membrane curvature and mechanisms of dynamic cell membrane remodelling. *Nat*, 438(7068):531–710, 2005.
- [32] Peter J. Quinn, editor. *Membrane Dynamics and Domains*, volume 37 of *Subcellular Biochemistry*. Kluwer Academic/Plenum Publishers, New York, 2004.
- [33] S. J. Marrink, A. H. de Vries, and D. P. Tieleman. Lipids on the move: Simulations of membrane pores, domains, stalks and curves. *Biochim Biophys Acta*, 1788(1):149–168, 2009.
- [34] Richard G. W. Anderson and Ken Jacobson. A role for lipid shells in targeting proteins to caveolae, rafts, and other lipid domains. *Science*, 296(5574):1821–1825, June 2002.
- [35] D. P. Tieleman, S. J. Marrink, and H. J. C. Berendsen. A computer perspective of membranes: molecular dynamics studies of lipid bilayer systems. *Biochim Biophys Acta*, 1331(3):235–270, November 1997.

- [36] Yee–Hung M. Chan and Steven G. Boxer. Model membrane systems and their applications. *Current Opinion in Chemical Biology*, 11(6):581–587, December 2007.
- [37] Scott E. Feller, editor. *Computational Modeling of Membrane Bilayers*, volume 60 of *Current Topics in Membranes*. Elsevier, Inc., Amsterdam, 2008.
- [38] Gregory A. Voth, editor. *Coarse–graining of Condensed Phase and Biomolecular Systems*. CRC Press, Boca Raton, 2009.
- [39] D. Marsh. Elastic curvature constants of lipid monolayers and bilayers. *Chemistry and Physics of Lipids*, 144(2):146–159, November–December 2006.
- [40] Drazen Raucher and Michael P. Sheetz. Cell spreading and lamellipodial extension rate is regulated by membrane tension. *Journal of Cell Biology*, 148(1):127–136, January 2000.
- [41] Norbert Kučerka, Mikhail A. Kiselev, and Pavel Balgavý. Determination of bilayer thickness and lipid surface area in unilamellar dimyristoylphosphatidylcholine vesicles from small–angle neutron scattering curves: a comparison of evaluation methods. *European Biophysics Journal*, 33(4):328–334, July 2004.
- [42] Drazen Raucher and Michael P. Sheetz. Characteristics of a membrane reservoir buffering membrane tension. *Biophysical Journal*, 77(4):1992–2002, 1999.
- [43] Kinneret Keren and Julie A. Theriot. Biophysical aspects of actin–based cell motility in fish epithelial keratocytes. In Peter Lenz, editor, *Cell Motility*, pages 31–58. Springer Science + Business Media, LLC, New York, 2008.
- [44] Marileen Dogterom, Julien Husson, Liedewij Laan, Laura Munteanu, and Christian Tischer. Microtubule forces and organization. In Peter Lenz, editor, *Cell*

- Motility*, pages 93–115. Springer Science + Business Media, LLC, New York, 2008.
- [45] Mohammad R. K. Mofrad and Roger D. Kamm, editors. *Cytoskeletal Mechanics: models and measurements*. Cambridge University Press, New York, 2006.
- [46] Dennis Bray. *Cell Movements from molecules to motility*. Garland Publishing, New York, 2nd edition, 2001.
- [47] Julie A. Theriot and Timothy J. Mitchison. Actin microfilament dynamics in locomoting cells. *Nature*, 352(6331):126–131, July 1991.
- [48] Alan Weeds and Sutherland Maciver. F-actin capping proteins. *Curr Opin Cell Biol*, 5(1):63–69, February 1993.
- [49] Dorothy A. Schafer and John A. Cooper. Control of actin assembly at filament ends. *Annu Rev Cell Dev Biol*, 11:497–518, November 1995.
- [50] Marie-France Carlier and Dominique Pantaloni. Control of actin dynamics in cell motility. *J Mol Biol*, 269(4):459–467, June 1997.
- [51] Yoram A. Puius, Nicole M. Mahoney, and Steven C. Almo. The modular structure of actin-regulatory proteins. *Curr Opin Cell Biol*, 10(1):23–34, February 1998.
- [52] Hui Qiao Sun, Masaya Yamamoto, Marisan Mejillano, and Helen L. Yin. Gelsolin, a multifunctional actin regulatory protein. *J Biol Chem*, 274(47):33179–33182, November 1999.
- [53] Amy M. McGough, Chris J. Staiger, Jung-Ki Min, and Karen D. Simonetti. The gelsolin family of actin regulatory proteins: modular structures, versatile functions. *FEBS Lett*, 552(2–3):75–81, September 2003.

- [54] Narendra Kumar and Seema Khurana. Identification of a functional switch for actin severing by cytoskeletal proteins. *J Biol Chem*, 279(24):24915–24918, June 2004.
- [55] John H. Hartwig and David J. Kwiatkowski. Actin-binding proteins. *Curr Opin Cell Biol*, 3(1):87–97, February 1991.
- [56] Enrique M. De La Cruz. Actin-binding proteins: An overview. In C. G. dos Remedios and D. D. Thomas, editors, *Molecular interactions of actin-actin structure and actin-binding proteins*, pages 123–134. Springer-Verlag Berlin, 2001.
- [57] Steven J. Winder and Kathryn R. Ayscough. Actin-binding proteins. *J Cell Sci*, 118(4):651–654, 2005.
- [58] Tim Mitchison and Marc Kirschner. Dynamic instability of microtubule growth. *Nature*, 312(5991):237–242, November 1984.
- [59] Arshad Desai and Timothy J. Mitchison. Microtubule polymerization dynamics. *Annu Rev Cell Dev Biol*, 13:83–117, November 1997.
- [60] M. Elbaum, A. Chausovsky, E. T. Levy, M. Shtutman, and A. D. Bershadsky. Microtubule involvement in regulating cell contractility and adhesion-dependent signalling: a possible mechanism for polarization of cell motility. In J. M. Lackie, G. A. Dunn, and G. E. Jones, editors, *Cell Behaviour: Control and Mechanism of Motility*, pages 147–172. Portland Press, London, 1999.
- [61] Fred Chang, Becket Feierbach, and Sophie Martin. Regulation of actin assembly by microtubules in fission yeast cell polarity. In Gregory Bock and Jamie Goode, editors, *Signalling networks in cell shape and motility*, pages 59–72. John Wiley and Sons, Ltd., Chichester, 2005.

- [62] J. Victor Small and Irina Kaverina. Polarized cell motility: microtubules show the way. In Doris Wedlich, editor, *Cell Migration in Development and Disease*, pages 15–31. Wiley–VCH Verlag GmbH and Co. KGaA, Weinheim, 2005.
- [63] Brigitte Raynaud–Messina and Andreas Merdes.  $\gamma$ -tubulin complexes and microtubule organization. *Curr Opin Cell Biol*, 19(1):24–30, 2007.
- [64] Manfred Schliwa, Ursula Euteneuer, Ralph Gräf, and Masahiro Ueda. Centrosomes, microtubules and cell migration. In John M. Lackie, Graham A. Dunn, and Gareth E. Jones, editors, *Cell Behaviour: Control and Mechanism of Motility*. Portland Press, London, 1999.
- [65] Elias Lazarides. Intermediate filaments: A chemically heterogeneous developmentally regulated class of proteins. *Annu Rev Biochem*, 51:219–250, July 1982.
- [66] Peter M. Steinert and Dennis R. Roop. Molecular and cellular biology of intermediate filaments. *Annu Rev Biochem*, 57:593–625, July 1988.
- [67] Elaine Fuchs and Klaus Weber. Intermediate filaments: Structure, dynamics, function and disease. *Annu Rev Biochem*, 63:345–382, 1994.
- [68] Miri Yoon, Robert D. Moir, Veena Prahlad, and Robert D. Goldman. Motile properties of vimentin intermediate filament networks in living cells. *J Cell Biol*, 143(1):147–157, October 1998.
- [69] Brian T. Helfand, Lynne Chang, and Robert D. Goldman. Intermediate filaments are dynamic and motile elements of cellular architecture. *J Cell Sci*, 117:133–141, 2004.
- [70] Lynne Chang and Robert D. Goldman. Intermediate filaments mediate cytoskeletal crosstalk. *Nat Rev Mol Cell Biol*, 5(8):601–613, August 2004.

- [71] Seyun Kim and Pierre A. Coulombe. Intermediate filament scaffolds fulfill mechanical, organizational, and signaling functions in the cytoplasm. *Gene Dev*, 21(13):1581–1597, July 2007.
- [72] Lynne Chang, Kari Barlan, Ying–Hao Chou, Boris Grinand Margot Lakonishok, Anna S. Serpinskaya, Dale K. Shumaker, Harald Herrmann, Vladimir I. Gelfand, , and Robert D. Goldman. The dynamic properties of intermediate filaments during organelle transport. *J Cell Sci*, 122(16):2914–2923, August 2009.
- [73] Tim Mitchison and Marc Kirschner. Cytoskeletal dynamics and nerve growth. *Neuron*, 1(9):761–772, November 1988.
- [74] Ralph Nossal. On the elasticity of cytoskeletal networks. *Biophys J*, 53(3):349–359, March 1988.
- [75] J. J. Blum and M. C. Reed. A model for slow axonal transport and its application to neurofilamentous neuropathies. *Cell Motil Cytoskeleton*, 12(1):53–65, 1989.
- [76] Diedrik Menzel. *The Cytoskeleton of the algae*. CRC Press, 1992.
- [77] Maria J. Schilstra Peter M. Bayley and Stephen R. Martin. Microtubule dynamic instability: numerical simulation of microtubule transition properties using a lateral cap model. *J Cell Sci*, 95(1):33–48, 1990.
- [78] Leah Edelstein–Keshet. A mathematical approach to cytoskeletal assembly. *Eur Biophys J*, 27(5):521–531, August 1998.
- [79] Athan Spiros and Leah Edelstein–Keshet. Testing a model for the dynamics of actin structures with biological parameter values. *Bull Math Biol*, 60(2):275–305, March 1998.

- [80] D. Sept, H. J. Limbach, H. Bolterauer, and J. A. Tuszynski. A chemical kinetics model for microtubule oscillations. *J Theor Biol*, 197(1):77–88, March 1999.
- [81] Wolfgang Alt and Micah Dembo. Cytoplasm dynamics and cell motion: two-phase flow models. *Math Biosci*, 156(1–2):207–228, March 1999.
- [82] Eric Karsenti, François Nédélec, and Thomas Surrey. Modelling microtubule patterns. *Nat Cell Biol*, 8(11):1204–1211, November 2006.
- [83] Ju Li, George Lykotrafitis, Ming Dao, and Subra Suresh. Cytoskeletal dynamics of human erythrocyte. *Proc Natl Acad Sci*, 104(12):4937–4942, March 2007.
- [84] Robert Kirmse, Stephanie Portet, Norbert Mücke, Ueli Aebi, Harald Herrmann, and Jörg Langowski. A quantitative kinetic model for the in vitro assembly of intermediate filaments from tetrameric vimentin. *J Biol Chem*, 282(25):18563–18572, June 2007.
- [85] Vikram S. Deshpande, Robert M. McMeeking, and Anthony G. Evans. A bio-chemo-mechanical model for cell contractility. *Proc Natl Acad Sci*, 103(38):14015–14020, September 2006.
- [86] Yaozhi Luo, Xian Xu, Tanmay Lele, Sanjay Kumar, and Donald E. Ingber. A multi-modular tensegrity model of an actin stress fiber. *J Biomech*, 41(11):2379–2387, August 2008.
- [87] Esa Kuusela and Wolfgang Alt. Continuum model of cell adhesion and migration. *J Math Biol*, 58(1–2):125–161, January 2009.
- [88] Lars Wolff and Klaus Kroy. Mechanical stability: A construction principle for cells. *diffusion-fundamentals.org*, 11(56):1–14, 2009.
- [89] S. Benoit. Personal web site. <http://lamar.colostate.edu/~sbenoit/>.

## CHAPTER 4

### MODELS OF HELICAL BIOLOGICAL MOLECULES

**Remark** This chapter is based on the paper *Helical states of nonlocally interacting molecules and their linear stability: geometric approach* by S. Benoit, D. D. Holm, and V. Putkaradze, published in the Journal of Physics A: Mathematical and Theoretical, Volume 44, Number 5, February, 2011. My work on this paper focused on development of the models and simulations and deriving the energy landscape and stable conformations. The linear stability analysis and geometric analyses, included here for completeness, are due to Drs. Putkaradze and Holm.

In this chapter, the equations for strands of rigid charge configurations interacting nonlocally are formulated on the special Euclidean group,  $SE(3)$ , which naturally generates helical conformations. Helical stationary shapes are found by minimizing the energy for rigid charge configurations positioned along an infinitely long molecule with charges that are off-axis. The classical energy landscape for such a molecule is complex with many local energy minima, even when limited to helical shapes. The question of linear stability and selection of stationary shapes is studied using an  $SE(3)$  method that naturally accounts for the helical geometry. We investigate the linear stability of a general helical polymer that possesses torque-inducing non-local self-interactions and find the exact dispersion relation for the stability of the helical shapes with an arbitrary interaction potential. We explicitly determine the

linearization operators and compute the numerical stability for the particular example of a linear polymer comprising a flexible rod with a repeated configuration of two equal and opposite off-axis charges, thereby showing that even in this simple case the non-local terms can induce instability that leads to the rod assuming a helical shape.

## 4.1 Introduction

Molecules with repeating subunits that spontaneously form helical shapes are ubiquitous in nature, and are common in the context of cellular structures. A classical example is given by  $\alpha$ -helices, which are an important motif in the secondary structure of proteins [1]. Other examples of naturally occurring helical structures within cells include intermediate filament proteins keratin and vimentin [2], the myosin and kinesin families of motor proteins [2], tubulin microtubules [3], RecA and Rad51 filaments on DNA [4], and others. Artificial polymer structures that spontaneously take helical forms have also been obtained, see for example [5,6]. The spontaneous emergence and persistence of helical shapes has been the subject of several recent studies. For progress in the description of helical shapes based on elastic rod theory, see [7]. The spontaneous formation of helical structures under compaction of an elastic rod has also been shown, by using a Lennard-Jones-like potential whose repulsive core eliminates self-intersections [8].

Molecular shapes arise through an interplay between elastic forces caused by bending and twisting of the molecular bonds, and long- and short-range forces (such as electrostatic and van der Waals forces) between individual atoms comprising the molecule. For elastic interactions only, Kirchoff's rod theory [9, 10] has been used to model molecular shapes with notable success [7, 11–16]. The recent work on non-local interactions has considered helical molecules as rods with charges concentrated along the axis of the rod only [7, 10, 17, 18]. Other authors used energy optimization with

short-range repulsion only, without initial assumptions on the molecular shapes, and yet helical shapes showed surprising persistence [8,19], either for the whole molecule, or in parts of it. The crucial question is whether such helical shapes persist for more complex interactions or geometries of the molecules. For example, more accurate models of molecules could include charges that are attached at a certain distance from the axis, as shown in Fig. 4.1. Interatomic forces are caused by some potential – or combination of potentials – that depends explicitly on the geometry of the molecule and the Euclidean distance  $d$  between two points  $s$  and  $s'$  along the curve representing the axis of the molecule. Equations of motion for such molecules were derived recently using nonlocal extensions of exact geometric rod theory [20,21]. However, the question of existence of helical shapes for more complex interactions between the parts of the molecule and the methods for their computations has remained open. In this chapter, we demonstrate a fast and efficient method for finding such states, and in addition show how we can achieve a complete classification of all helical states. We also show that the geometric approach allows exact computation of dispersion relations and linear instability growth rates.

**Outline of the chapter** Section 4.2 derives the equations for nonlocally interacting rods of rigid charge configurations, called *bouquets*. These bouquets are fixed configurations of charges, rigidly attached to the molecule’s central axis. The molecule is comprised of a long repeating chain of such bouquets. The equations are formulated on the special Euclidean group,  $SE(3)$ , consisting of three-dimensional spatial rotations and translations, which naturally generate helical configurations. Section 4.3 demonstrates how to find helical stationary shapes by minimizing the energy for bouquets positioned along an infinitely long molecule with charges that are off-axis. As shown in Section 4.4, even this simple molecule, when deformed into helical configurations, shows quite a complex and intriguing energy landscape. Section 4.5 briefly

discusses how to extend the ideas presented above to include more general shapes. In particular, we consider a molecular shape we refer to as a 2-helix. Here, we define an  $n$ -helix as a molecule that is a true helix consisting of repeating groups of  $n$  bouquets along the axis. For a 2-helix, one optimizes the energy over both the shape of the helix and the relative configuration of two bouquets. One may treat  $n$ -helices by optimizing configurations of  $n$  bouquets using the same methods. After revealing the complexity of the energy landscape, even when limited to helical shapes, and the large number of energy minima in that “helical universe”, it is natural to pose the question of linear stability and selection of the stationary shapes. By using an  $SE(3)$  method that naturally accounts for the helical geometry, in Section 4.6 we investigate the linear stability of a general helical polymer that possesses torque-inducing non-local self-interactions. As far as we know, no such work has been undertaken previously. The geometric approach in Section 4.6 allows us to find the exact dispersion relation for the stability of the helical shapes with an arbitrary interaction potential. Of course, for particular applications it is important to explicitly compute the linearization operators. This is accomplished in Section 4.7 using geometric methods to compute derivatives of the potential energy. Section 4.8 computes the numerical stability for the particular example of a linear polymer comprising a charged rod with repeated configuration of two equal and opposite charges that interact through a screened electrostatic and Lennard-Jones potential. For the sake of simplicity, we concentrate on the stability of a polymer that is perfectly straight in its unstressed configuration. Such a polymer is neutrally stable in the absence of the nonlocal interactions. It is therefore interesting that nonlocal terms can induce instability that causes the molecule to deform into helical conformations. Physically, this instability is connected to the tendency of the rod to minimize its energy and properly align the dipole moments of each bouquet by twisting, as was already seen in the minimum

energy calculation shown in Section 4.4.

We note that these results are difficult to achieve in the traditional Kirchhoff based approach, as the non-local interactions depend on the relative distance and orientation of the charges at different points on the rod. In these traditional methods, the equations of motion are written in a coordinate system that is moving with the rod, and changing with both position on the rod  $s$  and time  $t$ . Thus, one has to write equations of motion, *i.e.* calculate the momenta and forces, in a frame attached to the rod that is moving and rotating in a non-inertial fashion. The main difficulty arises because the relative distance between the charges depends on both their bouquet positions on the centerline and the local rotation of the bouquet about the centerline. To find this orientation one needs to integrate auxiliary equations of motion at each step (*Darboux's* vector), so the solution must be known *before* the relative distance between the charges can be computed. However, the solution explicitly depends on the relative distance between the charges, and so the closure of the system is problematic. These complications make an explicit derivation of equations of motion from Kirchhoff's approach difficult, if not impossible. On the other hand, the approach we suggest here provides a very straightforward derivation. One need not deal with vectors, forces and torques in non-inertial frames of references, in writing conservation laws, and so forth. Instead, in the geometric approach, helices are treated in exactly the same fashion as straight lines, so stationary helical states and even their linear stability properties may be considered conveniently.

## 4.2 Derivation in $SE(3)$ coordinates

In this section, we derive the full equations of motion for a self-interacting rod in the discrete and continuous cases. This derivation is based on the exact geometric rod theory [22], that derives equations equivalent to Kirchhoff's equations for elastic

rods using symmetry-reduced variables. Since the derivation of the exact geometric rod equations for purely elastic rods is well-established, we shall concentrate on the corresponding derivation of the nonlocal equations in the language of the Lie group  $SE(3)$  – the Special Euclidean group of orthogonal rotations and translations in  $\mathbb{R}^3$ . This familiar Lie group is a semidirect product of  $SO(3)$  and  $\mathbb{R}^3$  with the following definition of group multiplication:

$$(\Lambda_1, \mathbf{r}_1) \cdot (\Lambda_2, \mathbf{r}_2) = (\Lambda_1 \Lambda_2, \Lambda_1 \mathbf{r}_2 + \mathbf{r}_1) \quad (4.1)$$

for  $\Lambda_1, \Lambda_2 \in SO(3)$  and  $\mathbf{r}_1, \mathbf{r}_2 \in \mathbb{R}^3$ . We use the notation  $\mathfrak{se}(3)$  for the corresponding Lie algebra. For the reader’s convenience, we summarize the properties of this group, its adjoint and coadjoint actions  $\text{Ad}$ ,  $\text{Ad}^*$ ,  $\text{ad}$ ,  $\text{ad}^*$  in Appendix C. More details can be found in, for example, [23].

**Definition** A *bouquet* is a rigid, non-deformable assembly of spheres, each characterized by an interaction radius (which applies to short-range interactions like Lennard-Jones), and an electrostatic charge.

A molecule, as considered in this chapter, consists of a rod that represents the molecule’s central axis, with bouquets attached at fixed base points along the rod. Each bouquet is characterized by the spatial position coordinate of its base  $\mathbf{r}(s) \in \mathbb{R}^3$  and its orientation  $\Lambda(s) \in SO(3)$ , which together define an element  $\sigma(s) = (\Lambda(s), \mathbf{r}(s)) \in SE(3) \cong SO(3) \times \mathbb{R}^3$ . We are interested in describing the effects of nonlocal interactions, which in this chapter denotes all inter-atomic forces that affect parts of the molecule not immediately adjacent to each other. These are all the forces that do not come from elastic deformation, and include, for example, electrostatic and Lennard-Jones forces.

To describe nonlocal interactions among these bouquets of charges, we define their relative orientation and position variables by the  $SE(3)$  product

$$\begin{aligned}\Xi(s, s') &= \sigma^{-1}(s)\sigma(s') = (\Lambda^{-1}(s)\Lambda(s'), \Lambda^{-1}(s)(\mathbf{r}(s') - \mathbf{r}(s))) \\ &:= (\xi(s, s'), \boldsymbol{\kappa}(s, s')), \end{aligned}\tag{4.2}$$

where  $\xi(s, s') \in SO(3)$  and  $\boldsymbol{\kappa}(s, s') \in \mathbb{R}^3$ . The position of the  $k$ -th charge in the bouquet whose base is at  $s$  along the center-line of the rod is given by

$$\mathbf{c}_k(s) = \mathbf{r}(s) + \Lambda(s)\boldsymbol{\eta}_k(s).\tag{4.3}$$

Here  $\boldsymbol{\eta}_k(s)$  denotes a vector from the base point at  $s$  on the rod to the  $k$ -th off-axis charge of the bouquet as measured in a rigid Cartesian frame with orientation  $\Lambda(s)$ . Then, the distance  $d_{km}(s, s')$  between the  $k$ -th charge at  $s$  and  $m$ -th charge at  $s'$  is given by

$$\begin{aligned}d_{km}(s, s') &= |\mathbf{c}_k(s) - \mathbf{c}_m(s')| \\ &= |\mathbf{r}(s) + \Lambda(s)\boldsymbol{\eta}_k(s) - \mathbf{r}(s') - \Lambda(s')\boldsymbol{\eta}_m(s')| \\ &= |\Lambda^{-1}(s)(\mathbf{r}(s) - \mathbf{r}(s')) + \boldsymbol{\eta}_k(s) - \Lambda^{-1}(s)\Lambda(s')\boldsymbol{\eta}_m(s')| \\ &= |\boldsymbol{\kappa}(s, s') + \boldsymbol{\eta}_k(s) - \xi(s, s')\boldsymbol{\eta}_m(s')| = d_{km}(\Xi(s, s')). \end{aligned}\tag{4.4}$$

**Remark 4.2.1.** *In finding particular helical solutions and analyzing their stability, we consider the case of polymers where all the bouquets are exactly the same, so  $\boldsymbol{\eta}_k(s)$  and  $\boldsymbol{\eta}_m(s')$  are independent of  $s$  and  $s'$ . Nonetheless, the equations of motion we derive in this section, (4.22) and (4.23), would also be valid for arbitrary dependence of the bouquet's geometry on position. However, the linear stability analysis performed later will explicitly use the fact that all bouquets are identical, and thus cannot be applied to the conformations of molecules with varying geometry.*

Consequently, the total energy of the rod due to nonlocal interactions among the charges that compose it is obtained in the continuous case as

$$E = \sum_{k,m} \int U(d_{km}(\Xi(s, s'))) ds ds',\tag{4.5}$$

for interaction potential  $U$  between individual pairs of charges. In the discrete case, the integral becomes a sum and  $s, s'$  are discrete indices, so that

$$E = \sum_{s,s',k,m} U(d_{km}(\Xi(s, s'))). \quad (4.6)$$

The corresponding contribution of nonlocal interactions to the action in Hamilton's principle for the dynamics of the rod is thus (in the discrete case)

$$S_{nl} = - \int \sum_{s,s',k,m} U(d_{km}(\Xi(s, s'))) dt. \quad (4.7)$$

In order to compute the contribution of the mutual charge interactions to the dynamics of the rod one must take the variation of this nonlocal part of the action with respect to the charge conformation  $\Xi$ . Upon denoting

$$\nu(s) = \sigma^{-1}(s)\delta\sigma(s) \in \mathfrak{se}(3), \quad (4.8)$$

where  $\mathfrak{se}(3)$  is the Lie algebra of the Lie group  $SE(3)$ , we find

$$\delta\Xi(s, s') = \delta(\sigma^{-1}(s)\sigma(s')) = -\nu(s)\Xi(s, s') + \Xi(s, s')\nu(s'). \quad (4.9)$$

We now define a pairing  $\langle \cdot, \cdot \rangle_{TSE(3)}$  between the elements of  $TSE(3)$  and  $TSE(3)^*$  – the tangent and cotangent spaces of  $SE(3)$  – as follows. If a vector  $U$  is tangent to  $SE(3)$  at point  $\sigma \in SE(3)$ , and  $W$  co-tangent to  $SE(3)$  at the same point  $\sigma$ , then  $\sigma^{-1}U$  brings the vector  $U$  to the identity element of the group, so  $\sigma^{-1}U \in \mathfrak{se}(3)$  is in the Lie algebra. Similarly,  $\sigma^{-1}W \in \mathfrak{se}(3)^*$ , so a scalar product between these elements can be taken as defined in the appendix. Thus, we define

$$\langle U, W \rangle_{TSE(3)} = \langle \sigma^{-1}U, \sigma^{-1}W \rangle_{\mathfrak{se}(3)}. \quad (4.10)$$

In what follows, we drop the subscript  $TSE(3)$  from the scalar product as not to burden the notation unnecessarily.

In order to use the minimal action principle and derive the equations of motion, we need to take the variations with respect to  $\Xi$ . The variation  $\delta\Xi$  defined in (4.9) is an element of  $TSE(3)$ , as  $\delta\Xi$  is tangent to  $SE(3)$  at the point  $\Xi$ . Then, the derivative  $\delta U/\delta\Xi$  is an element of  $TSE(3)^*$  as it is co-tangent to the group at the same point  $\Xi$ . The pairing

$$\left\langle \frac{\delta U}{\delta \Xi}, \delta \Xi \right\rangle$$

can be now defined according to (4.10).

Consequently, the variation of the nonlocal part of the action in (4.7) is given by

$$\begin{aligned} \delta S_{nl} &= - \int \sum_{s,s',k,m} \left\langle \frac{\delta U}{\delta \Xi}, \delta \Xi \right\rangle dt \\ &= - \int \sum_{s,s',k,m} \left\langle \frac{\delta U}{\delta \Xi}, -\nu(s)\Xi(s,s') + \Xi(s,s')\nu(s') \right\rangle dt \\ &= - \int \sum_{s,s',k,m} \left\langle -\frac{\delta U}{\delta \Xi}(s,s')\Xi^{-1}(s,s') + \Xi(s,s')\frac{\delta U}{\delta \Xi}(s',s), \nu(s) \right\rangle dt, \end{aligned} \quad (4.11)$$

in which the last step uses the relation  $\Xi(s',s) = \Xi^{-1}(s,s')$  obtained from the definition of  $\Xi$  in (4.2). We shall now proceed with the computation of the variations of action with respect to all dynamical quantities and thereby obtain the equations of motion.

**Velocities.** The local part of the Lagrangian in Hamilton's principle for the dynamics of the rod is written by introducing the left-invariant variables

$$\mu = \sigma^{-1}\dot{\sigma} = (\Lambda, \mathbf{r})^{-1} \left( \dot{\Lambda}, \dot{\mathbf{r}} \right) = \left( \Lambda^{-1}\dot{\Lambda}, \Lambda^{-1}\dot{\mathbf{r}} \right) \in \mathfrak{se}(3), \quad (4.12)$$

as velocities taking values in the Lie algebra  $\mathfrak{se}(3)$ .

**Elastic deformations.** In the continuous case, the invariant variables that describe elastic deformations are,

$$\lambda = \sigma^{-1}\sigma' \in \mathfrak{se}(3). \quad (4.13)$$

In the discrete case, following the Moser-Veselov method for numerical discretization of rigid body dynamics [24] we set,

$$\lambda = \sigma^{-1}(s)\sigma(s+1) \in SE(3), \quad (4.14)$$

where  $s = 1, 2, \dots$  is the discrete index labeling a given base. The elastic part of the Lagrangian will then depend on  $\lambda$ .

**Compatibility conditions.** The *compatibility conditions* are obtained, in the continuous case, by using equality of cross derivatives, so that  $\sigma_{st} = \sigma_{ts}$ . Differentiating (4.12) with respect to  $s$  and (4.13) with respect to  $t$ , then subtracting yields

$$\frac{\partial \mu}{\partial s} - \frac{\partial \lambda}{\partial t} = -\lambda \mu + \mu \lambda := [\mu, \lambda]_{\mathfrak{se}(3)} = \text{ad}_\mu \lambda, \quad (4.15)$$

where  $[\mu, \lambda]_{\mathfrak{se}(3)}$  is the commutator of  $\mu$  and  $\lambda$  in  $\mathfrak{se}(3)$ . In the discrete case, we write (4.14) as  $\sigma(s+1, t) = \sigma(s, t)\lambda(s, t)$ . Differentiating this condition with respect to time, we get

$$\frac{\partial \lambda}{\partial t}(s) = \lambda(s)\mu(s+1) - \mu(s)\lambda(s), \quad (4.16)$$

or in terms of  $\mathfrak{se}(3)$ -algebra quantities only

$$\lambda^{-1} \frac{\partial \lambda}{\partial t}(s) = \mu(s+1) - \text{Ad}_{\lambda^{-1}} \mu(s). \quad (4.17)$$

**Dynamical equations: variations** In the continuous case, the variations of the velocities on the Lie algebra  $\mathfrak{se}(3)$  satisfy,

$$\delta \mu = -\nu \mu + \mu \nu + \frac{\partial \nu}{\partial t}. \quad (4.18)$$

In the discrete case, this is replaced by a variation on the Lie group  $SE(3)$ ,

$$\lambda^{-1} \delta \lambda(s) = -\text{Ad}_{\lambda^{-1}} \nu(s) + \nu(s+1). \quad (4.19)$$

For the discrete case, one may then compute the variation of the Lagrangian as,

$$\begin{aligned}
& \sum_s \left\langle \lambda^{-1}(s) \frac{\delta l}{\delta \lambda}(s), \lambda^{-1}(s) \delta \lambda(s) \right\rangle \\
&= \sum_s \left\langle \lambda^{-1}(s) \frac{\delta l}{\delta \lambda}(s), -\text{Ad}_{\lambda^{-1}(s)} \nu(s) + \nu(s+1) \right\rangle \\
&= \sum_s \left\langle -\text{Ad}_{\lambda^{-1}(s)}^* \left( \lambda^{-1}(s) \frac{\delta l}{\delta \lambda}(s) \right) + \lambda^{-1}(s-1) \frac{\delta l}{\delta \lambda}(s-1), \nu(s) \right\rangle.
\end{aligned} \tag{4.20}$$

In continuous time, the Euler-Poincaré equations emerge from the following direct computation as in [20, 21],

$$\begin{aligned}
& \int \int \left\langle \frac{\delta l}{\delta \mu}, \delta \mu \right\rangle dt ds = \int \int \left\langle \frac{\delta l}{\delta \mu}, -\nu \mu + \mu \nu + \frac{\partial \nu}{\partial t} \right\rangle dt ds \\
&= \int \int \left\langle \frac{\delta l}{\delta \mu}, \text{ad}_\mu \nu + \frac{\partial \nu}{\partial t} \right\rangle dt ds \\
&= \int \int \left\langle \left( -\frac{\partial}{\partial t} + \text{ad}_\mu^* \right) \frac{\delta l}{\delta \mu}, \nu \right\rangle dt ds.
\end{aligned} \tag{4.21}$$

Likewise, the equations of motion in continuous time for the spatially discrete nonlocal rod, may be written in  $SE(3)$  coordinates as

$$\begin{aligned}
& \left( -\frac{\partial}{\partial t} + \text{ad}_\mu^* \right) \frac{\delta l}{\delta \mu} - \text{Ad}_{\lambda^{-1}(s)} \left( \lambda^{-1}(s) \frac{\delta l}{\delta \lambda}(s) \right) + \lambda(s-1) \frac{\delta l}{\delta \lambda}(s-1) \\
& \quad - \sum_{s', m, k} -\frac{\delta U}{\delta \Xi}(s, s') \Xi^{-1}(s, s') + \Xi(s, s') \frac{\delta U}{\delta \Xi}(s', s) = 0.
\end{aligned} \tag{4.22}$$

In the continuous case, a similar calculation gives (note that now  $\lambda = \sigma^{-1} \sigma' \in \mathfrak{se}(3)$ ):

$$\begin{aligned}
& \left( -\frac{\partial}{\partial t} + \text{ad}_\mu^* \right) \frac{\delta l}{\delta \mu} + \left( -\frac{\partial}{\partial s} + \text{ad}_\lambda^* \right) \frac{\delta l}{\delta \lambda} \\
& \quad - \sum_{m, k} \int -\frac{\delta U}{\delta \Xi}(s, s') \Xi^{-1}(s, s') + \Xi(s, s') \frac{\delta U}{\delta \Xi}(s', s) ds' = 0.
\end{aligned} \tag{4.23}$$

**Remark** Notice that (4.23) are exactly the equations derived earlier in [20, 21]. However, the discrete equations (4.22) for nonlocally interacting molecules are new, as far as we know.

**Lemma 4.2.2.** *For an arbitrary potential  $U(d)$ , equations (4.22) and (4.23) reduce to algebraic equations for helical solutions. The solutions of these algebraic equations are stationary helical shapes.*

**Proof** Helical configurations in the discrete case are obtained from taking a given element  $a \in SE(3)$  and defining  $\sigma(s) = a^s$ . In the continuous case, a given element  $\lambda \in \mathfrak{se}(3)$  generates  $\sigma(s)$  from the differential equation  $\sigma'(s) = \sigma(s)\lambda_0$  (exponential map). In either case,

$$\Xi(s, s') = \sigma^{-1}(s)\sigma(s') = \sigma(s' - s). \quad (4.24)$$

Then,

$$d_{km}(s, s') = d_{km}(\Xi(s, s')) = d_{km}(\sigma(s' - s)),$$

and therefore

$$\frac{\delta U}{\delta \Xi}(s, s') := D_1(s' - s),$$

where  $D_1$  is some  $TSE(3)^*$ -valued function that depends only on the difference between  $s$  and  $s'$ . Thus, the right-hand sides under the sum (4.22) and in the integral in (4.23) depend only on the difference between  $s$  and  $s'$ , and are therefore *constant*. Likewise, the left-hand sides of these equations are also constant, as  $\mu = 0$  and  $\lambda = a \in SE(3)$  in the discrete case and  $\lambda = \sigma_0 \in \mathfrak{se}(3)$  in the continuous case. Thus, integro-differential equations (4.22) and (4.23) reduce to algebraic equations for helical solutions, as long as the potential between two charges depends (in an arbitrary fashion) only on the Euclidean distance between those charges.  $\square$

Of course, this result had been well-known by molecular biologists for at least 50 years; in their famous paper [25] Pauling, Corey and Branson noted that “... *It is likely that these [helical] configurations constitute an important part of the structure of both fibrous and globular proteins, as well as synthetic polypeptides*”. As it turned out, the helical structures are amazingly robust; they appear for large variety of molecules with widely ranging elastic properties and charge distributions. Lemma 4.2.2 provides a mathematical model for this well-established empirical fact. It is worth noting however that the molecules that are locally helical almost never stay

in the shape of a perfect straight helix if they are sufficiently long. This *folding* of molecules is driven by a combination of the elastic and non-local forces and plays a very important role in the ensuing functionality of molecules. The instabilities of the helical states will be considered later using geometric approach.

**Remark 4.2.3.** *Lemma 4.2.2 includes, as a particular case, results from previous work on the helical solutions of the Kirchhoff's rod (no nonlocal terms) or uniformly charged Kirchhoff rod [18], with the charges<sup>10</sup> positioned at the rod's axis. In that case, the rigid charge conformations are positioned at  $\boldsymbol{\eta}(s) = 0$ , and thus*

$$d(s, s') = |\boldsymbol{\kappa}(s' - s)|.$$

*In this case, the distance  $d$  is independent of the mutual orientation  $\xi(s, s')$ , which is the first part of  $SE(3)$  group element  $\sigma^{-1}(s)\sigma(s') := (\xi(s, s'), \boldsymbol{\kappa}(s, s'))$ . That is, charges arranged on the axis produce no torque.*

*With this particular simplification, the computation still proceeds in the same way as before and reduction to algebraic equations still holds. Of course, more work is needed for each particular potential to demonstrate that the algebraic equations actually have a solution, especially if complicated elasticity laws in the rod are assumed. Thus, Lemma 4.2.2 provides a simple justification for helical solutions that have been ubiquitous in the previous literature. However, our result goes further: helical shapes also allow one to search for helical solutions as solutions of algebraic equations for arbitrary charges off axis and for a charge distribution at each point of the molecule, possibly generating torque in the molecule.*

---

<sup>10</sup> Here, we use the word “charge” somewhat loosely to denote arbitrary potential interaction, like Morse or Lennard-Jones, and not just electrostatic potential.

### 4.3 Application to a linear rod with straight un-stressed conformation

This section demonstrates how to find helical stationary shapes for charge bouquets positioned along an infinitely long, naturally straight molecule.

To illustrate the general ideas described above, we shall consider a molecule that consists of a chain of centerline atoms connected with elastic springs, and charges that are attached to each unit of the elastic chain with a rigid charge bouquet. In the undisturbed (base) configuration, the molecule is straight. In what follows, we select a charge bouquet containing two charges of  $q_i = \pm 0.3e$ , where  $e$  is the charge of electron. This arrangement approximates any molecule which has a constant dipole moment perpendicular to the axis, for example, vinylidene fluoride oligomers (VDF) [26]. More general charge configurations such as quadrupoles *etc.* can be incorporated by considering more general bouquets.

We assume electrical charges exhibit a screened electrostatic interaction

$$E_{ij,C}(s, s') = \frac{q_i(s) q_j(s')}{4\pi\epsilon_0 d_{ij}(s, s')} e^{-d_{ij}(s, s')/\lambda}, \quad (4.25)$$

where  $d_{ij}$  is the distance between charges  $q_i$  at  $s$  and  $q_j$  at  $s'$ , and  $\lambda$  denotes the Debye screening length. In what follows, we consider values of  $\lambda$  corresponding to various ionic strengths in the solution, from  $I = 0.001$  M/l (close to de-ionized water) to  $I = 10$  M/l (an order of magnitude higher than sea water). Debye length  $\lambda$  and ionic strength  $I$  are related by

$$\lambda = \sqrt{\frac{\epsilon_0 \epsilon_r k_B T}{2 N_A e^2 I}}, \quad (4.26)$$

where  $\epsilon_0$  is the permittivity of space,  $\epsilon_r$  is dielectric constant of the media,  $k_B$  is Boltzmann's constant and  $N_A$  is Avogadro's number.

We seek stationary states that are invariant with respect to an affine (helical) transformation of space, which rotates a coordinate frame  $F$  by a matrix  $\Lambda$ , and

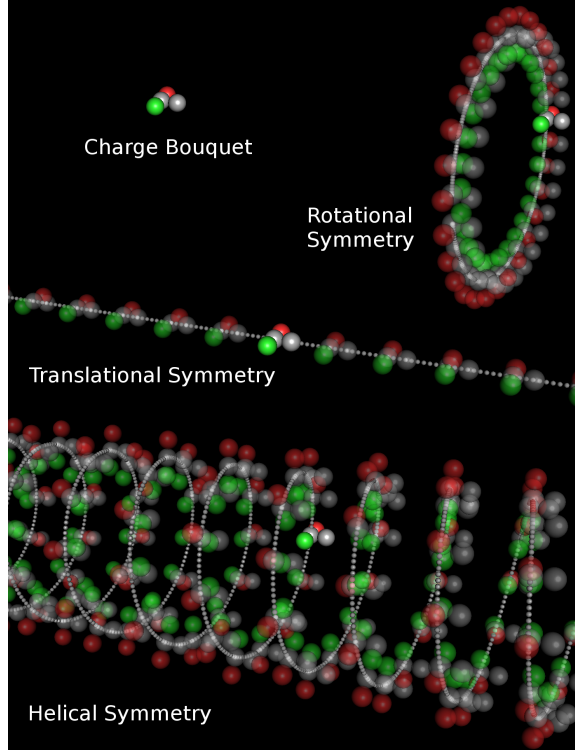


Figure 4.1: Top left: an example of a charge bouquet with four atoms. The electrically charged atoms are shown in red and green (positive or negative). Grey atoms are neutral, but still interact with other atoms through Lennard-Jones potential (4.34). The molecules we consider are long chains of these bouquets. Top right: a circular conformation obtained by applying rotational symmetry to the bouquet. Middle: A linear conformation obtained by applying the translational symmetry to the bouquet that are considered to be undisturbed configuration of the molecule. Bottom: A helical conformation obtained by simultaneous application of rotation and translation to the bouquet.

performs a translation of an arbitrary vector  $\mathbf{r}$  as

$$(F, \mathbf{r}) \rightarrow (\Lambda F, \Lambda \mathbf{r} + \mathbf{a}) . \quad (4.27)$$

In particular, we seek solutions with bouquets spaced uniformly on a helix of radius  $R$  and pitch  $C$ , with the rotation being parallel to the  $(x, y)$  plane. By *pitch*, we mean that after making one period of rotation, the atoms are moved by the distance

$C$  along the  $z$ -axis. The helix is then defined parametrically by

$$x = R \cos t, \quad y = R \sin t, \quad z = Ct, \quad (4.28)$$

or explicitly

$$x = R \cos z/C, \quad y = R \sin z/C, \quad (4.29)$$

where  $R \geq 0$  and  $C \neq 0$ . The helix is right-handed for  $C > 0$  and left-handed for  $C < 0$ . We use  $R$  and  $C$  as parameters in our calculations and visualizations. A continuous helix is a curve that is invariant under a set of transformations consisting of a rotation  $\Lambda$  about the  $\hat{\mathbf{z}}$  axis and a translation  $\mathbf{a}$ , parameterized by  $z$ ,

$$\Lambda(z) = \begin{bmatrix} \cos\left(\frac{z}{C}\right) & \sin\left(\frac{z}{C}\right) & 0 \\ -\sin\left(\frac{z}{C}\right) & \cos\left(\frac{z}{C}\right) & 0 \\ 0 & 0 & 1 \end{bmatrix}, \quad \mathbf{a}(z) = \begin{bmatrix} R \sin\left(\frac{z}{C}\right) \\ R \cos\left(\frac{z}{C}\right) \\ z \end{bmatrix}. \quad (4.30)$$

For a discrete helix, we consider values of  $t$ , (respectively,  $z$ ) that are discrete multiples of some value  $T$  (respectively,  $z/C$ ):

$$t = nT \quad \text{resp.} \quad z = n\frac{z}{C}, \quad \text{where} \quad n \in \mathbb{Z}. \quad (4.31)$$

Bouquets on the helix are oriented such that the helical invariance described above is maintained. Once a single bouquet is specified, at say  $z = 0$ , (4.30) generates the entire helix structure. Let  $A \in SO(3)$  denote the orientation of the initial bouquet at  $z = 0$ . In what follows, we limit  $A$  to a twist about the tangent to the helix at  $z = 0$ , as shown in Fig. 4.2, allowing a single angle  $\alpha$  to characterize bouquet orientation.

$$A(R, C, \alpha) = \begin{bmatrix} \cos \alpha & \frac{-C}{\sqrt{4\pi^2 R^2 + C^2}} \sin \alpha & \frac{2\pi R}{\sqrt{4\pi^2 R^2 + C^2}} \sin \alpha \\ \frac{C}{\sqrt{4\pi^2 R^2 + C^2}} \sin \alpha & \frac{4\pi^2 R^2 + C^2 \cos \alpha}{4\pi^2 R^2 + C^2} & \frac{2\pi RC}{4\pi^2 R^2 + C^2} (1 - \cos \alpha) \\ \frac{-2\pi R}{\sqrt{4\pi^2 R^2 + C^2}} \sin \alpha & \frac{2\pi RC}{4\pi^2 R^2 + C^2} (1 - \cos \alpha) & \frac{4\pi^2 R^2 \cos \alpha + C^2}{4\pi^2 R^2 + C^2} \end{bmatrix}. \quad (4.32)$$

The entire helical structure may then be generated by repeated application of (4.30).

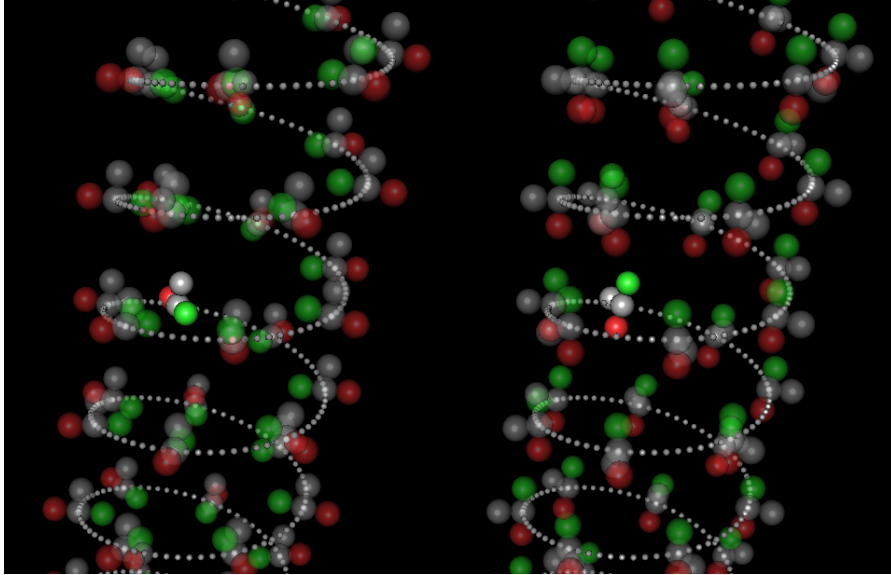


Figure 4.2: Effect of twist transformation - the twisted bouquet is highlighted.

## 4.4 Energy of a helical conformation

This section explains the interaction energies of a realistic molecule to be used in calculations, both the local (elastic) parts and non-local (electrostatic and Lennard-Jones). As discussed above, we investigate the particular example of a molecule of bouquets with two opposite charges  $\pm q$  positioned on either side of the polymer axis, each a distance  $l$  from that axis. This simplified model describes a polymer with a constant polarization perpendicular to the polymer's axis. The interaction energies are defined as follows.

**Elastic energy.** We consider elastic energy as quadratic in bond bend angle,

$$E_{elastic} = \frac{1}{2}\mu(\Delta\phi)^2, \quad (4.33)$$

where  $\mu$  is a spring constant, and  $\Delta\phi$  is the bond bend angle with respect to its unstressed orientation *in the intrinsic frame*, assumed straight. For naturally helical molecules,  $\Delta\phi$  would be the value of rotation angle for a bouquet about its rotation

axis in the intrinsic frame from its equilibrium value. In terms of global geometry that would mean that bend energy is punishing creation of local curvature. A value of  $\mu = 3.025 \cdot 10^5 J/(rad^2)Mol = 5.022 \cdot 10^{-19} J/rad^2$  is typical for bend rigidity for a carbon-carbon bond. The bend depends (through a complex algebraic formula that we do not present here) on the radius and pitch (axial distance traversed on each rotation) of the helix.

**Lennard-Jones energy.** To prevent self-intersection, we introduce a truncated Lennard-Jones interaction between charge bouquet nodes with equilibrium distance  $d_0$  and potential well depth  $\varepsilon$ . When the centers of two bouquet nodes are a distance  $d$  from each other, they experience a potential given by

$$E_{LJ} = \begin{cases} \varepsilon \left[ \left(\frac{d_0}{d}\right)^{12} - 2 \left(\frac{d_0}{d}\right)^6 - \frac{1}{3^{12}} + \frac{2}{3^6} \right] & d < 3 d_0 \\ 0 & d \geq 3 d_0 \end{cases} . \quad (4.34)$$

**Charge potential energy.** As mentioned when the model was introduced, each bouquet has charges of  $q_{1,2}(s) = \pm 0.3e$  that interact with each other through the screened Coulomb potential (4.25) with Debye length  $\lambda$ .

**Total energy of a given conformation.** Given a bouquet configuration and values for  $R$ ,  $C$ , and  $\alpha$ , we compute the total energy by choosing a reference bouquet, then working outward along the helix in both directions by helical symmetry. For each bouquet we reach, its contribution is the sum of the Lennard-Jones and Coulomb interactions of the bouquet nodes with the reference bouquet nodes. The sum of these, plus the elastic energy corresponding to the given  $R$  and  $C$  give the energy per bouquet (energy density) of the given conformation.

As an example, we demonstrate the particular energy landscape for  $I = 0.001M/l$  in Fig. 4.3. The vertical axis is helix radius  $R$ , the horizontal axis is helix pitch  $C$ , with  $(R, C) = (0, 0)$  in the upper left corner. The energy scale bar is shown on the

right, with lowest energies in black, highest in white. The left edge and the upper left-hand corner contain most of the energy minima. The minima along the left-hand edge, corresponding to small pitch  $C$  (on the order of the size of the bouquet), corresponds to the helices solutions that are being “ratcheted” into tighter and tighter conformations as we proceed upward (smaller  $R$ ). The values of the energy in this graph are minima over all twists (values of  $\alpha$ ) of the bouquet, as shown in Fig. 4.1. The local minima of this energy landscape are stable helical conformations.

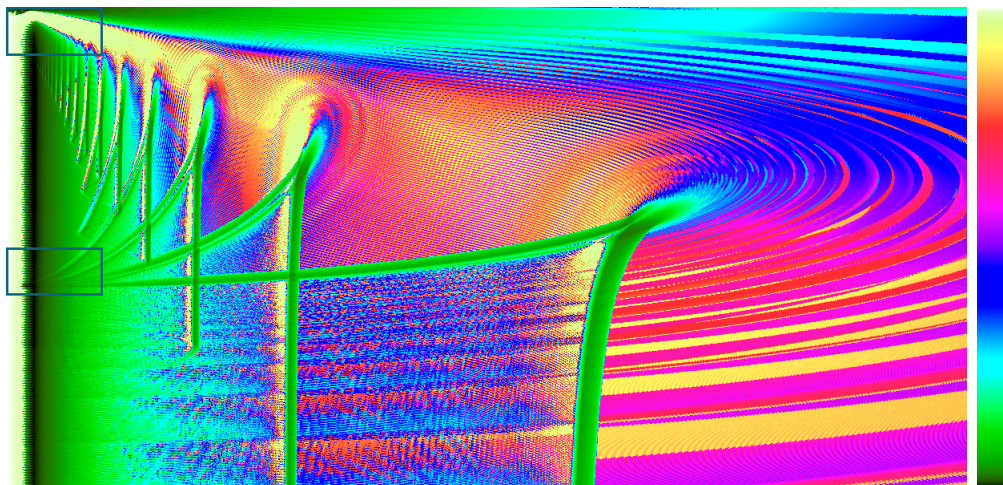


Figure 4.3: The energy landscape for a given ionic strength  $I = 0.001M/l$ . The vertical coordinate is radius  $R$  and the horizontal coordinate is pitch  $C$ . Energy is also dependent on the rotation of the bouquet around the axis  $\alpha$ , but this coordinate has been projected out onto two dimensions by taking a minimum over all rotation angles for the bouquet. That projection preserves the minima of the energy. Notice that this energy plot provides a complete analysis for all helical conformations. Helical conformations that are potential minima are concentrated on the left-hand side (small pitch, increasing radius) and upper left-hand corner (small radius, increasing pitch. Below, Figure 4.4 shows blow-ups of the framed rectangular regions.

In order to further elucidate the structure of the energy landscape, Fig. 4.4 presents a blow-up of the two boxes in Fig. 4.3. Yellow dots correspond to energy minima and thus show stationary conformations. Since we assume that the base conformation of our molecule is linear, a weakly ionized solution leads to longer electrostatic interac-

tion, resulting in richer structure. Helical conformations become increasingly unlikely for strongly ionized solutions that make long-range electrostatic forces weaker. For strongly ionized solutions, elastic forces tend to unwind the helices into straight lines.

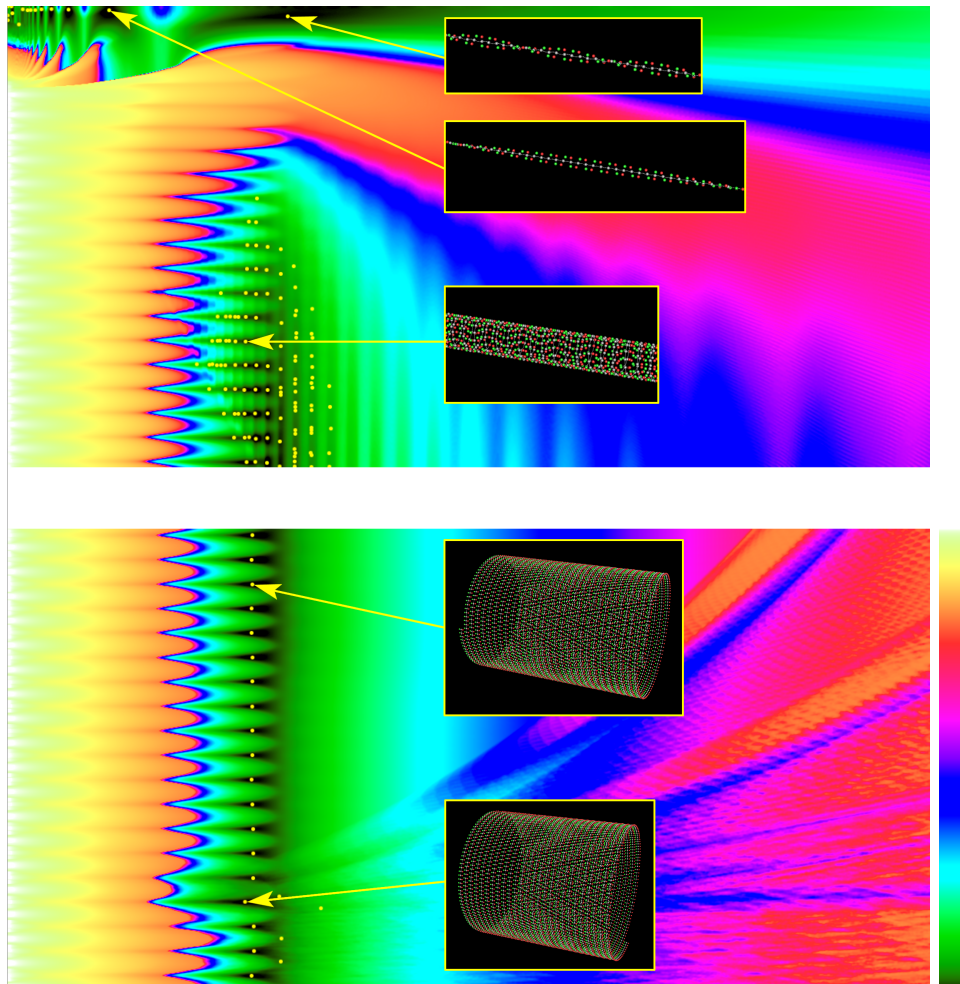


Figure 4.4: Blow-up of energy landscape for the boxes in Fig. 4.3. The energy scale has been adjusted to show more detail, and is shown on the right with lowest energies in black, highest energies in white. The vertical coordinate is radius  $R$  and horizontal coordinate is pitch  $C$ . Top: upper left corner box in Fig. 4.3. Bottom: box in the middle of left edge in Fig. 4.3. Several examples of the helical conformations corresponding to different energy minima are presented as inserts with yellow arrows indicating the corresponding energy minima.

As shown in Fig. 4.4, even this simple molecule, when deformed into helical config-

urations, shows quite a complex and intriguing energy landscape. While the details of the landscape depend on the individual molecular parameters, the presence of “ratcheting” helical states is, we believe, typical for all molecules of this type. In this figure, several examples of the helical conformations corresponding to different energy minima are presented as inserts. There are two types of helical conformations. The “twist” type is obtained by twisting a base straight conformation, and is characterized by small radius  $R$  and increasing pitch  $C$ . In a given energy landscape, there are only finitely many conformations of this type, as increasing the twist beyond certain level will cause elastic forces that are too large to be balanced by electrostatic attraction. We show two examples of such twist conformations in the top part of this figure. Another type of helical solution is given by the ratcheting states, characterized by a pitch on the order of bouquet’s size and increasing radius. This is shown both in the top and bottom parts of the figure. There are infinitely many of these ratcheting states, as the radius can increase (in principle) to arbitrarily large values. Energy minima then occur every time the opposite charges line up on sequential rolls of the helix. That explains the regularity of occurrence of those minima. They occur every time the helix circumference increases by the distance separating the bouquets,  $l$ . This leads to an increase of radius between neighboring ratcheting conformations as  $\Delta R = l/(2\pi)$ .

To illustrate how varying ionic strength of the solution changes the energy landscape of helical conformations, we compute 10 energy landscapes varying from  $I = 0.001M/l$  to  $I = 0.16M/l$ . These energy landscapes are presented, with the same orientation and axes as in Fig. 4.5 (where the ionic strengths are labeled in  $M/ml$ ). From this, it is clear that the variation of ionic strength and hence Debye length, has a profound effect on the energy landscape. As we see below, the ionic strength is also of particular importance for linear stability.

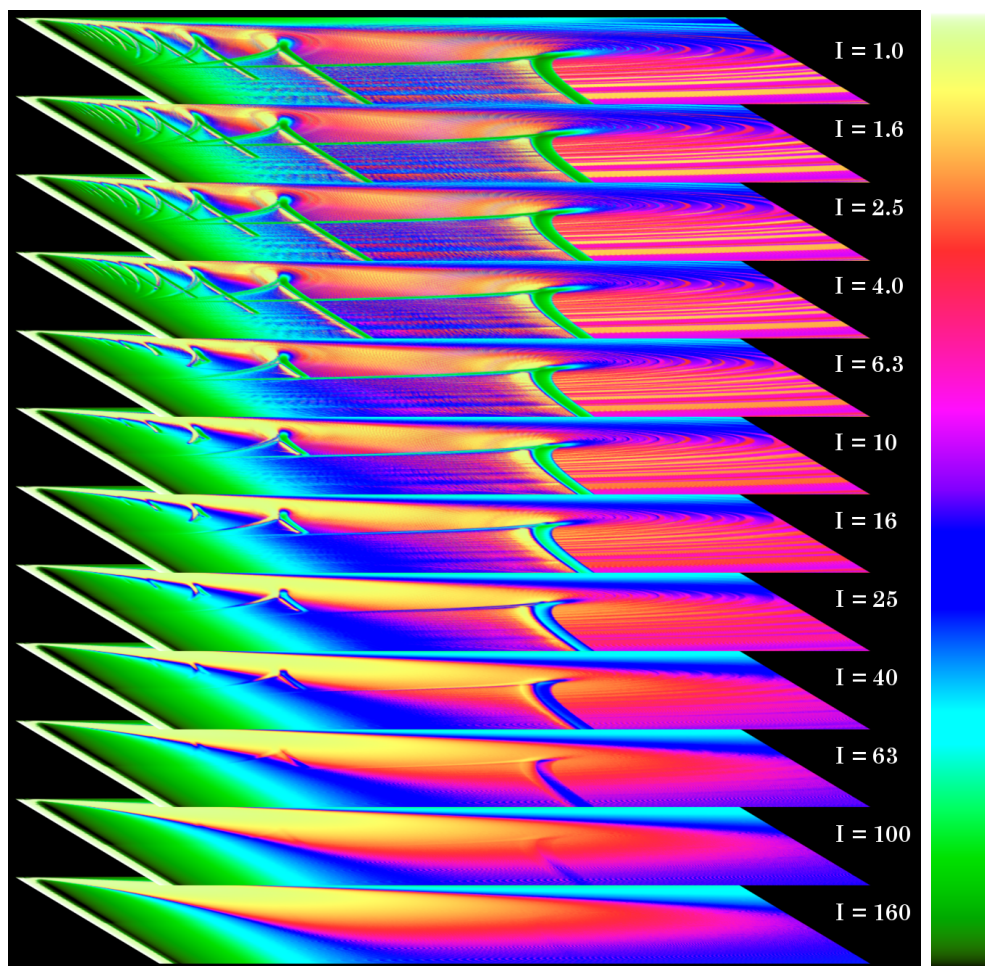


Figure 4.5: (Supplementary Figure) Energy landscapes for different values of ionic strengths  $I$ , expressed in Moles/l. A value  $I = 0.001M/l$  is a very weakly ionized solution, whereas  $I = 0.16M/l$  is a rather strongly ionized solution.

## 4.5 Multiple helical conformations

In this section, we explore generalizations of the helical shapes considered above. We show how to compute a particular molecular shape that we refer to as a *2-helix* (and, in general, *n-helix*). By 2-helix we mean a conformation where a group consisting of two bouquets with some relative position and orientation is repeated along a helix. Alternatively, a 2-helix can be seen as two helices of single bouquets arranged so

the polymer axis passes through bouquets from alternating helices over its length. The relative orientation of bouquets in the group can be arbitrary. Such structures have been suggested and analyzed in [27] in the context of describing given molecular configurations:  $\beta$ -helix structure (2-helix) or collagen (3-helix). These structures may be obtained as natural energy minima for a given molecule. In particular, we present an example of an equilibrium configuration of a 2-helix using the bouquet considered in the previous section. An extension of these ideas is possible for  $n$ -helices with  $n > 2$ . In general,  $n$ -helices are combinations of  $n$  helical conformations, with 2, 3,  $\dots$ ,  $n$  being obtained from the first one by a shift, rotation and a twist of the base bouquet. A detailed map of the energy landscape for an  $n$ -helix is problematic even for moderate  $n$ , because the number of parameters involved in defining the conformation of such a shape may increase prohibitively with  $n$ , as the position and orientation of each bouquet is required in defining a repeated group in an  $n$ -helix.

For a 2-helix, we optimize the energy over both the shape of the helix and the relative configuration of two bouquets. A minimal energy over these variables will, by the helical symmetry, provide an exact stationary conformation for the whole molecule. Two examples of such conformations are given in Fig. 4.6. Details of calculations of more general multi-helices will be discussed elsewhere.

## 4.6 Linear stability analysis

This section derives the dispersion relations for the linear stability of helical polymers, based on the linearizations of (4.22) and (4.23) about a helical state that is assumed to be a stationary solution. As we show in this section, the use of geometric methods yields an exact dispersion relation.

The energy landscape for charged polymers with nonlocal interactions is complex, even when limited to helical shapes, because of the large number of energy minima

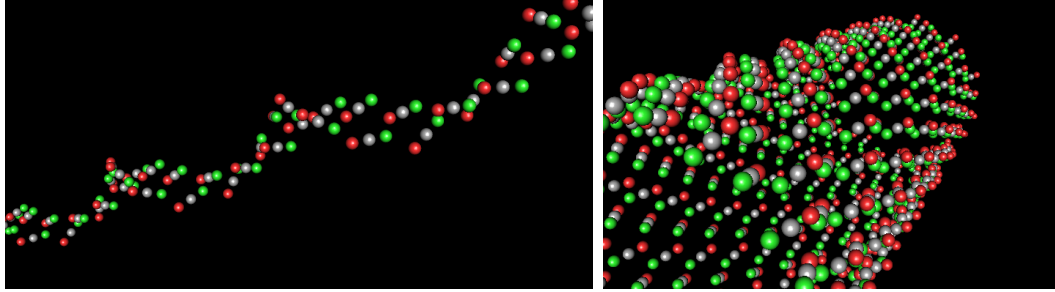


Figure 4.6: 2-helix conformations for the ionic strength  $I= 0.001$  M/l, and red/green charges in each bouquet of  $\pm 0.8e$ . The elastic centerline (not shown) goes through gray spheres that are the centers of the bouquets. The conformation is not a perfect helix, but instead consists of two helices, in which the second helix has undergone a twist, shift and rotation with respect to the first one. The distance between the bases of the bouquets (gray spheres) is  $2 \text{ \AA}$ .

in that “helical universe”. It is natural to pose the question of linear stability and selection of the stationary shapes. Here, the geometric approach allows us to find the exact dispersion relation for the stability of the helical shapes. As far as we know, no such work has been undertaken before, perhaps because of the complexity of the linear stability analysis when using traditional methods.

By using an  $SE(3)$  method that naturally accounts for the helical geometry, one may investigate the linear stability of a general helical polymer with torque-inducing non-local self-interactions. Studies of the stability of helical elastic rods have been undertaken before, with most studies concentrating on the linearization of the traditional Kirchhoff equations about the stationary helical states [11, 28–32]. The focus of these works was on the stability analysis based on increasingly complex elastic properties of the rod. Alternatively, the work [33] investigated the stability of elastic rods using the exact geometric rod theory and applied it to DNA dynamics. All these works have used the continuous model of elastic rods. Our results differ in two ways from previous studies. First, our results are formulated for spatially discrete rods, as discussed in the previous sections. Second, and more importantly, our stability

analysis includes non-local interaction of charges that in general occupy positions *off the axis* of the elastic rod. The forces on these charges generate torques acting on the rod's centerline. These torques are absent when one considers purely elastic rods, or when the charges are distributed only along the centerline.

This section shows that the presence of the torques due to non-local interaction of off-axis charges generates an *instability* of the rod and that the instability appears even for the simplest possible states – the linear rod. The instability due to nonlocal torques is new, as far as we are aware.

Obtaining similar results using Kirchhoff's rod equations would be problematic. The main difficulty consists in finding the Euclidean distance between two arbitrary points on a rod's axis using coordinates intrinsic to the rod. In addition, the present computation shows the geometric origin of the exact dispersion relation for arbitrary helical configuration of a rod (without charges), something that was noticed already in [11]. In our opinion, the present method based on exact geometric theory is more straightforward, algorithmic and compact than the corresponding linear analysis of Kirchhoff equations.

Suppose we have a helical configuration arising from successive repetition of a given element  $a \in SE(3)$ , so that  $\sigma(s) = a^s$  and  $\Xi(s, s') = a^{s'-s}$ . Let us linearize about this solution, so

$$\sigma(s) = a^s + \epsilon a^s \psi_1(s, t) + O(\epsilon^2). \quad (4.35)$$

The linearization written symbolically as  $\sigma = \sigma_0 + \epsilon \sigma_1$  is defined by

$$\psi_1 = \sigma_0^{-s} \sigma_1(s) := a^{-s} \sigma_1(s) \in \mathfrak{se}(3). \quad (4.36)$$

As it turns out, this substitution leads to an exact dispersion relation for  $\sigma_1$ . We define the  $O(\epsilon)$  perturbations in velocity and deformation as follows. First, perturbations

of the velocity are determined, as

$$\mu(s, t) = \epsilon\mu_1(s, t) + O(\epsilon^2), \quad \mu_1 = \sigma_0^{-1}\dot{\sigma}_1 = \dot{\psi}_1 \in \mathfrak{se}(3). \quad (4.37)$$

In the discrete case,

$$\lambda(s, t) = a + \epsilon\lambda_1 + O(\epsilon^2), \quad (4.38)$$

where

$$\lambda_1 = -\sigma_0^{-1}(s)\sigma_1(s)a + \sigma_0^{-1}(s)\sigma_1(s+1) = -\psi_1(s)a + \psi_1(s+1) \in \mathfrak{se}(3). \quad (4.39)$$

In the corresponding continuous case, one denotes  $\lambda_0 = \sigma^{-1}(s)\sigma'(s) = \Gamma$  and finds,

$$\begin{aligned} \lambda(s, t) &= \Gamma + \epsilon\lambda_1 + O(\epsilon^2) \\ \lambda_1 &= -\sigma_0^{-1}\sigma_1\Gamma + \sigma_0^{-1}\sigma_1'(s) = -\psi_1\Gamma + \psi_1' \in \mathfrak{se}(3). \end{aligned} \quad (4.40)$$

For simplicity (in order to keep the formulas compact), we shall assume for the discrete case that

$$\frac{\delta l}{\delta \mu} = \Pi_0 + \epsilon I\mu_1 + \dots, \quad \lambda^{-1}\frac{\delta l}{\delta \lambda} = K_0 + \epsilon K_1(s) + \dots \quad (4.41)$$

Next, we compute the linearization of the nonlinear terms due to elasticity. In order to find the linearization of the sum of terms

$$\text{Ad}_{\lambda^{-1}(s)}^* \left( \lambda^{-1}(s) \frac{\delta l}{\delta \lambda}(s) \right) + \lambda^{-1}(s-1) \frac{\delta l}{\delta \lambda}(s-1), \quad (4.42)$$

in equation (4.22) we utilize the following proposition.

**Proposition 4.6.1.** *Suppose  $G$  is a Lie group with Lie algebra  $\mathfrak{g}$  and  $\langle \cdot, \cdot \rangle : \mathfrak{g}^* \times \mathfrak{g} \rightarrow \mathbb{R}$  is a pairing between the Lie algebra and its dual. Suppose  $A(\epsilon) \in G$  is a curve in  $G$  with  $A(0) = A_0$  and  $A_0^{-1}A'(0) = a \in \mathfrak{g}$ ,  $\alpha(\epsilon) \in \mathfrak{g}^*$ , and  $\alpha'(0) = \xi$ . Then (see, for example, [23], p.60)*

$$\left. \frac{\partial}{\partial \epsilon} \text{Ad}_{A^{-1}(\epsilon)}^* \alpha(\epsilon) \right|_{\epsilon=0} = \text{Ad}_{A_0^{-1}}^* (\xi - \text{ad}_a^* \alpha_0). \quad (4.43)$$

Note that  $\lambda^{-1}\delta l/\delta\lambda$  has the physical meaning of the local stress in the body coordinate frame at point  $s$ .

Then, writing

$$\lambda^{-1}\frac{\delta l}{\delta\lambda}(s) = K_0 + \epsilon K_1(s) + O(\epsilon^2),$$

where  $K_0, K_1 \in \mathfrak{se}(3)^*$ . Hence, the linearization of (4.42) is computed as follows

$$\begin{aligned} \frac{\partial}{\partial\epsilon}\Bigg|_{\epsilon=0} & \left( -\text{Ad}_{\lambda^{-1}(s)}^* \left( \lambda^{-1}(s) \frac{\delta l}{\delta\lambda}(s) \right) + \lambda^{-1}(s-1) \frac{\delta l}{\delta\lambda}(s-1) \right) \\ & = -\text{Ad}_{\lambda_0^{-1}}^* \left( K_0 - \text{ad}_{\psi_1}^* K_1(s) \right)(s) + K_1(s-1), \end{aligned} \quad (4.44)$$

where  $\psi_1(s) := \lambda_0^{-1}(s)\lambda_1(s) \in \mathfrak{se}(3)$ .

The linearization of the nonlocal terms in equation (4.22) is less straightforward and will be outlined in its own section below. For now, we assume it is possible to compute that linearization, and it is described by some linear operator  $\mathbb{L}(\Xi(s, s'))\psi_1(s)$ , which is defined as follows. Consider an arbitrary  $\eta \in \mathfrak{se}(3)$  and define the *scalar* function of  $s$  by the following pairing,

$$I(s) = \int \left\langle -\frac{\delta U}{\delta\Xi}(s, s')\Xi(s, s') + \Xi^{-1}(s, s')\frac{\delta U}{\delta\Xi}(s', s), \eta \right\rangle ds'. \quad (4.45)$$

The nonlocal term takes values in the space  $\mathfrak{se}(3)^*$ , so the pairing in (4.45) indeed defines a scalar function. We need to find its linearization with respect to  $\psi = \sigma^{-1}\delta\sigma \in \mathfrak{se}(3)$ . For this, we compute the derivative of  $I(s)$  with respect to  $\Xi$  according to

$$\delta I = \left\langle \frac{\delta I(\Xi, \eta)}{\delta\Xi}, \Xi_1 \right\rangle = \left\langle \Xi^{-1} \frac{\delta I(\Xi, \eta)}{\delta\Xi}, \Xi^{-1}\Xi_1 \right\rangle, \quad (4.46)$$

where  $\psi_1 = \Xi^{-1}\Xi_1 \in \mathfrak{se}(3)$  is the linearization with respect to  $\Xi$ . To complete this calculation, we need to express  $\Xi^{-1}\Xi_1$  in terms of  $\psi_1$ . This step proceeds as follows.

The linearization of  $\Xi(s, s')$  in (4.24) gives

$$\Xi(s, s') = a^{s'-s} + \epsilon\Xi_1(s, s') + O(\epsilon^2), \quad (4.47)$$

where

$$\begin{aligned}
\Xi_1(s, s') &= -a^{-s}\sigma_1(s)a^{s'-s} + a^{-s}\sigma_1(s') \\
&= -\psi_1(s)a^{s'-s} + a^{s'-s}\psi_1(s') \\
&= a^{s'-s}(\psi_1(s') - \text{Ad}_{a^{s-s'}}\psi_1(s)).
\end{aligned} \tag{4.48}$$

Consequently, the quantity  $\Xi^{-1}\Xi_1$  is given by

$$\Xi^{-1}\Xi_1 = -\text{Ad}_{a^{s-s'}}\psi_1(s) + \psi_1(s'), \tag{4.49}$$

and we have

$$\begin{aligned}
\delta I &= \left\langle -\text{Ad}_{a^{s-s'}}^* \left( \Xi^{-1}(s, s') \frac{\delta I(\Xi(s, s'), \eta)}{\delta \Xi} \right) \right. \\
&\quad \left. + \Xi(s', s) \frac{\delta I(\Xi(s', s), \eta)}{\delta \Xi}, \psi_1 \right\rangle.
\end{aligned} \tag{4.50}$$

Finally, since  $I(s)$  in (4.45) is a linear function of an arbitrary  $\eta$ , re-arranging expression (4.50) into a scalar product of an  $\mathfrak{se}(3)^*$ -valued function with  $\eta$  will give the desired linearization operator  $\mathbb{L}(\Xi(s, s'))\psi_1(s)$ , from

$$\delta I =: \langle \mathbb{L}(\Xi(s, s'))\psi_1(s), \eta \rangle. \tag{4.51}$$

The equations simplify further upon noticing that for a stationary helical solution,  $\sigma = \sigma_0 a^s$  where  $a \in SE(3)$  is a given element, so the expression  $\lambda_0 = \sigma_0^{-1}(s)\sigma(s+1) = a$  is independent of  $s$ . Then, the linearization of equation (4.22) in the discrete case is

$$\begin{aligned}
&-\frac{\partial^2}{\partial t^2} I\psi_1 - \text{Ad}_{a^{-1}}^* \left( K_1(s) - \text{ad}_{\psi_1}^*(s)K_0 \right)(s) + K_1(s-1) \\
&= \sum_{s', m, k} \mathbb{L}(\Xi(s, s'))\psi_1(s).
\end{aligned} \tag{4.52}$$

It is natural to posit the following ansatz:

$$K_1(s) = a^{-s} \left[ J(\psi_1(s+1) - \psi_1(s)) \right] a^s := \text{Ad}_{a^s}^* \left( J(\psi_1(s+1) - \psi_1(s)) \right), \tag{4.53}$$

where  $\psi_1(s) \in \mathfrak{se}(3)$  and  $J : \mathfrak{se}(3) \rightarrow \mathfrak{se}(3)^*$  is a linear operator having the physical meaning of the rigidity matrix. Notice that the linearized system of coordinates is

written at the point  $s$ , but it encounters the value of the stress at the point  $s - 1$ . In order to connect this stress with the coordinate system at the point  $s$ , we will need to transform the coordinates to  $s - 1$ , by shifting one step forward on the helix. We thus need to compute  $\text{Ad}_{a^{-1}}^*$  of the term evaluated at  $s - 1$ , *i.e.*

$$K_1(s - 1) = \text{Ad}_{a^{-1}}^* \left[ J(\psi_1(s) - \psi_1(s - 1)) \right].$$

Then, the linearization of the discrete case gives

$$\begin{aligned} -\frac{\partial^2}{\partial t^2} I\psi_1 - \text{Ad}_{a^{-1}}^* \left[ J(\psi_1(s + 1) - 2\psi_1(s) + \psi_1(s - 1)) \right] \\ + \text{ad}_{\psi_1(s)}^* K_0 = \sum_{s', m, k} \mathbb{L}(\Xi(s, s')) \psi_1(s). \end{aligned} \quad (4.54)$$

In the continuous case, the corresponding linearization of equation (4.23) gives

$$-\frac{\partial^2}{\partial t^2} I\psi_1 + \left( -\frac{\partial}{\partial s} + \text{ad}_\Gamma^* \right) J\psi_1' + \text{ad}_{\psi_1}^* \Gamma = \sum_{m, k} \int \mathbb{L}(\Xi(s, s')) \psi_1(s) ds'. \quad (4.55)$$

Here, again  $\psi = \lambda_0^{-1}(s)\lambda_1(s) \in \mathfrak{se}(3)$ .

Further simplification can be obtained for the nonlocal term for the stationary helical state  $\sigma(s) = \sigma_0 a^s$ . The invariant variable  $\Xi = \sigma^{-1}(s)\sigma(s') = a^{s-s'}$  depends only on the difference between  $s$  and  $s'$ . Thus, all of the derivatives of the potential energy with respect to  $\Xi$  when evaluated at the helical configuration depend only on the difference between  $s$  and  $s'$ . In other words, we have

$$\begin{aligned} \Xi_0^{-1} \frac{\delta U}{\delta \Xi_0} (s, s') = D_1(s - s') \in \mathfrak{se}(3)^*, \\ \Xi_0^{-1} \frac{\delta}{\delta \Xi_0} \left( \Xi_0^{-1} \frac{\delta^2 U}{\delta \Xi_0} (s, s') \right) = D_2(s - s'), \end{aligned} \quad (4.56)$$

with  $D_2\alpha \in \mathfrak{se}(3)^*$  for any  $\alpha \in \mathfrak{se}(3)$ , so  $D_2 : \mathfrak{se}(3) \rightarrow \mathfrak{se}(3)^*$ .

Since all the functions on the right-hand side depend only on the difference  $s - s'$ , the integrals or sums become convolution integrals. Fourier transforming then allows the exact dispersion relation to be obtained, as follows. Let us consider

$$\psi_1(s, t) = S e^{-i\omega t + iks}, \quad S \in \mathfrak{se}(3). \quad (4.57)$$

Here  $s$  is an integer and  $k$  is the dimensionless wave number, measured in the units of  $2\pi/l_0$ , where  $l_0$  is the distance between the elements of the helical chain. Consequently, assuming  $S$  is real, the linearized equation (4.54) gives the following dispersion relation:

$$\omega^2 IS - 4\left(\sin^2 \frac{k}{2}\right) \text{Ad}_{a^{-1}}^* \left( JS - \text{ad}_S^* K_0 \right) = \sum_{s', m, k} \mathbb{L}(s') S. \quad (4.58)$$

Note that in the absence of non-local interactions, the basic helix must be unstressed,  $K_0 = 0$ , so  $\omega^2 = \lambda$  are given by the generalized eigenvalues of the problem

$$4 \sin^2 \frac{k}{2} \text{Ad}_{a^{-1}}^* \left( JS \right) = I \lambda S. \quad (4.59)$$

From physical principles, we require all the generalized eigenvalues of the matrices  $J$  and  $I$  to satisfy  $\lambda = \omega^2 > 0$ , so that all purely elastic helices in stationary conformations are neutrally stable. The spatially discrete dispersion relation (4.58) converges to the dispersion relation for the continuum case in the limit  $k \rightarrow 0$ ,  $a \rightarrow \text{Id}_{SE(3)}$ , which is

$$k^2 \text{Ad}_{a^{-1}}^* \left( JS \right) = I \lambda S. \quad (4.60)$$

Again, the right-hand side of (4.58) is a function of  $s' - s$  only, while the left-hand side is a constant. Upon summation over  $s'$ , the dependence on  $s$  disappears and the dispersion relation is obtained by setting  $s = 0$  on the right-hand side:

$$\omega^2 IS - \left(\sin^2 \frac{k}{2}\right) \text{Ad}_{a^{-1}}^* \left( JS - \text{ad}_S^* K_0 \right) = \sum_{s', m, k} \mathbb{L}(s') S. \quad (4.61)$$

The right-hand side is a linear operator acting on  $S$ . Instability corresponds to generalized eigenvalues  $\omega$  of equation (4.61) having a positive imaginary part. As it turns out, all eigenvalues  $\lambda = \omega^2$  are real, so it is enough to identify the case  $\lambda < 0$  as instability. However, the consideration of discrete rods puts an interesting spin on this problem that we will consider below.

## 4.7 Computation of potential energy

Equation (4.61) provides the stability analysis for an arbitrary interaction potential  $U(d)$ . However, for particular applications it is important to explicitly compute the linearization operators in (4.61). Again, geometric methods will be advantageous. Therefore, this section computes the linearization of the nonlocal terms for the dispersion relation. We believe it is advantageous to show this computation in some detail, as it is not trivial.

We shall perform the computation only for the discrete case. The continuous case is derived similarly with the change of sums with respect to  $s$  and  $s'$  into integrals where necessary. One has to be careful here, as we need to take derivatives of quantities that take values in  $T_e SE(3)$  and  $T_e SE(3)^*$ . The most straightforward way, least likely to lead to a mistake, is to define a corresponding scalar functional by bringing these quantities to the Lie algebra and then pairing them with the corresponding *fixed* element from the dual. The derivatives will then be given by whatever term is paired the chosen fixed element. This is akin to the weak computations of functional derivatives, only performed with geometric quantities.

First, notice that

$$\frac{\delta U}{\delta \Xi}(s, s') \Xi^{-1}(s, s') = \text{Ad}_{\Xi^{-1}(s, s')}^* \left( \Xi^{-1}(s, s') \frac{\delta U}{\delta \Xi}(s, s') \right), \quad (4.62)$$

and

$$\Xi(s, s') \frac{\delta U}{\delta \Xi}(s', s) = \left( \Xi^{-1}(s, s') \frac{\delta U}{\delta \Xi}(s, s') \right) \Big|_{s \leftrightarrow s'}. \quad (4.63)$$

Thus, we start the computation of the linearization operator  $D_2$  for the nonlocal term by linearizing the expression  $\Xi^{-1} \frac{\delta U}{\delta \Xi} \in \mathfrak{se}(3)^*$ . Let us consider  $\Xi = (\xi, \kappa)$  with  $\Xi^{-1} = (\xi^{-1}, -\xi^{-1}\kappa)$ , an arbitrary element  $(\phi, \Psi) \in \mathfrak{se}(3)$  and a scalar functional

$$I_1 = \left\langle \Xi^{-1} \frac{\delta U(d_{km})}{\delta \Xi}, (\mu, \alpha) \right\rangle. \quad (4.64)$$

The linearization operator  $D_2$  is therefore defined as

$$\left\langle D_2(\boldsymbol{\phi}, \boldsymbol{\Psi}), (\boldsymbol{\mu}, \boldsymbol{\alpha}) \right\rangle := \left\langle \Xi^{-1} \frac{\delta I_1(\boldsymbol{\mu}, \boldsymbol{\alpha})}{\delta \Xi}, (\boldsymbol{\phi}, \boldsymbol{\Psi}) \right\rangle. \quad (4.65)$$

Here, we introduced a natural pairing between two elements  $(a, \mathbf{b}) \in T_e SE(3)^*$  and  $(\alpha, \boldsymbol{\beta}) \in T_e SE(3)$ :

$$\langle (a, \mathbf{b}), (\alpha, \boldsymbol{\beta}) \rangle = \frac{1}{2} \text{tr}(a^T \alpha) + \mathbf{b} \cdot \boldsymbol{\beta}. \quad (4.66)$$

Given

$$d_{km}(\Xi(s, s')) = d_{km}(\xi, \boldsymbol{\kappa}) = |\boldsymbol{\kappa} + \boldsymbol{\eta}_k(s) - \xi(s, s') \boldsymbol{\eta}_m(s')|,$$

we have

$$\begin{aligned} I_1 &:= \left\langle \Xi^{-1} \frac{\delta U}{\delta \Xi}, (\boldsymbol{\mu}, \boldsymbol{\alpha}) \right\rangle \\ &= \frac{U'(d_{km})}{d_{km}} \left[ \text{tr} \left( -(\xi^{-1} \mathbf{d}_{km} \otimes \boldsymbol{\eta}_m)^T \hat{\boldsymbol{\mu}} \right) + (\xi^{-1} \mathbf{d}_{km}) \cdot \boldsymbol{\alpha} \right] \\ &= \frac{U'(d_{km})}{d_{km}} \left[ -(\xi^{-1} \mathbf{d}_{km} \times \boldsymbol{\eta}_m)^T \cdot \boldsymbol{\mu} + (\xi^{-1} \mathbf{d}_{km}) \cdot \boldsymbol{\alpha} \right] \\ &:= Q(d_{km}) I_2, \end{aligned} \quad (4.67)$$

since  $(\hat{\boldsymbol{\mu}})_{ij} = \epsilon_{ijk} \mu_k$  by the definition of the hat map. Here, we have defined

$$\begin{aligned} Q(d_{km}) &:= \frac{U'(d_{km})}{d_{km}}, \\ I_2(\Xi, \boldsymbol{\mu}, \boldsymbol{\alpha}) &:= -(\xi^{-1} \mathbf{d}_{km} \times \boldsymbol{\eta}_m)^T \cdot \boldsymbol{\mu} + (\xi^{-1} \mathbf{d}_{km}) \cdot \boldsymbol{\alpha}. \end{aligned} \quad (4.68)$$

In order to compute the linearization  $D_2$ , we proceed as follows. For  $(\boldsymbol{\phi}, \boldsymbol{\Psi}) \in \mathfrak{se}(3)$ , calculate

$$\begin{aligned} \left\langle \Xi^{-1} \frac{\delta I_1}{\delta \Xi}, (\boldsymbol{\phi}, \boldsymbol{\Psi}) \right\rangle &= \frac{Q'(d_{km})}{d_{km}} I_2(\Xi, \boldsymbol{\mu}, \boldsymbol{\alpha}) I_2(\Xi, \boldsymbol{\phi}, \boldsymbol{\Psi}) \\ &\quad + Q(d_{km}) \left\langle \Xi^{-1} \frac{\delta I_2}{\delta \Xi}, (\boldsymbol{\phi}, \boldsymbol{\Psi}) \right\rangle. \end{aligned} \quad (4.69)$$

We still need to compute the variational derivative of  $I_2(\Xi, \boldsymbol{\mu}, \boldsymbol{\alpha})$ . The only part of  $I_2$  depending on  $\Xi = (\xi, \boldsymbol{\kappa})$  is the quantity

$$\xi^{-1} \mathbf{d}_{km} = \xi^{-1}(\boldsymbol{\kappa} + \boldsymbol{\eta}_k) - \boldsymbol{\eta}_m.$$

Then,

$$\begin{aligned}
& \left\langle \xi^{-1} \frac{\partial}{\partial \xi} \xi^{-1} (\boldsymbol{\kappa} + \boldsymbol{\eta}_k) \cdot \boldsymbol{\alpha}, \hat{\psi} \right\rangle \\
&= -\frac{1}{2} \text{tr} \left\langle \xi^{-1} \frac{\partial}{\partial \xi} (\boldsymbol{\kappa} + \boldsymbol{\eta}_k) \cdot \xi \boldsymbol{\alpha}, \hat{\psi} \right\rangle - \frac{1}{2} \text{tr} \left\langle \boldsymbol{\alpha} \otimes (\boldsymbol{\kappa} + \boldsymbol{\eta}_k), \hat{\psi} \right\rangle \\
&= \left( \boldsymbol{\alpha} \times (\boldsymbol{\kappa} + \boldsymbol{\eta}_k) \right) \cdot \boldsymbol{\Psi} = \left( (\boldsymbol{\kappa} + \boldsymbol{\eta}_k) \times \boldsymbol{\Psi} \right) \cdot \boldsymbol{\alpha}.
\end{aligned} \tag{4.70}$$

Similarly,

$$\left\langle \xi^{-1} \frac{\partial}{\partial \boldsymbol{\kappa}} \xi^{-1} (\boldsymbol{\kappa} + \boldsymbol{\eta}_k) \cdot \boldsymbol{\alpha}, \hat{\psi} \right\rangle = \left\langle \xi^{-1} \frac{\partial}{\partial \boldsymbol{\kappa}} (\boldsymbol{\kappa} + \boldsymbol{\eta}_k) \cdot \xi \boldsymbol{\alpha}, \hat{\psi} \right\rangle = \boldsymbol{\alpha} \cdot \boldsymbol{\Psi}. \tag{4.71}$$

The derivatives of  $\xi^{-1} (\boldsymbol{\kappa} + \boldsymbol{\eta}_k) \times \boldsymbol{\eta}_m$  are computed similarly using standard properties of vector cross products. For brevity, we shall not present these calculations here. The final answer for  $D_{2,\boldsymbol{\mu}}$  is given by collecting the terms proportional to  $\boldsymbol{\mu}$ , and coefficient of  $D_{2,\boldsymbol{\alpha}}$  is given by the terms proportional to  $\boldsymbol{\alpha}$ . The operator  $D_2$  is thus given by

$$\begin{aligned}
D_{2,\boldsymbol{\mu}}(\boldsymbol{\Psi}, \boldsymbol{\phi}) &= \frac{Q'(d_{km})}{d_{km}} I_2(\Xi, \boldsymbol{\phi}, \boldsymbol{\Psi}) (\boldsymbol{\eta}_m \times \xi^{-1} \mathbf{d}_{km}) \\
&\quad + Q(d_{km}) \boldsymbol{\eta}_m \times \left( -\xi^{-1} (\boldsymbol{\kappa} + \boldsymbol{\eta}_k) \times \boldsymbol{\phi} + \boldsymbol{\Psi} \right), \\
D_{2,\boldsymbol{\alpha}}(\boldsymbol{\Psi}, \boldsymbol{\phi}) &= \frac{Q'(d_{km})}{d_{km}} I_2(\Xi, \boldsymbol{\phi}, \boldsymbol{\Psi}) \xi^{-1} \mathbf{d}_{km} \\
&\quad + Q(d_{km}) \left( -\xi^{-1} (\boldsymbol{\kappa} + \boldsymbol{\eta}_k) \times \boldsymbol{\phi} + \boldsymbol{\Psi} \right).
\end{aligned} \tag{4.72}$$

From (4.72) one notices a very interesting relationship, namely,

$$D_{2,\boldsymbol{\mu}}(\boldsymbol{\Psi}, \boldsymbol{\phi}) = \boldsymbol{\eta}_m \times D_{2,\boldsymbol{\alpha}}(\boldsymbol{\Psi}, \boldsymbol{\phi}). \tag{4.73}$$

The linearization operator is computed from  $D_2$  as follows (using  $\Xi(s, s') = a^{s'-s}$  and  $\psi_1(s) = S e^{iks}$ ):

$$\begin{aligned}
\mathbb{L}(\Xi)(\boldsymbol{\phi}, \boldsymbol{\Psi}) &= -\text{Ad}_{\Xi^{-1}}^* \left( D_2((\boldsymbol{\phi}, \boldsymbol{\Psi}) - \text{ad}_{(\boldsymbol{\phi}, \boldsymbol{\Psi})}^* D_1(\Xi))(s, s') \right. \\
&\quad \left. + \left( D_2(\boldsymbol{\phi}, \boldsymbol{\Psi}) \right)(s', s) \right),
\end{aligned} \tag{4.74}$$

where

$$D_1(\Xi) = \Xi^{-1} \frac{\delta U}{\delta \Xi} = \frac{U'(d_{km})}{d_{km}} \left( -(\xi^{-1} \mathbf{d}_{km} \times \boldsymbol{\eta}_m)^T, (\xi^{-1} \mathbf{d}_{km}) \right). \tag{4.75}$$

It is also useful to outline the formula for the change of variables  $s \leftrightarrow s'$  that forms the last term of the linearization operator  $\mathbb{L}$ . Under this change, the operators  $\text{Ad}$  and  $\text{Ad}^*$  change their form, and it is essential to perform this transformation correctly. Since

$$(\phi, \Psi)(s, s') = -\text{Ad}_{\Xi^{-1}(s, s')} \psi_1(s) + \psi_1(s') = -\text{Ad}_{a^{s-s'}} e^{iks} S + e^{iks'} S,$$

an exchange of variables  $s \leftrightarrow s'$  gives

$$(\phi, \Psi)(s', s) = -\text{Ad}_{\Xi^{-1}(s', s)} e^{iks'} \psi_1(s') + \psi_1(s) = -\text{Ad}_{a^{s'-s}} e^{iks'} S + e^{iks} S.$$

Thus, the final expression for the linearization of the nonlocal term is

$$\begin{aligned} \mathbb{L}(s)\psi_1 = & -\text{Ad}_{a^{-s'}}^* \left[ D_2(a^{s'}) (-\text{Ad}_{a^{-s'}} S + e^{iks'} S) \right. \\ & \left. - \text{ad}_{(-\text{Ad}_{a^{-s'}} S + e^{iks'} S)}^* D_1(\Xi) \right] + D_2(a^{-s'}) (-e^{iks'} \text{Ad}_{a^{s'}} S + S). \end{aligned} \quad (4.76)$$

## 4.8 Numerical stability of a linear polymer

In order to apply the general method of geometric linear stability of helical polymers derived in the previous section and show how our theory applies to a real-world case, we will solve the problem of linear stability in an example of a naturally straight, untwisted polymer in its unstressed configuration. The reason we choose this polymer is the relative simplicity of the formulas, where all the  $\text{Ad}$  and  $\text{Ad}^*$  operators are identities. Also, this is exactly the PVDF polymer considered in Section 4.4, with the linear state being the most basic energy state of the molecule. It is thus interesting to determine the conditions for the linear state to become unstable, so other helical states computed in that section can be achieved. We shall note that the stability of the helical states computed in Section 4.4 can be considered analogously using the results of the previous section. Here, however, we shall avoid doing this as it will make the chapter unnecessarily complex, due to the large number of helical states we have

described. Thus, for the sake of simplicity, we shall only concentrate on the stability of a polymer that is perfectly straight in an unstressed configuration, as illustrated in Fig. 4.7. We also explain in this section the difference between linear stability of a continuous and discrete polymer, and explain why a short enough polymer may exhibit stability whereas a long polymer will be unstable.

We assume the 2-charge bouquet with a charge of  $\pm q$  on each end, resulting in a constant dipole moment perpendicular to the axis. The charges interact through a screened electrostatic interaction (4.25) and Lennard-Jones interactions (4.34). The charges are positioned away from the axis at the distance  $l_c = 1\text{\AA}$ , and the distance between the charges is  $l_0 = 1\text{\AA}$ . We take electrostatic charges to be  $0.17e$ , leading to the dipole moment of  $5.33 \times 10^{-30} C \cdot m \simeq 1.63D$  (Debye units), which is slightly smaller than a PVDF polymer having similar polarization structure. Note that this charge is smaller than the value  $q = 0.3e$  taken in the computation of the stationary states, since for  $q = 0.3$  the subcritical bifurcation occurs for the values of ionic strength of about  $I \sim 200\text{M/l}$  which is orders of magnitude larger than any values of  $I$  achievable experimentally. Thus, the linear polymer with charges  $q = \pm 0.3e$  at the ends of bouquets will be inherently unstable for all viable experimental conditions.

### 4.8.1 Setup of the problem

**Remark 4.8.1.** *It is well known that the stability of finite Kirchhoff rods strongly depends on the end conditions imposed on the edges of the rod [34], p.81. The issue of choosing the right boundary conditions is a delicate one and, as far as we know, not entirely understood even for the Kirchhoff rods. Since the focus of this article is the investigation of the effects of nonlocal terms, we shall assume that the boundary conditions at the edges of the rod are such that Fourier transform analysis can be applied.*

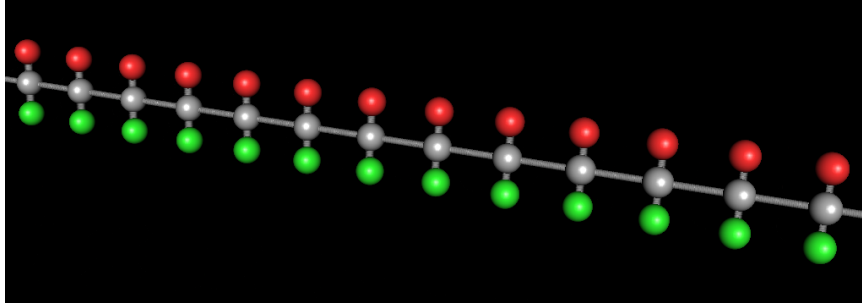


Figure 4.7: A particular example of charged rod with repeated configuration of two charges, plus (top) and minus (bottom) of  $q = 0.17e$  that interact through a screened electrostatic and Lennard-Jones potential.

For the purpose of this chapter we shall assume the simplest possible shape of the  $6 \times 6$  elastic tensor  $J$ : we take  $J$  to be diagonal, with the values of 3 first diagonals  $\mu = 3.025 \cdot 10^5 J/(rad^2)Mol = 5.022 \cdot 10^{-19} J/rad^2$  being the twist rigidity of a C-C bond, as outlined above, and the values of the last 3 diagonals (stretch rigidity along different directions) being  $\mu l^2$ . Such a choice of the elastic constants achieves  $J = Id_{6 \times 6}$  in the dimensionless units. All lengths are then expressed in units of  $l_0$ .

We take the inertia tensor to be

$$I_0 = \text{diag}(m_0 l_0^2, m_0 l_0^2, m_0 l_0^2, m_0, m_0, m_0),$$

where  $m_0$  is the mass of the charged atom at the end of the rigid bouquet. In reality,  $I$  will be a symmetric positive-definite tensor depending on the exact nature of the polymer selected. Selecting the time scale  $\tau = \sqrt{\mu/m_0}$  sets all the coefficients of the temporal and elastic terms exactly equal to unity. It is convenient to choose the unit of electrostatic charge as

$$e_* = \sqrt{4\pi\epsilon_0\mu l_0} \sim 1.514e.$$

The value  $e_*$  is chosen in such a way that two charges separated by  $l_0$  interact with potential  $\pm\mu$ . The dimensionless Lennard-Jones amplitude is  $\epsilon/\mu \sim 2.90 \times 10^{-4}$ .

Our theory is also applicable for more complex values of elasticity tensors. How-

ever, the more complex elastic properties of the rod may themselves lead to instabilities, as earlier works show [28,30]. Thus, we shall assume the simplest possible elastic tensor in order to concentrate on the appearance of instabilities due to the long-range interactions.

Limiting the considerations to unstressed linear polymers provides rather substantial simplifications in the expressions for the nonlocal terms. More precisely, the following simplifications hold:

$$\begin{aligned}
a &= \text{Parallel shift along the rod's axis by } l, \\
\text{Ad}_{a^s} &= \text{Identity in } \mathfrak{se}(3), \\
\text{Ad}_{a^s}^* &= \text{Identity in } \mathfrak{se}(3)^*, \\
K_0 &= 0 \quad (\text{no stress in the basic state}), \\
D_1 &= 0 \quad (\text{no twist in the basic state}).
\end{aligned} \tag{4.77}$$

Using this information, the dispersion relation  $\omega(k)$  can be now directly computed from (4.61). Unfortunately, even though the linearized operator  $\mathbb{L}$  is simplified considerably, very little further analytical progress can be made and one has to turn to numerical computations.

In order to compute the frequency  $\omega(k)$ , for a given  $k$ , we need to calculate the linearized operator  $\mathbb{L}$ . The computation proceeds as follows. First, we identify a basic vector  $S_i$  which is a unit vector in six-dimensional space, with 1 at  $i$ -th component and 0 otherwise. Then, we compute the matrix

$$M(k) = (\mathbf{q}_1, \dots, \mathbf{q}_6), \quad \mathbf{q}_i = \left(\sin^2 \frac{k}{2}\right) JS_i + \sum_{s', m, k} \mathbb{L}(s') S_i. \tag{4.78}$$

The frequencies  $\omega$  are then computed as generalized eigenvalues of

$$M(k)\mathbf{S} = \omega^2(k)I_0\mathbf{S}. \tag{4.79}$$

In Appendix D, we consider a simplified pedagogical case when the polymer is only allowed to twist, which leads to (almost) analytic expressions for the linear stability.

Unfortunately, in our case, the entries of 6x6 matrix  $M(k)$  for every wavenumber  $k$  have to be computed numerically as outlined above. It is not a difficult or numerically challenging computation though, and the computation of dispersion relation for several hundred values of  $k$  only takes a few seconds in *Matlab* on a standard desktop. The results of these computations are presented below.

### 4.8.2 Results of linear stability computations

For the rod we are considering here, in the absence of the nonlocal interactions the rod is neutrally stable, as the elastic tensor  $J$  is diagonal with positive entries. It is therefore interesting that nonlocal terms introduce instability, corresponding to  $\text{Im}(\omega(k)) > 0$ . Because  $\omega(k)$  only enters as  $\omega^2$  in (4.79), the instability occurs when  $\lambda = \omega^2(k)$  becomes negative. Physically, this instability is connected to the inclination of the rod to minimize its energy and properly align the dipole moments of each bouquet by twisting, as we have seen in the minimum energy calculation in Sec. 4.4. Mathematically, the instability corresponds to the eigenvalues of the linearization matrix  $M$  becoming negative for some  $k$ . However, one needs to keep in mind the discrete nature of our rods, making only certain values of  $k$  possible. Since we rescale the length by  $l_0$ , the distance between the centers of the bouquets, it is natural to take  $k \in [0, 2\pi]$ . In the continuum case, there is no restriction on the wavenumber, so the condition for the instability is simply

$$\text{Instability} = \min_{0 < k < 2\pi} \text{eigenvalues } (M) < 0.$$

On the other hand, for a discrete chain of length  $N$ ,  $k$  takes the values  $2\pi n/N$ , where  $0 < n < N$ . Thus, for a discrete chain

$$\text{Instability} = \min_{k=2\pi i/N} \text{eigenvalues } (M) < 0.$$

The difference between the discrete and continuous case is illustrated in Figure 4.8. The vertical axis shows the eigenvalue  $\lambda = \omega^2(k)$  with  $\lambda < 0$  corresponding to the

instability. Only the part  $0 < k < \pi$  has physical meaning, since dispersion curves are symmetric with respect to reflection about  $k = \pi$ . There is an instability region for small  $k < k_*$ . However, a polymer of length  $N = 9$  (circles) does not have any allowed wavenumbers in the unstable region, whereas a polymer of length  $N = 10$  (blue squares) has one wavenumber  $k = \pi/5$  in the unstable region. Thus, from a physical point of view, even for a formally unstable situation, a short enough chain will be stable. There is some indication that such behavior is indeed observed in VDF polymers [26].

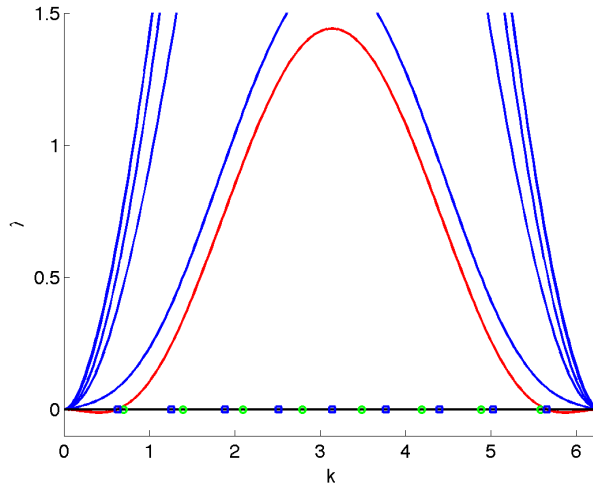


Figure 4.8: The eigenvalue  $\lambda(k) = \omega^2(k)$  of (4.79) is shown when the ionic strength of the solution  $I = 10^{-2}M/l$ . The lowest curve is the unstable dispersion curve. Circles correspond to a chain of length  $N = 9$ , squares are for  $N = 10$ .

When the ionic strength  $I$  is increased, the Debye screening length decreases according to (4.26), thereby decreasing the electrostatic interaction. It is thus natural to assume that the rod's instability decreases for large values of  $I$  until finally the stabilizing elastic forces overcome the nonlocal forces. This is the case here. On the left side of Figure 4.9, we show the maximum unstable wavenumber  $k_{max}$  as a function of the ionic strength  $I$ , and on the right side of this figure, we show the corresponding

maximum stable rod length. We see that stabilization happens at  $I \gtrsim 8.9\text{M/l}$ .

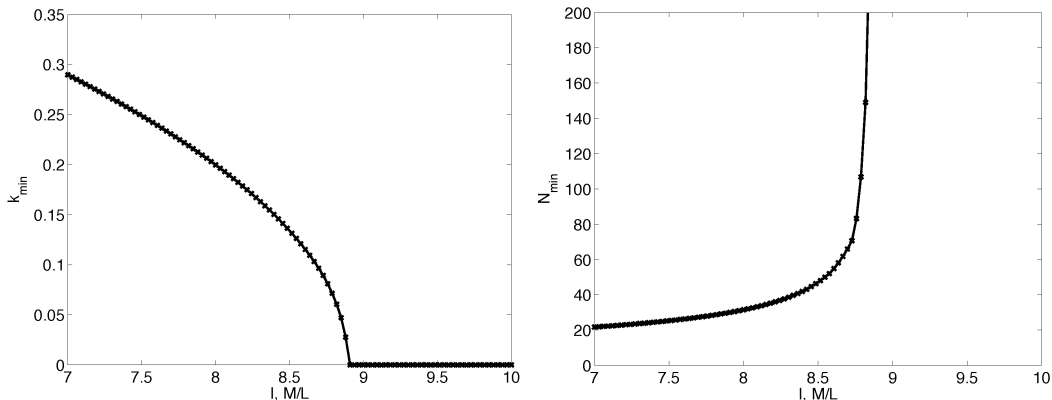


Figure 4.9: The minimum unstable wavenumber (left) and its inverse, the maximum unstable wavelength, (right) are shown as functions of ionic strength in M/l.

## 4.9 Conclusion

This chapter has investigated the particular example of a simple molecule whose helical configurations possess the complex and intriguing energy landscape shown in Fig. 4.3 and Fig. 4.4. Yellow dots in these figures correspond to energy minima and thus show stationary conformations. We have derived a general scheme for analyzing linear stability of these states, particularly to elucidate the effects of torque on the molecular rod generated by non-local interactions of off-axis charge conformations. The stability analysis was facilitated by the  $SE(3)$  symmetry of helical stationary configurations of the rod and it showed that non-local charge-interaction effects could induce instability of helical configurations due to the torques exerted on the rod by off-axis charges. This was illustrated by the instability of a linear polymer in its natural state. We have also shown how the increase of the ionic strength of the solution, in weakening the electrostatic interactions, leads to stabilization of the rod.

## REFERENCES

- [1] C. Branden and J. Tooze. *Introduction to Protein Structure, 2nd ed.* Garland Publishing, New York, NY, 1999.
- [2] P. Burkhard, J. Stetefeld, and S.V. Strelkov. Coiled coils: a highly versatile protein folding motif. *Trends in Cell Biology*, 11(2):82–88, 2001.
- [3] H. Li, D.J. DeRosier, W.V. Nicholson, E. Nogales, and K.H. Downing. Microtubule structure at 8 Å resolution. *Structure*, 10:1317–1328, 2002.
- [4] X. Yu, S.A. Jacobs, S.C. West, T. Ogawa, and E.H. Egelman. Domain structure and dynamics in the helical filaments formed by RecA and Rad51 on DNA. *Proc. Natl. Acad. Sci.*, 98(15):8419–8424, 2001.
- [5] J. J. L. M. Cornelissen, J. J. J. M. Donners, R. de Gelder, W. S. Graswinckel, G. A. Metselaar, A. E. Rowan, N. A. J. M. Sommerdijk, and R. J. M. Nolte.  $\beta$ -helical polymers from isocyanopeptides. *Science*, 293:676–680, 2001.
- [6] J. R. Matthews, F. Goldoni, A. P. H. J. Schenning, and E. W. Meijer. Non-ionic polythiophenes: a non-aggregating folded structure in water. *Chem. Comm*, pages 5503–5505, 2005.
- [7] N. Chouaieb, A. Goriely, and J. H. Maddocks. Helices. *Proc. Natl. Acad. Sci.*, 103:9398–9403, 2006.

- [8] J. R. Banavar, T. X. Hoang, J. H. Maddocks, A. Maritan, C. Poletto, A. Stasiak, and A. Trovato. Structural motifs of macromolecules. *Proc. Natl. Acad. Sci.*, 104:17283–17286, 2007.
- [9] E. H. Dill. Kirchhoff’s theory of rods. *Arch. Hist. Exact Sci.*, 44:1–23, 1992.
- [10] D. J. Dichmann, Y. Li, and J. H. Maddocks. *Hamiltonian Formulation and Symmetries in Rod Mechanics*, volume 82: Mathematical Approaches to Biomolecular Structure and Dynamics. Springer IMA, New York, 1992.
- [11] A. Goriely and M. Tabor. New amplitude equations for thin elastic rods. *Phys. Rev. Lett.*, 77:3537–3540, 1996.
- [12] R. Goldstein, T. R. Powers, and C. H. Wiggins. Viscous nonlinear dynamics of twist and writhe. *Phys. Rev. Lett.*, 80:5232–5235, 1998.
- [13] A. Balaeff, L. Mahadevan, and K. Schulten. Elastic rod model of a DNA loop in the lac operon. *Phys. Rev. Lett.*, 83:4900–4903, 1999.
- [14] R. Goldstein, A. Goriely, G. Huber, and C. Wolgemuth. Bistable helices. *Phys. Rev. Lett.*, 84:1631–1634, 2000.
- [15] A. Hausrath and A. Goriely. Repeat protein architectures predicted by a continuum representation of fold space. *Protein Science*, 15:1–8, 2006.
- [16] S. Neukirch, A. Goriely, and A. C. Hausrath. Chirality of coiled coils: Elasticity matters. *Phys. Rev. Lett.*, 100:038105, 2008.
- [17] N. Chouaieb and J. Maddocks. Kirchhoff’s problem of helical equilibria of uniform rods. *J. of Elasticity*, 77:221–247, 2004.

- [18] S. DeLillo, G. Lupo, and M. Sommacal. Helical configurations of elastic rods in the presence of a long-range interaction potential. *J. Phys. A: Math. Gen.*, 43:085214, 2010.
- [19] A. Maritan, C. Micheletti, A. Trovato, and J. R. Banavar. Optimal shapes of compact strings. *Nature*, 406:287–290, 2000.
- [20] D. D. Holm and V. Putkaradze. Nonlocal orientation-dependent dynamics of charged strands and ribbons. *C. R. Acad. Sci. Paris, Sér. I: Mathématique*, 347:1093–1098, 2009.
- [21] D. Ellis, D. D. Holm, F. Gay-Balmaz, V. Putkaradze, and T. Ratiu. Geometric mechanics of flexible strands of charged molecules. *Arch. Rat. Mech. Anal.*, To appear, 2009.
- [22] J. C. Simó, J. E. Marsden, and P. S. Krishnaprasad. The Hamiltonian structure of nonlinear elasticity: The material and convective representations of solids, rods, and plates. *Arch. Rat. Mech. Anal.*, 104:125–183, 1988.
- [23] D. D. Holm. *Geometric Mechanics II: Rotation, Translation and Rolling*. Imperial College Press, 2009.
- [24] J. Moser and A. P. Veselov. Discrete versions of some classical integrable systems and factorization of matrix polynomials. *Comm. Math. Phys.*, 139:217–243, 1991.
- [25] L. Pauling, R. B. Corey, and H. R. Branson. The structure of proteins: Two hydrogen-bonded helical configurations of the polypeptide chain. *Proc. Natl. Acad. Sci.*, 37:205–2011, 1951.
- [26] K. Noda, K. Ishida, A. Kubono, T. Horiuchi, and H. Yamada. Remanent polarization of evaporated films of vinylidene fluoride oligomers. *J. Appl. Phys.*, 93:2866–2870, 2003.

- [27] J. R. Quine. Helix parameters and protein structure using quaternions. *Journal of Molecular Structure (Theochem)*, 460:53–66, 1999.
- [28] A. Goriely and M. Tabor. Nonlinear dynamics of filaments. iii. instabilities of helical rods. *Proc. Roy. Soc. A*, 453:2583–2601, 1997.
- [29] A. Goriely and M. Tabor. The nonlinear dynamics of filaments. *Nonlinear Dynamics*, 21:101–133, 2000.
- [30] P. Shipman and A. Goriely. Dynamics of helical strips. *Physical Review E*, 61:4508–4517, 2000.
- [31] A. Goriely, M. Nizette, and M. Tabor. On the dynamics of elastic strips. *J. Nonlinear Science*, 11:3–45, 2001.
- [32] S. Lafortune, A. Goriely, and M. Tabor. The dynamics of stretchable rods in the inertial case. *Nonlinear Dynamics*, 43:173–195, 2005.
- [33] T. C. Bishop, R. Cortez, and O. O. Zhmudsky. Investigation of bend and shear waves in a geometrically exact elastic rod model. *J. Comp. Physics*, 193:642–665, 2004.
- [34] N. Chouaieb. *Kirchhoff's problem of helical solutions of uniform rods and their stability properties*. PhD thesis, EPFL, Sec. Math., 2003.

## APPENDIX A

### PROOF OF LEMMA 3.2.1

We begin with the divergence theorem,

$$\iint_{\Omega_{\mathcal{D}}} \mathbf{F}(\mathbf{p}) \cdot \hat{\mathbf{n}} \, dA = \iiint_{\mathcal{D}} \left( \frac{\partial \mathbf{F}}{\partial x} + \frac{\partial \mathbf{F}}{\partial y} + \frac{\partial \mathbf{F}}{\partial z} \right) dx \, dy \, dz .$$

If we choose  $\mathbf{F}(\mathbf{p}) = \mathbf{p}/3$ , then

$$\iint_{\Omega_{\mathcal{D}}} \frac{\mathbf{p}}{3} \cdot \hat{\mathbf{n}} \, dA = \iiint_{\mathcal{D}} dx \, dy \, dz = V .$$

Because the surface is made of the set  $\mathcal{F}$  of triangles  $f_i = (\mathbf{q}_{i_1}, \mathbf{q}_{i_2}, \mathbf{q}_{i_3})$ , with normal vectors  $\hat{\mathbf{n}}_i$ , which we can write explicitly as

$$\hat{\mathbf{n}}_i = \frac{(\mathbf{q}_{i_2} - \mathbf{q}_{i_1}) \times (\mathbf{q}_{i_3} - \mathbf{q}_{i_1})}{|(\mathbf{q}_{i_2} - \mathbf{q}_{i_1}) \times (\mathbf{q}_{i_3} - \mathbf{q}_{i_1})|} ,$$

we can replace the surface integral with a sum of integrals over each triangle,

$$V = \frac{1}{3} \sum_{f_i \in \mathcal{F}} \iint_{f_i} \mathbf{p} \cdot \hat{\mathbf{n}}_i \, dA .$$

We parametrize a point  $\mathbf{p}$  on triangle  $f_i$  using  $\alpha$  and  $\beta$  as

$$\mathbf{p} = \mathbf{q}_{i_1} + \alpha (\mathbf{q}_{i_3} - \mathbf{q}_{i_1}) + \beta (1 - \alpha) (\mathbf{q}_{i_2} - \mathbf{q}_{i_1}) ,$$

where the area element is

$$dA = |(\mathbf{q}_{i_2} - \mathbf{q}_{i_1}) \times (\mathbf{q}_{i_3} - \mathbf{q}_{i_1})| \, d\alpha \, d\beta ,$$

and integrate over  $\alpha \in (0, 1)$  and  $\beta \in (0, 1 - \alpha)$ ,

$$V = \frac{1}{3} \sum_{f_i \in \mathcal{F}} \int_0^1 \int_0^{1-\alpha} (\mathbf{q}_{i_1} \cdot \hat{\mathbf{n}}_i + \alpha (\mathbf{q}_{i_3} - \mathbf{q}_{i_1}) \cdot \hat{\mathbf{n}}_i + \beta (1 - \alpha) (\mathbf{q}_{i_2} - \mathbf{q}_{i_1}) \cdot \hat{\mathbf{n}}_i) dA.$$

Noticing that  $(\mathbf{q}_{i_2} - \mathbf{q}_{i_1}) \perp \hat{\mathbf{n}}_i$  and  $(\mathbf{q}_{i_3} - \mathbf{q}_{i_1}) \perp \hat{\mathbf{n}}_i$ , this simplifies to

$$V = \frac{1}{6} \sum_{f_i \in \mathcal{F}} |(\mathbf{q}_{i_2} - \mathbf{q}_{i_1}) \times (\mathbf{q}_{i_3} - \mathbf{q}_{i_1})| \mathbf{q}_{i_1} \cdot \hat{\mathbf{n}}_i.$$

## APPENDIX B

### ALGORITHM FOR MESH ADJUSTMENT

Given a fixed constant  $\varepsilon$ , a degeneracy threshold  $\mu \ll \varepsilon$ , and a maximal angle  $\phi_{max}$  with  $0 < \pi - \phi_{max} \ll \pi$ , we consider a triangulated mesh to be “valid” if the following conditions hold:

1. no edge has length exceeding  $\varepsilon$ ,
2. no face has a largest angle exceeding  $\phi_{max}$ , and
3. no edges have length smaller than  $\mu$ , unless removing that edge would violate condition (2)

After each step in the evolution of the mesh representation of a membrane, the mesh must be adjusted to correct any violations of the above conditions. We modify the procedure in [1] to accomplish this.

#### B.0.1 Edge length adjustment

The first step is to ensure that no edge in the mesh has length exceeding  $(\varepsilon - 2\mu)$ . To do this, we simply divide any edge with length exceeds  $(\varepsilon - 2\mu)$  at its midpoint with a new vertex point, and create a new edge from this new vertex to the opposite vertex of the two faces that share the edge being divided, as shown in Figure B.1. Since there

are finitely many such edges, and each requires at a finite number of subdivisions to drive edge lengths below  $\varepsilon$ , this process is guaranteed to terminate.

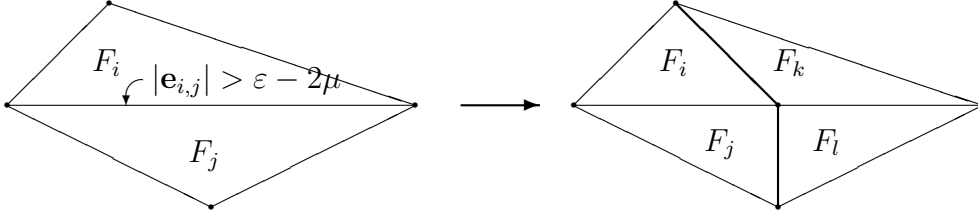


Figure B.1: Subdividing an edge for which  $|\mathbf{e}_{i,j}| > \varepsilon$ . The edge is divided into two edges, each half the original length. This operation adds one vertex, three edges, and two faces.

## B.0.2 Elimination of caps

Following [1], we define a *cap* as a face whose largest angle exceeds  $\theta_{max}$  but whose smallest edge length is larger than  $\mu$  (we deal with faces with edge lengths below  $\mu$  in a later step).  $\theta_{max}$  is related to  $\psi_{max}$  as follows. Given a triangle

For each cap face in the mesh, we define a plane perpendicular to the cap face and to the edge opposite the large angle, passing through the vertex where the large angle occurs, and slice the entire model with this plane. We refer the reader to [1] for details of the method to prevent such an operation from creating new cap faces. The results is the elimination of the cap face without the introduction of any new cap faces. As there are finitely many cap faces in the mesh, this process is guaranteed to terminate. Also, since this process only subdivides existing faces, it cannot introduce an edge that is longer than an existing edge, and so the resulting mesh will have no edge exceeding  $(\varepsilon - \mu)$  in length.

### B.0.3 Elimination of microfaces

We define a *microface* as a face with at least two edges of length smaller than  $\mu$ . We eliminate such faces, when doing so would not create a cap, by replacing the face by a vertex at its center, as shown in Figure B.2. Note that this operation can move a vertex by at most  $\varepsilon\sqrt{3}/3$ .

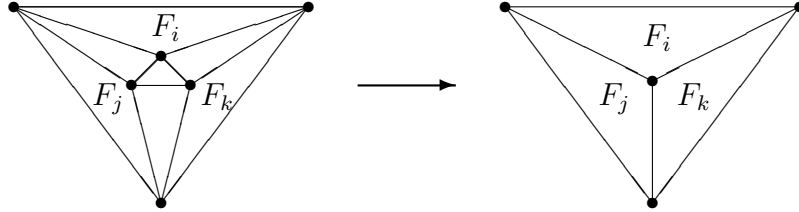


Figure B.2: Removing a microface by replacing it with a single vertex. This operation removes two vertices, six edges, and four faces.

### B.0.4 Elimination of needles

We next define a *needle* as a face with a single edge has length smaller than  $\mu$ . Needles are eliminated, when doing so would not create a cap, by replacing the small edge by a vertex at its midpoint, eliminating the small edge and the two triangles that share that edge, as shown in Figure B.3. This operation can move a vertex by, at most,  $\mu/2$ .

The removal of microfaces and needles can move each vertex, at most,  $\mu\sqrt{3}/3$ , and so the length of each edge cannot exceed  $\varepsilon$  after these operations, leaving the mesh in a valid state.

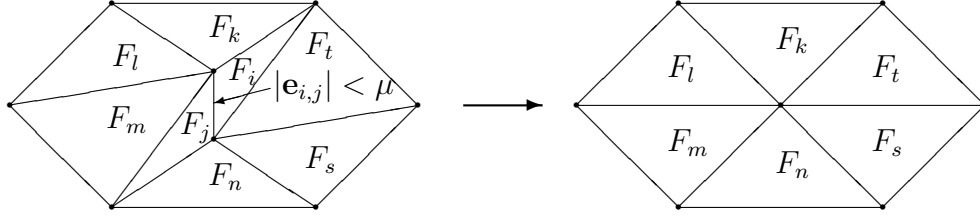


Figure B.3: Merging vertices to remove a needle. The short edge is replaced by a single vertex at its midpoint. This operation removes one vertex, three edges, and two faces.

### B.0.5 Maximal movement for subsequent modeling iteration

Having ensured that the mesh is valid, the maximum movement that a vertex can be allowed to undergo during the subsequent time step in the model evolution is given by half the length of the shortest edge or altitude associated with that vertex, where we compute the altitude  $d_i$  of a face relative to vertex  $\mathbf{p}_i$  from the face area  $A_i$  using the edge  $\mathbf{e}_{j,k}$  opposite the vertex in the face, by

$$d_i = \frac{2A_i}{|\mathbf{e}_{j,k}|}.$$

This constraint ensures that faces will not become degenerate during model evolution, and that the adjustment process described here will be able to restore the mesh to a valid state after the vertex positions are updated.

## APPENDIX C

### GEOMETRIC PROPERTIES OF $SE(3)$ GROUP

This Appendix describes the geometric structure of  $SE(3)$  group and defines the aspects of its adjoint and co-adjoint actions that are needed for the computations in the text. For more details and the theoretical framework, see [2].

Suppose  $G$  is a Lie group, and  $g$  and  $h$  are elements of  $G$ . Then, the AD operator – the conjugacy class of  $h$  – is defined as

$$\text{AD}_g h = ghg^{-1}, \quad (\text{C.1})$$

for all  $g \in G$ . Assume that  $h(t)$  changes smoothly with respect to a parameter  $t$  starting at the unit element of the group. Then,  $h(0) = e$  and  $h'(0) = \eta$  is the velocity at the initial point, taken to be unity. Note that  $\eta$  is an element of the tangent space at unity which is the Lie algebra of  $G$ . We denote this fact as  $T_e G \simeq \mathfrak{g}$ . In this notation, the Adjoint operation is defined as

$$\text{Ad}_g \eta = \left. \frac{d}{dt} gh(t)g^{-1} \right|_{t=0} = g\eta g^{-1}. \quad (\text{C.2})$$

Note that Ad takes an element in  $\eta \in \mathfrak{g}$  and produces another element in  $\mathfrak{g}$ . Now, suppose  $g(\epsilon)$  is also varying with respect to a parameter  $\epsilon$ , and again  $g(0) = e$ ,  $g'(0) = \xi \in \mathfrak{g}$ . In this notation, the *adjoint* operator ad is defined as

$$\text{ad}_\xi \eta = \left. \frac{d}{d\epsilon} \text{Ad}_g(\epsilon) \eta \right|_{\epsilon=0} = \xi \eta - \eta \xi =: [\xi, \eta], \quad (\text{C.3})$$

where  $[\cdot, \cdot]$  is the commutator in the Lie algebra  $\mathfrak{g}$ .

In order to derive equations, it is important to consider the co-adjoint operators  $\text{Ad}^*$  and  $\text{ad}^*$ . The operation  $\text{Ad}^* : G \times \mathfrak{g}^* \rightarrow \mathfrak{g}^*$ , is defined for  $g \in G$  and  $a \in \mathfrak{g}^*$  as

$$\langle \eta, \text{Ad}_g^* a \rangle = \langle \text{Ad}_g \eta, a \rangle \quad (\text{C.4})$$

for every  $\eta \in \mathfrak{g}$ , in terms of a suitable pairing  $\langle \cdot, \cdot \rangle : \mathfrak{g}^* \times \mathfrak{g} \rightarrow \mathbb{R}$ . Similarly, the operation  $\text{ad}^* : \mathfrak{g} \times \mathfrak{g}^* \rightarrow \mathfrak{g}^*$ , is defined for  $\eta, \xi \in \mathfrak{g}$  and  $a \in \mathfrak{g}^*$  as

$$\langle \eta, \text{ad}_\xi^* a \rangle = \langle \text{ad}_\xi \eta, a \rangle. \quad (\text{C.5})$$

Let us now see how these formulas are expressed for the  $SE(3)$  group. The Lie group multiplication of two elements  $(\Lambda_1, \mathbf{r}_1) \in SE(3)$  and  $(\Lambda_2, \mathbf{r}_2) \in SE(3)$ , where  $\Lambda_1, \Lambda_2 \in SO(3)$  and  $\mathbf{r}_1, \mathbf{r}_2 \in \mathbb{R}^3$ , is defined as follows:

$$(\Lambda_1, \mathbf{r}_1) \cdot (\Lambda_2, \mathbf{r}_2) = (\Lambda_1 \Lambda_2, \Lambda_1 \mathbf{r}_2 + \mathbf{r}_1) \quad (\text{C.6})$$

with the meaning of subsequent application of rotation and shift. The inverse element is then

$$(\Lambda, \mathbf{r})^{-1} = (\Lambda^{-1}, -\Lambda^{-1} \mathbf{r}). \quad (\text{C.7})$$

The tangent space  $T_{(\Lambda_0, \mathbf{r}_0)} SE(3)$  at a point  $(\Lambda_0, \mathbf{r}_0)$  is defined as the space of derivatives of curves  $(\Lambda(t), \mathbf{r}(t))$  at  $t = 0$  given that  $\Lambda(0) = \Lambda_0$ ,  $\mathbf{r}(0) = \mathbf{r}_0$ . In order to obtain the element of the tangent space at the identity – that is, the Lie algebra  $T_e SE(3) \simeq \mathfrak{se}(3)$  – we compute the derivative at  $\Lambda_0 = \text{Id}_{3 \times 3}$  (a  $3 \times 3$  unity matrix),  $\mathbf{r}_0 = \mathbf{0}$ . Hence, an element of this Lie algebra can be written as

$$\eta = (\hat{\omega}, \mathbf{v}) = (\boldsymbol{\omega}, \mathbf{v}) \in \mathfrak{se}(3),$$

where  $\hat{\omega}$  denotes a skew-symmetric  $3 \times 3$  matrix and  $\mathbf{v}$  is a vector in three dimensions. Here, we may use the so-called “hat map” correspondence between the skew-symmetric matrices and vectors to define a vector  $\boldsymbol{\omega} \in \mathbb{R}^3$  as  $\hat{\omega}_{ij} = -\epsilon_{ijk} \omega_k$ , such that

$\hat{\boldsymbol{\omega}} \mathbf{r} = \boldsymbol{\omega} \times \mathbf{r}$  for all  $\mathbf{r}$ . Thus,  $\mathfrak{se}(3)$  is a six-dimensional vector space, with the first three components having the physical meaning of the angular velocity, and the last three components being the linear velocity.

Using this preliminary information, we are ready to define the adjoint actions. After some relatively straightforward computations, we have:

$$\text{Ad}_{(\Lambda, \mathbf{r})}(\tilde{\Lambda}, \tilde{\mathbf{r}}) = (\Lambda \tilde{\Lambda} \Lambda^{-1}, -\Lambda \tilde{\Lambda} \Lambda^{-1} \mathbf{r} + \Lambda \tilde{\mathbf{r}} + \mathbf{r}). \quad (\text{C.8})$$

Then if  $(\hat{\boldsymbol{\omega}}, \mathbf{v}) = \frac{d}{dt}(\tilde{\Lambda}(t), \tilde{\mathbf{r}}(t))|_{t=0}$ ,

$$\text{Ad}_{(\Lambda, \mathbf{r})}(\hat{\boldsymbol{\omega}}, \mathbf{v}) = (\Lambda \hat{\boldsymbol{\omega}} \Lambda^{-1}, -\Lambda \hat{\boldsymbol{\omega}} \Lambda^{-1} \mathbf{r} + \Lambda \mathbf{v}), \quad (\text{C.9})$$

and using  $\hat{\boldsymbol{\omega}} \Lambda^{-1} \mathbf{r} = \boldsymbol{\omega} \times \Lambda^{-1} \mathbf{r} = \Lambda^{-1}(\Lambda \boldsymbol{\omega} \times \mathbf{r})$ ,

$$\text{Ad}_{(\Lambda, \mathbf{r})}(\hat{\boldsymbol{\omega}}, \mathbf{v}) = (\Lambda \hat{\boldsymbol{\omega}} \Lambda^{-1}, -\Lambda \boldsymbol{\omega} \times \mathbf{r} + \Lambda \mathbf{v}). \quad (\text{C.10})$$

To express this in vector form, we note that for arbitrary  $\mathbf{u}$ ,  $\Lambda \hat{\boldsymbol{\omega}} \Lambda^{-1} \mathbf{u} = \Lambda(\boldsymbol{\omega} \times \Lambda^{-1} \mathbf{u}) = \Lambda \boldsymbol{\omega} \times \mathbf{u} = (\Lambda \boldsymbol{\omega}) \hat{\mathbf{u}}$ , one has

$$\text{Ad}_{(\Lambda, \mathbf{r})}(\boldsymbol{\omega}, \mathbf{v}) = (\Lambda \boldsymbol{\omega}, -\Lambda \boldsymbol{\omega} \times \mathbf{r} + \Lambda \mathbf{v}). \quad (\text{C.11})$$

Letting  $(\hat{\boldsymbol{\omega}}_1, \boldsymbol{\alpha}_1) = \frac{d}{d\epsilon}(\Lambda(\epsilon), \mathbf{r}(\epsilon))|_{\epsilon=0}$ , one finds

$$\text{ad}_{(\hat{\boldsymbol{\omega}}_1, \boldsymbol{\alpha}_1)}(\hat{\boldsymbol{\omega}}_2, \boldsymbol{\alpha}_2) = (\hat{\boldsymbol{\omega}}_1 \hat{\boldsymbol{\omega}}_2 - \hat{\boldsymbol{\omega}}_2 \hat{\boldsymbol{\omega}}_1, -\hat{\boldsymbol{\omega}}_2 \boldsymbol{\alpha}_1 + \hat{\boldsymbol{\omega}}_1 \boldsymbol{\alpha}_2), \quad (\text{C.12})$$

then because  $[\hat{\boldsymbol{\omega}}_1, \hat{\boldsymbol{\omega}}_2] \mathbf{u} = (\boldsymbol{\omega}_1 \times \boldsymbol{\omega}_2) \times \mathbf{u}$  for all  $\mathbf{u}$ , we can express this in vector form as

$$\text{ad}_{(\boldsymbol{\omega}_1, \boldsymbol{\alpha}_1)}(\boldsymbol{\omega}_2, \boldsymbol{\alpha}_2) = (\boldsymbol{\omega}_1 \times \boldsymbol{\omega}_2, \boldsymbol{\omega}_1 \times \boldsymbol{\alpha}_2 - \boldsymbol{\omega}_2 \times \boldsymbol{\alpha}_1). \quad (\text{C.13})$$

The physically relevant pairing between two elements  $(\boldsymbol{\omega}, \boldsymbol{\alpha}) \in \mathfrak{se}(3)$  and  $(\mathbf{u}, \mathbf{a}) \in \mathfrak{se}(3)^*$  is given by

$$\langle (\boldsymbol{\omega}, \boldsymbol{\alpha}), (\mathbf{u}, \mathbf{a}) \rangle = \boldsymbol{\omega} \cdot \mathbf{u} + \boldsymbol{\alpha} \cdot \mathbf{a}. \quad (\text{C.14})$$

With this choice of pairing, we may also write  $\mathfrak{se}(3)$  as a pair of two 3D vectors. In that notation, the co-Adjoint operator is

$$\text{Ad}_{(\Lambda, \mathbf{r})}^*(\mathbf{u}, \mathbf{a}) = (\Lambda \mathbf{u} + \mathbf{r} \times \Lambda \mathbf{a}, \Lambda \mathbf{a}), \quad (\text{C.15})$$

and the co-adjoint action is given by

$$\text{ad}_{(\boldsymbol{\omega}, \boldsymbol{\alpha})}^*(\mathbf{u}, \mathbf{a}) = (\mathbf{u} \times \boldsymbol{\omega} - \boldsymbol{\alpha} \times \mathbf{a}, -\boldsymbol{\omega} \times \mathbf{a}). \quad (\text{C.16})$$

## APPENDIX D

### TWIST DYNAMICS OF A STRAIGHT POLYMER

In this section, we consider the linear polymer drawn in Fig. 4.7 with the restriction that the charge bouquets can only twist about the axis, and only in the plane perpendicular to the axis. The rod itself is assumed to be completely rigid. This problem – in a slightly different configuration – was considered in [3] as a model of DNA dynamics. For convenience, we take the mass of the charges to be  $m_0/2$  so the moment of inertia has the value  $m_0 l_0^2$  (no factor of 2), to coincide with the formulas derived in Sec. 4.8. We show two ways to analyze the linear stability of this problem.

#### Standard solution

The configuration space for this problem is described by the angles of rotation  $\phi_i$ . The coordinate for the positive and negative charges are given by

$$\mathbf{r}_{k,\pm} = (kl, \pm l_0 \cos \phi_k, \pm l_0 \sin \phi_k).$$

The state  $\phi_i = 0$  for all  $i$  is an equilibrium state of the system. In order to linearize around that state, we proceed as follows.

The distance between a charge at  $m$ -th unit and a charge at  $n$ -th unit depends on whether the charges are at the same or opposite sides of the chain. For the same side we get

$$\begin{aligned} d_{mn}^+ &= \sqrt{l_0^2 (m-n)^2 + l^2 (\cos \phi_m - \cos \phi_n)^2 + l^2 (\sin \phi_m - \sin \phi_n)^2} \\ &\simeq \sqrt{l_0^2 (m-n)^2 + l^2 \frac{1}{4} (\phi_m^2 - \phi_n^2)^2 + l^2 (\phi_m - \phi_n)^2 + O(\phi^4)}. \end{aligned}$$

For charges on the opposite sides of the chain,

$$\begin{aligned} d_{mn}^- &= \sqrt{l_0^2 (m-n)^2 + l^2 (\cos \phi_m + \cos \phi_n)^2 + l^2 (\sin \phi_m + \sin \phi_n)^2} \\ &\simeq \sqrt{l_0^2 (m-n)^2 + l^2 \left(2 - \frac{1}{2}\phi_n^2 - \frac{1}{2}\phi_m^2\right)^2 + l^2 (\phi_m + \phi_n)^2 + O(\phi^4)}. \end{aligned}$$

The electrostatic energy is positive for the charges on the same side, and negative for the charges on the opposite side, whereas Lennard-Jones energy only depends on the distance between the charges. Thus, the total potential energy  $\mathbb{P}$  is given by the sum

$$\mathbb{P} = -\frac{1}{2} \sum_m J \phi_m^2 + \frac{1}{2} \sum_{m,n,\pm} U(d_{mn}^\pm) + U(d_{mn}^-). \quad (\text{D.1})$$

The linearized equation of state is given by

$$I \frac{d^2 \phi_m}{dt^2} = -\frac{\partial \mathbb{P}}{\partial \phi_m}, \quad (\text{D.2})$$

where  $I = m_0 l_0^2$  is the moment of inertia,  $m_0$  being the mass of the charged particle. We choose the length to be measured in terms of  $l$ , and wavenumber  $0 < k < 2\pi$  will be dimensionless. Assuming  $\phi_m = e^{ikm - i\omega t} S$ , after some fairly simple algebra we obtain the following dispersion relation:

$$I\omega^2(k) = J \sin^2 \frac{kl_0}{2} - \sum_{m=-\infty, m \neq 0}^{\infty} \left[ \frac{U'(|m|)}{|m|} + \frac{U'(\sqrt{m^2+4})}{\sqrt{m^2+4}} \right] (1 - e^{ikm}).$$

On summing up terms with opposite signs of  $m$ , one finds the real expression

$$I\omega^2(k) = J \sin^2 \frac{kl_0}{2} - \sum_{m=1}^{\infty} \left[ \frac{U'(|m|)}{|m|} + \frac{U'(\sqrt{m^2+4})}{\sqrt{m^2+4}} \right] 4 \sin^2 \frac{mk}{2}. \quad (\text{D.3})$$

For the chosen values of physical parameters,  $\omega^2 > 0$  and the twist dynamics is stable.

### Geometric method

Assume that the axis of the rod is along  $x$ -axis, and all the charges in the undisturbed configuration are aligned along the  $z$ -axis. The deformations are rotations about the  $x$ -axis, which are given by the first coordinate in  $\mathfrak{se}(3)$  representation. The resulting

rotation is also about the  $x$ -axis, so we need to look at the first row of the matrix  $M$  in (4.78). Thus, the stability of the problem of the twist about the axis is considered as simply the  $(1, 1)$  component of (4.79):

$$I_{11}\omega^2 = (MS_1)_1, \tag{D.4}$$

where we take  $S_1 = (1, 0, 0, 0, 0, 0)^T$  to be the vector of infinitesimal rotations about the  $x$ -axis. Again, after some rather straightforward algebra (not presented here) we see that the right-hand side of (D.4) gives exactly (D.3). As verification of our code, we also compared the numerical results given by these two methods; they were identical within numerical accuracy of the computations.

We note that (D.3) *does not* correspond to any eigenvalues, since the vector  $MS_1$  is full, *i.e.* it has non-trivial components at other entries besides the first. These components arise because a realistic twist deformation about the  $x$ -axis induces twists and stretches in other directions. Nevertheless, we feel that such a simplified physical example still provides a useful verification procedure for the full stability calculation.

## REFERENCES

- [1] M. Botsch and L. P. Kobbelt. A robust procedure to eliminate degenerate faces from triangle meshes. *Proceedings of the Sixth International Fall Workshop Vision, Modeling, and Visualization*, pages 402–410, 2001.
- [2] D. D. Holm. *Geometric Mechanics II: Rotation, Translation and Rolling*. Imperial College Press, 2009.
- [3] I. Mezić. On the dynamics of molecular conformation. *Proc. Natl. Acad. Sci.*, 103:7542–7547, 2006.